Spin State Tailoring of Quantum Dot Spins for Quantum Information Processing

Kristopher Barr
Experimental Quantum Nanoscience Laboratory
Department of Physics
University of Strathclyde
Glasgow, Scotland

August 31, 2024

Thesis Abstract

Individual quantum dots can be efficiently harnessed as matter-based spin-qubits resulting in applications across the field of quantum information processing. In this work, single-qubit operations of quantum dot spin states are shown through a range of coherent control experiments demonstrating that these systems have great potential. The system structure of the quantum dot can be varied through application of a range of electric and magnetic fields. This work extended the existing body of knowledge through characterization of the system properties and further by experimental demonstrations under non-standard magnetic field configurations.

The initial objective required developing a state-of-the-art experiment with capabilities to manipulate and control individual quantum dot spin-qubits. This involved building and optimizing a cryo-magnetic environment alongside a complex optical excitation system using pulsed and continuous wave lasers. Upon completion, the remainder of this work demonstrated coherent control between the ground-state spins confined to a quantum dot under both standard and non-standard magnetic fields. The system was characterized under oblique magnetic field configurations which mix the properties common to the Voigt and Faraday geometries (the two most common magnetic field configurations).

After a successful analysis, further experiments revealed the spin-qubits under non-standard field configurations can be manipulated with relative ease and only a minor impact on the efficacy of operations. Coherent control experiments were demonstrated with promising clarity and precision. Single-qubit tomography showed high fidelity initialization and reconstruction of the initial state of the spin-qubit. Finally, verification of geometric phase gates under oblique configurations confirms fur-

ther methods with which to control the spin-qubit state space.

By extending the body of knowledge under non-standard magnetic fields this work can directly apply to a wide variety of spin-based quantum systems grown using non-standard geometries such as pyramidal 1-1-1 quantum dots. Additionally, the enhanced understanding of quantum dots under non-standard magnetic field configurations allows more flexibility when adapting quantum dots for further applications and future research.

Acknowledgments

The work shown here is the culmination of an overwhelming amount of support and guidance I have received from the University of Strathclyde through which my entire higher education has been conducted. I want to being by saying thank you to Dr Konstantinos Lagoudakis who allowed me the opportunity to learn and develop while acting as my mentor throughout the entire PhD process. At the beginning he was there whenever needed and openly shared his knowledge with me in the process of developing the lab. This set up a strong foundation to build upon and later allowed the opportunity to further develop these skills on my own. This has resulted in a strengthened confidence and authority in this subject amd allowed me to produce this work.

There were many more staff at Strathclyde who have mentored and guided me over the year and it is not an easy task to name them all. In particular, I am grateful to both Andrew Daley and Stefan Kuhr who mentored me throughout my Advanced Research BSc and were always extremely supportive and helpful. They inspired me to develop my own intuition and expand my knowledge base which has fueled the curiosity that will continue to serve me well throughout my life. Overall, the stimulating environment that exists here at Strathclyde has created an unforgettable positive experience.

Beyond just these recent years, this work is actually the culmination of dedicated learning over a time span of close to ten years now. A non-trivial amount of this can certainly be related to the dedication and self-motivation I have been tirelessly working to develop. Yet I am also acutely aware that without the help and support of my family, my friends and mentors it simply wouldn't have been possible. The

support of some of the individuals named here (and many who could not be) has allowed me to rise from the lowest points in my life to my current situation. Upon reflection this support has allowed me to begin to realize my potential and I believe this will continue for a good while yet.

From my family I would like to show appreciation to my aunt Donna, my gran and my parents who have supported me from the lowest points in my life over a decade ago to where I am now. I believe out of all who know me they must take particular joy to see me get this far. They have always been available to listen, allow me to voice my opinions, answer my questions or just allow me the space to come to my own conclusions. All of this was freely given with an unconditional level of support and love.

I have also been gifted with a wide range of friends from all over the planet who have helped both directly and indirectly with my physical and mental well being. From the online physics community on Discord, Jkub and Chronum have always been around to discuss concepts and struggles relating to the physics while providing the chaos and joy required to weather the more personal ones. My oldest friend John has grown with me for over half our lives to date, Manos has embraced the coffee and physics chat for many years now and Davids self determination has helped to inspire me. Finally, I am extremely grateful for Matthew who has consistently been one of my closest friends and has given me the space to be myself while pushing me to embrace my identity and potential more than anyone I have ever known. This has allowed me to expand my mathematical and physics knowledge base, improve my programming skills, become a *no half bad* pianist all the while having a presence that has made dealing with lifes struggles manageable and in honesty, enjoyable. Additionally, he has provided most of the external proof reading for this work which has resulted in the high standard of presentation.

For the many who I have not named personally (and there are many), know that I am grateful for the presence, support, enjoyment and pleasure in life that you have provided. While not mentioned directly you have certainly not been forgotten. It certainly feels like my own personal universe is conspiring to help me achieve my

goals whatever they may be.

Words really cannae cut it but know I'm thankful tae every single one.

Contents

List of Authors Publications

- Operation of a continuous flow liquid helium magnetic microscopy cryostat as a closed cycle system - K. Barr, T. Cookson, K.G. Lagoudakis
  Review of Scientific Instruments (2021) DOI: 10.1063/5.0065560

- Towards spin state tailoring of charged excitons in InGaAs quantum dots using oblique magnetic fields - K. Barr, B. Hourahine, C. Schneider, S. Höfling, K.G. Lagoudakis
  Physical Review B (2024) DOI: 10.1103/physrevb.109.075433

List of Figures

List of Tables

Chapter 1

Introduction

The advent of quantum mechanics in the early 1900's has resulted in the most rapid and ongoing change in our understanding possibly in history. This has occurred on a range of levels; with general understanding that weird and wacky behaviors such as wave-particle duality and spooky action at a distance exist, and at a much deeper level that is arguably far stranger. Having now received formal training at the undergraduate and post-graduate level coupled with much self-study, this has only become more apparent.

Understanding natural phenomena through the lens of quantum mechanics required re-framing the intuitive classical causal relationship of *if A then B* towards a more probabilistic and statistical interpretation. Running an experiment on a quantum system under the same initial conditions will often produce different measurement outcomes. This is demonstrably not an artifact of experimental conditions but rather a property inherent to quantum mechanics itself. The predictability of quantum theory is thus found by averaging over statistically large ensembles to yield the correct results.

In light of this, quantum theory has proven to be extremely reliable and consistent resulting in a wealth of modern advances. Many of these have occurred over the past five decades as technology has improved. Most recently, the Nobel prize of 2022 was awarded to A. Aspect [1], J.F. Clauser [2] and A. Zeilinger [3] for their seminal experiments that covered a time span of almost fifty years. Their contributions cumu-

latively resulted in an unequivocal verification of quantum entanglement properties using Bells inequalities, for which the prize was awarded.

In 2012, S. Haroche [4–6] and D. Wineland [7] were awarded the prize for their cavity QED experiments using trapped ions. Each independently developed techniques to perform quantum non-demolition measurements, allowing physical observation of quantum phenomena on a never before seen scale.

While a vast amount of quantum theory was developed early on experimental verification has taken many decades since to obtain. This was further enforced with the 2005 Nobel prize being awarded to R. J. Glauber for his overwhelming theoretical contributions to the field of quantum optics. Among others, the impact of his theory on optical coherence [8], first published in 1963, could not be fully realized and appreciated until many years later.

The general message is that the peculiar behavior inherent to quantum mechanics has proven to yield widespread impact and applications to the modern world. As techniques and technologies continue to progress, successfully utilizing these properties, the benefits to wider society appear to show no signs of slowing down anytime soon.

Another rather recent area of research has been the field of quantum information [9,10]. This is a particular subset of physics that this work is closely related too. In the broadest terms, there are two main branches that attract the most resources which are quantum computation and quantum communication. Both show great promise in having significant impact on upcoming quantum technologies with current implementations well underway. This has attracted an overwhelming amount of active research and investment, time and resources here in the UK and throughout the wider world.

The UK itself is host to the Quantum Technologies hub consisting of four main areas of active research; Quantum Computing and Simulation, Quantum Communications, Quantum Sensors and Timing, and Quantum Enhanced Imaging. The purpose of the Quantum Technologies hub is to combine forefront academic research with industry applications, easing the process for forefront research to have imme-

diate impacts to wider society. The results presented in this work would fall under the quantum computing and simulation branch, although it is but a small portion of the wider ongoing research.

In this work, the contributions evolve from manipulating spins confined within semiconductor quantum dots. Electronic spins have long been considered potential candidates for spin-qubits. Qubits, quantum-based bits, being the fundamental building blocks in quantum computation and simulation.

An in-depth investigation combining characterization methods and experimental demonstrations of spin control with quantum dot systems has been performed. This has been to develop and reinforce the knowledge and techniques with which we can further enhance the manipulation and control of quantum dot systems. This is not necessarily quantum dot specific, spin manipulation can be performed in a wide range of quantum systems. Some examples are colloidal quantum dots, perovskites and 2D materials such as quantum wells and transition metal dichalcogenides (TMDs). The end goal is towards future applications, design architectures and hardware that can be used in upcoming quantum technologies.

As a general statement, the author believes the purpose of scientific research is a combination of pushing frontier boundaries, while filling in the gaps to improve our existing understanding. To this end, it is hoped that what is presented here is of sufficient quality and interest to the field. Additionally, that the effort and determination that went into this work makes it a contribution worthy of merit.

1.1 Quantum mechanics for computation and simulation

A key concept in quantum theory is the principal of superposition, a fundamental property opening up a wide range of possibilities classical systems cannot achieve. There are additional concepts related to the evolution of quantum states, which show a linearity with respect to the unitary state evolution after an operator is applied. Additionally, entanglement properties of both the internal system and also the wider environment play a role. The result is that probabilistic quantum systems can be solved

to show quite predictable behaviors following some base axioms.

The state space of a two-level quantum system spanned by the basis vectors $\{|0\rangle, |1\rangle\}$, assumed both normalized and orthogonal can be written as [11],

$$|\psi\rangle = c_0 |0\rangle + c_1 |1\rangle , \tag{1.1}$$

where c_0, c_1 are the probability amplitudes, complex numbers that obey the condition $|c_0|^2 + |c_1|^2 = 1$. The squared amplitudes are of significant importance as they define the probability of finding the system in a particular state, as postulated by Born. Since the probability amplitudes are complex then 1.1 can be written in the more generalized form,

$$|\psi\rangle = e^{i\eta}(\cos\theta/2\,|0\rangle + e^{i\varphi}\sin\theta/2\,|1\rangle). \tag{1.2}$$

Equation 1.2 is a description of a two-level quantum system and defines the properties of a qubit. The system can oscillate between $|0\rangle$ and $|1\rangle$ using θ and the states can develop a relative phase φ between them. The η parameter is related to an overall global phase which becomes important when working with multiple qubits. It is not relevant for this work which has a single-qubit focus.

From 1.2 we see that a single-qubit contains more information than a binary classical bit containing a 0 or 1. Upon an operator measurement, where we project the state onto a particular basis, it will still reveal only a binary outcome $|0\rangle$ or $|1\rangle$. Instead, the strength comes from the evolution of 1.2 in-between the initialization and the projective measurement. The benefits of this property are not immediately obvious, yet since the 1980's various quantum algorithms and proposals have been developed that take advantage of the superposition principal.

The general principle is that in utilizing the state space of the qubit during its evolution, yet prior to measurement, the time complexity of certain algorithms can be greatly enhanced. This would result in the quantum algorithms exhibiting time

complexities classical computations cannot rival. Some of the most prolific to date are Shor's factoring algorithm [12], Grover's search algorithm [13] and the Deutsch-Jozsa algorithm [14, 15].

For example, factoring large numbers classically and in big O notation can, in the worst case, scale at $\mathcal{O}(\sqrt{N})$. Shor's factoring algorithm could operate with a complexity of $\mathcal{O}(\log(N))$. Factorization of large numbers is of essential importance in modern day security and encryption which uses RSA encryption.

This naturally stimulated significant interest towards the physical realization of systems capable of performing these operations. The real challenge lies with developing physical systems that can maintain coherence on a large scale, while combating environmental interactions and noise sufficiently such that the error rates are not insurmountable. Just as much of quantum theory was developed before technological advancements allowed for their realization, quantum information technologies (in particular quantum computation) appear to follow a similar trend.

While complex quantum algorithms and computation indeed require solutions to the technical and engineering challenges before a full realization, quantum computation and simulation has many other applications that are relevant and already attainable. Quantum simulation is the principal of simulating complex microscopic systems to understand their behavior; this could be identifying electrons in materials, quantum disorder [16], spin dynamics [17–20], high-temperature superconductivity [21, 22], and many more.

Quantum computation and simulation is a broad field and in this work we can only touch on a small subset. For further information the author directs towards the following works [23–25].

With the advent of improved quantum hardware to apply towards computation and simulation, the possibility to unlock major economic opportunities present themselves. Near-term predictions believe that applications in quantum chemistry, finance, optimization and machine learning may reap many benefits within five to ten years [26].

This is dependent upon achieving *quantum advantage*, the point at which quantum

computation and simulation demonstrably out-scales classical computers for a particular problem. Realistically, attaining a *practical* quantum advantage [23] requires problems to be contextualized and interpreted appropriately. This is essential for near-term positive impacts on economics and society as a whole, ensuring applications along the path towards real quantum advantage.

While this work does not pertain to large scale computation or simulation the approach has been to extend the body of knowledge regarding spin-based qubits. That said, this work contributes firstly with the development of a state-of-the-art experiment, and further through the subsequent methods, techniques and experimental demonstrations contained within.

1.2 A brief introduction to quantum dots

The quantum system used here are semiconductor quantum dots which demonstrate potential across the quantum information sciences. In this work, we focus on the ground-state electron spins of negative singly-charged dots and harness them as a spin-qubit. This is but one of many different spin-state structures found in quantum dots which can be manipulated and controlled.

There are many excitonic structures (electron and hole quasi-particles) such as the neutral exciton, (positively- and negatively-) charged exciton, bi-exciton and dark/bright excitons which can be investigated. There have been many methods developed to characterize the structures, coherently manipulate the spins, and develop techniques for writing and readout of spin-based matter qubits. Additionally, they can be adapted to generate single-photons which can then be used in quantum communication technologies.

It has been observed that the dipole moment in quantum dots can be an order of magnitude greater than is common in atoms [27]. This leads to an enhancement in the coupling strength between light and matter. The interactions between light (photons) and spin-based systems (electrons, holes, excitons) can then be investigated, forming another rich field of physics. With the introduction of microcavities, small cavities

on the order of the wavelength of the light, with a high Q-factor, weak- and strong-coupling between the excitons and photons [28] can occur. In the strong-coupling regime the quasi-particle produced is called a polariton, though these quasi-particles are more commonly studied in 2D materials such as quantum wells and TMDs.

Additionally, quantum dots can be used to generate non-classical light, acting as both single-photon emitters and generators of entangled photons. Producing on-demand single photons of high indistinguishably is essential for quantum communication networks. With applications in quantum key distribution and cryptography such as the secure BB84 protocol [29].

With self-assembled quantum dots as the key type used in this work, this section explains aspects of the fabrication process using the Stranski-Krastanov (SK) growth mode. We then discuss quantum dots as spin-qubits by comparing their properties to DiVincenzo's criterion [30] for the physical realization of quantum computation. Finally, non-classical light generation is briefly covered to highlight other active areas of QD research. The techniques used for single-qubit control share overlap with QDs as single-photon emitters. Although the end goal differs, and so the optimization focus, the techniques are relevant across both areas.

1.2.1 Optically addressable spin-system architectures

The InGaAs quantum dots used in this work are one of the many spin-qubit architectures which offer strengths in the ability to be optically addressed. This aids the prospect of ultra-fast optical control capable of operation times many orders of magnitude longer than the coherence times. **III-V semiconductor quantum dots** are used in this work with InAs/GaAs being the most common. Some other notable III-IV compounds are As_ySb_{1-y}/GaP, GaSb/GaAs and GaN/AlN [31]. III-IV quantum dots generally form slightly larger QDs than the II-VI compounds [32]. This allows the formation of QDs at longer wavelengths with some works now pushing InAs/GaAs QDs into telecom wavelengths [33–35]. As these will be covered extensively in this work we mention some other notable systems that share similar physics with regard to optically addressable spin systems. In particular, **II-VI compound QDs** and point

defects such as **NV centres in diamond** are discussed. Both show great potential and comparison of these systems highlights strengths, weaknesses and the shared common ground among them.

II-VI compound quantum dots have also been investigated extensively over the years and have some associated benefits over the III-IV used in this work. II-VI compounds are most commonly seen to be formed from either CdTe/ZnTe or CdSe/ZnSe [32]. These form much smaller QDs leading to shorter wavelengths and benefit from emission in the short wavelength to visible regime [36].

Epitaxial II-VI QDs have been investigated with the inclusion of magnetic impurities through doping with Mn atoms [36–39]. These have been observed to show striking similarities to the charged QDs used in this work. The reduction of size in the quantum dots also leads to the localization sites of the charged particles interacting with less neighboring atomic nuclei. CdTe/ZnTe QDs contain approximately 5000 nuclear spins as opposed to 10^4-10^5 typical of InAs/GaAs [32]. This can result in a reduction of the Overhauser fields, with II-VI showing fields on the order of a few μeV compared to values > 100 μeV possible in III-V [40, 41]. While there are distinct differences, both the III-V and II-VI semiconductor QDs can be used as optically addressable spin-qubits as demonstrated in this work.

NV centres in diamond, and point defects more generally, are arguably one of the most unique of all optical spin systems. As all the systems here are spin systems they can be manipulated through a combination of electric and magnetic fields. Though in contrast to semiconductor QDs, NV centres exhibit zero-field splitting of the electronic levels and can be easily addressed through optical and microwave excitation [42].

The zero-field splitting an interesting property for spin-qubit applications due to allowing a significant reduction in the magnetic field strength, with systems requiring magnetic fields on the order of tens of mT [43]. While early works have shown two-qubit CROT between an NV center and a ^{13}C nuclear spin with a fidelity of 88.8% [44]. Additionally, observation of coherent population trapping [45] performed at liquid Helium temperatures lends well to the prospect of quantum information processing applications.

Perhaps one of the most striking aspects of NV centers is the ability to maintain these coherent properties even at room temperature. Electron spin coherence times of 58 μs [43] have been demonstrated alongside optical pumping and readout at room temperature. Incredibly, at room temperature this has been pushed as high as 350 μs [46] using Hahn-echo techniques.

Finally, similar to semiconductor quantum dots these systems are of interest for on-demand single photon generation which can be applied to quantum networks and repeater technologies. With a variety of research investigating the benefit of room temperature single-photon emitters [47–49].

Many other active areas of research of optically addressable spin systems exist and here we present only a few. Each system shows particular strengths from III-V QDs at telecom wavelengths, II-VI QDs showing reduced nuclear interactions and a broader spectrum towards UV/visible regions and NV centers capable of room temperature quantum effects. While in some sense these are competing architectures, the shared common ground within spin-physics leads to much of the advancements of a particular system benefiting the wider scientific community. We now move on to discuss in more detail the InGaAs quantum dots that are the focus of this work.

1.2.2 Growth using the Stranski-Krastanov growth mode

This section discusses some background information on the sample used throughout this work. Which are self-assembled InGaAs quantum dots formed using the Stranski-Krastanov (SK) growth mode. Fabrication of quantum dot heterostructures was not a part of this research hence we provide only a brief introduction.

Semiconductors quantum dots are heterostructures formed from crystals using a combination of different materials, in this case these are III-V compounds. With each compound exhibiting different valence and conduction band properties, combining them can result in the localization of electrons and holes leading to quantum confinement effects. The size and shape of quantum dots affect many different properties such as the emission wavelength where larger sizes often lead to longer wavelengths. They can be formed from compact shapes such as pyramids [50–54], dashes [55] and

of course, dots.

Different fabrication techniques exist such as the Stranski-Krastanov growth mode (as with this sample), droplet epitaxy (DE) and others. DE uses metal nanodroplets to stimulate formation of the quantum dot islands [56] and can allow more deterministic placement and control over dot density. We now focus on the SK growth mode in relation to the sample used here.

The process begins with a substrate layer, such as GaAs (001), as shown in figure 1.1(i). A distributed Bragg reflector layer can be introduced in the substrate prior to the dot formation (DBR in (i)) which helps reflect emitted photons towards the positive z-axis, improving the extraction efficiency. A DBR is a mirror structure consisting of alternating layers of dielectric materials with differing refractive indexes. This leads to near unit reflectivity within a desired wavelength range (∼910-920 nm for this sample).

Differing growth modes exist from layer-by-layer to island formation or a combination which characterizes the SK growth mode. Which growth mode occurs is a function of the interfatial free energy and the lattice mismatch of the compounds [57]. The SK growth mode occurs with a small value of the free energy and a large lattice mismatch [57]. The process begins layer-by-layer but when the strain energy of a thicker layer lowers the total energy, it leads to strain-induced 3D island formation.

The process to stimulate the SK growth mode is shown in figure 1.1(ii), an InGaAs wetting layer (WL) is grown with thickness h_{WL}. A dopant layer can also be introduced to assist in natively charging quantum dots. This sample contains a δ-dopant, commonly Be or Si, which can donate electrons to the quantum dots leading to negatively charged dots.

When the wetting layer exceeds a critical thickness, $h_{\mathrm{WL}} > h_{\mathrm{c}}$, the lattice mismatch creates strain energy causing the 3D island formation, indicative of the SK growth mode [56, 58], shown in figure 1.1(iii). This has been shown to work very effectively for InAs/GaAs quantum dots where the lattice constant of InAs is ∼7% greater than GaAs.

Finally, as in figure 1.1(iv), the sample is capped with another layer of the sub-

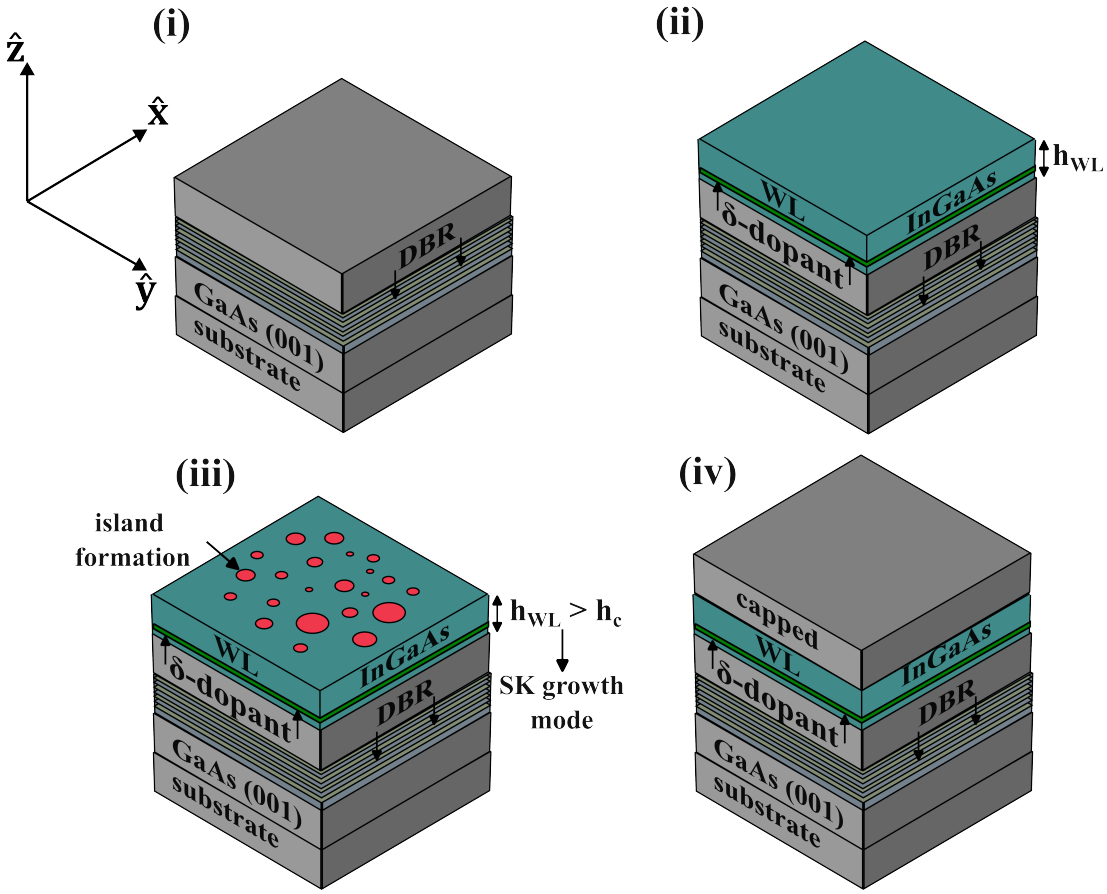

Figure 1.1: Self-assembled SK growth process. (i) Shows introduction of a GaAs(001) substrate and a DBR layer. (ii) An InGaAs wetting layer is grown with introduction of a δ-dopant layer to natively charge quantum dots. (iii) Island formation occurs whens $h_{\mathrm{WL}} > h_{\mathrm{c}}$. (iv) The sample is capped with the substrate material to complete the process.

strate material (GaAs), protecting the quantum dots and completing the process. The combination of the internal island formation and WL between the upper and lower substrate layer forms complete quantum dots which can localize electron and holes. As implied by the self-assembled term, the SK growth mode does not allow much degree of control over dot formation in terms of location, size, shape and strain. The size dispersion of dots throughout a sample is $\sim$10% in both SK and DE growth [56], leading the in-homogeneity within samples that is often observed. Even so, SK growth quantum dots have proven to be a powerhouse to generate high quality quantum dots for use in research and applications.

1.2.3 Harnessing a quantum dot as a spin-qubit

DiVincenzo stated five criterion to have a well-defined qubit state [30] to use for quantum computation. Physical realization of a system for quantum information processing should thus meet these requirements. As an aside, Loss and DiVincenzo were also some of the first to propose quantum computation with quantum dots as a physical qubit [59]. In this section we introduce the criterion and compare QD spin-qubit properties against them indicating some of their strengths and highlighting the weaknesses. The criterion were as follows [30],

1. A scalable physical system with well-characterized qubits.
2. The ability to initialize the qubits to an initial state.
3. Long decoherence times with respect to the gate operation times.
4. A universal set of quantum gates.
5. A reliable method to readout the state of the qubit.

The latter half of condition 1 , a well-characterized qubit, will be demonstrated repeatedly throughout this work, by experimental demonstrations of single-qubit rotations. The former of condition 1 can be fulfilled during the fabrication process as samples can exhibit high densities of $10^{10}/\text{cm}^2$ [194], with each QD being a potential spin-qubit candidate. Therefore, a highly scalable system of matter qubits exists if techniques to manage QD qubit selection exists.

The inclusion of a δ-dopant layer, such as Beryllium, increases the probability of excess donor electrons to be trapped within the QDs. This allows for native negatively-charged QDs, upon which much of the work presented in this thesis is focused on. Alternatively, application of a bias-voltage can allow for precise charge configurations such as a singly or doubly charged QD although this would require a gate-based approach.

The in-homogeneity of emission wavelengths, brightness and g-factors do prove challenging in this context. Tuning of such QD properties can be performed through

strain-induced [60, 61] and electric field tuning [62, 63] which provides some form of solution.

We will see that condition 2 is fulfilled through the spin pumping experiments shown later in chapters 4 and 5. The ground-state electron spins have been shown to be initialized in ∼3 ns [64] in InGaAs quantum dots. The quantum state tomography presented in chapter 6 also indirectly hints towards high initialization fidelities ($\mathcal{F}$ = 0.978) without explicit optimization of the process.

Condition 3 is one of key challenges limiting the physical implementations of quantum computation and is most prominent when attempting to scale up a system. This can be improved by either lengthening the decoherence times of the physical qubits or by increasing the speed of the gate operation times. Spin-qubits in QDs have been seen to have coherence times on the order of μs, with some variability dependent on whether an electron or hole spin is used. When demonstrating coherent control experiments using ground-state spins the methods and techniques applied on either an electron or hole are equivalent.

In terms of coherence times, hole spins have the benefit of the p-like symmetry of the wavefunction, reducing the effects of the Fermi contact hyperfine interaction with neighboring nuclei [65, 66]. Conversely electrons, with their s-like symmetry, will interact with the local nuclear environment. Hole spins exhibit long transverse relaxation times with measured T_2^* values in the range of hundreds of μs as demonstrated in [67, 68] and show long spin relaxation times of $T_1 \geq 180$ μs [69]. Electron spins are predicted capable of spin relaxation times up to ∼1 s [70] using techniques to reduce the strength of interactions with neighboring nuclei.

The true appeal with QD spin-qubits is that ultra-fast manipulations are possible using picosecond-pulsed light. This rapid generation of spin rotations is promising when compared with the coherence lifetimes. Within the QD coherence times we see that many gate operations could be applied within a single period, where 10^4-10^5 gate operations are possible. Coherent control using off-resonant pulses is a cornerstone of this work and exhibits an existing large body of research [34, 64, 71–74].

The universal set of quantum gates, condition 4 , presents the greatest challenge for

QD systems. This work alongside previous others, demonstrates that single-qubit rotations with QD spin-qubits are possible, efficient and highly controllable. A universal set of quantum gates at minimum requires single-qubit gates alongside the two-qubit CNOT gate. This is because any more complex set of quantum operations can be composed [30] solely from these gates. A reliable method to implement a two-qubit gate for quantum dots has yet to be found between two individual, distant quantum dots.

Implementation of a two-qubit controlled rotation (CROT) gate was shown on a bi-exciton structure within a single quantum dot [75] yet distant QDs cannot easily interact due to their weak dipole-dipole interactions [11]. Immamoglu. *et al* proposed a method to realize controlled interactions between distant QDs mediated by a high-Q microcavity [76] though a consistent method is still a challenge at present.

Finally condition 5 requires the ability to readout the state of the qubit. As QDs are strong emitters this can be performed through detection of single-photons in many cases. Investigations using different excitonic structures have identified methods of writing to a QD spin-qubit state and then perform efficient readout as in [77, 78].

We will show that the ultra-fast pulses rotate the spin using stimulated Raman adiabatic passage (STIRAP). While the excited stated contains a negligible population we are able to detect photons based upon the final state of the qubit at readout.

Applying the five criterion of DiVincenzo to QD spin-qubits and matching with the body of research that has been conducted indicates that QDs prove ideal candidates for single-qubits. Yet without a reliable method to mediate two-qubit gates they cannot be applied towards more advanced quantum computations. Regardless, single-qubit operations have many applications in quantum information processing. Additionally, many of the techniques described here are also applicable as excitation schemes for generation of single-photons with quantum dots.

1.2.4 Single-photon generation

Quantum communication is another major branch of quantum information that requires generation of entangled states of high purity and on-demand indistinguishable single-photon generation. This has applications in quantum key distribution, quan-

tum cryptography, quantum repeaters [79, 80] and wider quantum networks.

Generation of on-demand single-photons with high indistinguishably is essential for implementation of these applications. Error rates are known to increase significantly when the losses are great. QDs narrow linewidths and rapid recombination rates ($\sim$1 ns) yield properties that indicate generation of rapid on-demand single-photons. For a wider range of potential solid-state candidates we direct the reader to [81].

Flying-qubits (photons) can enable interactions between distant matter-qubits and it has been shown that their errors are manageable when the product of detector and source efficiencies $\eta_d \eta_s > 2/3$ [82]. This can be taken as a benchmark to aim for when evaluating extraction efficiencies from single-photon generators. This can be measured using techniques such as a Hong-Ou-Mandel (HOM) setup [83].

Generation of indistinguishable photons with physical systems is difficult as they all exhibit linewidth broadening and thus variance in the frequency of the emitted light. Many protocols require photons to be highly indistinguishable to reduce error rates. A fundamental requirement for highly indistinguishable photons is to have the linewidth approach the Fourier transform-limit [84].

A wide range of experiments with QDs have shown indistinguishabilties ranging from 0.970-0.995 in the best cases using various generation schemes. Some methods to generate on-demand single-photons with QDs are: continuous wave (CW) excitation [85], pulsed excitation schemes [85–87] (with similarities to coherent control), and adiabatic rapid passage [88] which demonstrated an indistinguishably of 0.995.

In conclusion, we introduced but a small portion of the large body of research presently active with semiconductor quantum dots. The Stranski-Krastanov (SK) growth method was introduced in relation to this works main sample. We then followed this by highlighting some key areas of quantum dot research, spin-based matter-qubits and single-photon generation. Having introduced some broader background knowledge we now move on to the main body.

1.3 Thesis direction

The outline of this thesis begins by discussing the experimental setup that was assembled over the first 16-18 months of this work. We then follow with a series of experimental results demonstrating coherent control of quantum dot spin states, first under standard, and then non-standard magnetic field configurations. Finally, we end with concluding remarks and a future outlook.

This begins with chapter 2 introducing foundational components of the experimental setup. These are essential equipment such as the cryo-magnetic environment, the range of lasers and the experiments measurement capabilities through spectrometry. Chapter 3 continues by focusing on specific aspects of the experimental setup required to manipulate a quantum dots spin state space. We show the techniques used to tailor mode-locked laser pulses for spin rotations and polarimetry setups that assist in both measurement and characterization.

Chapter 4 signifies the beginning of experimental data acquisition and includes background theory prior to experimental results harnessing charged quantum dots as a spin-qubit. These were all conducted under a Voigt magnetic field configuration. This reproduces previous results but was taken as an essential step equating to *calibrating the experiment*.

In chapter 5 charged quantum dots are investigated under non-standard, oblique magnetic field configurations. The level structures and selection rules of the system are verified through experimentally acquired parameters which aided the simulations. This reveals an understanding of charged quantum dots response to oblique magnetic fields, which could then be applied to produce the results of chapter 6.

The final results shown in chapter 6 builds on the knowledge and techniques gained from chapters 4 and 5 to extend spin-qubit control into oblique magnetic field configurations. We demonstrate coherent control of a charged quantum dot under this configuration, demonstrate some quantum state tomography and finally show that dressed states can still impart a geometric phase onto the spin state space, even under non-standard field configurations.

Final remarks and the conclusion of this work are found in chapter 7, where the implications of the research results are interpreted. Finally, the author highlights their perspective and ideas for future outlook with regards to extending the research.

Chapter 2

Foundations of the Experimental Setup

In this chapter we aim to provide a comprehensive introduction to the experimental setup used in this work. This was designed and built to allow for investigation and manipulation of spins confined to quantum dots. There are a wide variety of methods to control semiconductor quantum dot systems from electric fields, using optics and electronics, to application of magnetic fields.

Here, we address quantum dots optically using a variety of highly coherent laser light sources. By tuning the power, polarization and frequency of the light source a full range of control over the spin systems are possible. The confocal microscopy setup used allows us to address individual quantum dots.

An alternative approach is by application of electric fields such as in gate-defined quantum dot systems providing another much researched avenue. The source and drain setup allows the application of a bias voltage allowing a high degree of tunability of charge states within the QD, with a range of techniques for addressing states within [89–91].

Application of magnetic fields lifts the degeneracy of the spins and is an essential component for tailoring the spin states, revealing a range of rich level structures that can be adapted and used. With access to a 5 T superconducting magnet, investigating and tailoring these structures was possible.

Henceforth, we focus on optical manipulation of the quantum dots, often under strong magnetic fields, to demonstrate a high degree of control over the system. Future works looking to produce large scale quantum dot systems would most likely benefit by combining aspects of both optical and electrical control. On-chip applications should aim to combine knowledge from a broader range of areas such as photonic crystal structures, wave-guides and gate-defined quantum dot arrays. Coupling this with the electrically controlled architectures similar to modern non-quantum hardware appears to be a natural progression.

A (sometimes problematic) property of almost any quantum system is the high susceptibility to interaction with the environment. This inevitably affects the quantum mechanical properties leading to decoherence effects. These severely limit the timescale and quality of the systems performance when performing a variety of operations. When looking towards applications in quantum information processing, maintaining or lengthening this quantum coherence, or finding techniques to increase the number of operations within that timescale is a high priority.

This section begins by describing the considerations to minimize effects from the environment while optimizing the experimental performance. The foundations of the optical setup are then introduced, describing the lasers used in this work. Finally, the measurement and detection setup is shown which consists of a custom-built spectrometer capable of observing spectra using a CCD, or accurate count rates via single-photon counters.

2.1 Sample environment considerations

The quantum properties of quantum dots spin-states are fragile and shielding them from environmental interactions helps fight against decoherence. As a first step, lowering the samples temperature greatly reduces the impact of thermal effects that impact the quality of the system. As semiconductor quantum dots reside within a local solid state environment thermal excitations and other behaviors such as phonon associated coupling in the sample can be unavoidable. Fully accounting for these in-

teractions is difficult and when the effects become significant, both controlling and measuring the system can be challenging.

However, the introduction of a cryogenic environment helps to greatly limit thermal effects that can lead to noise and reduce coherence properties of the system. Thus, the samples are housed in a high-vacuum environment, on the order of 10^{-6}-10^{-7} mbar, while being maintained at cryogenic temperatures of around 6-10 K. The cryostat also allows for application of strong magnetic fields to lift the degeneracy of the spin-states.

The Microstat MO (*Oxford Instruments*) was specifically chosen for this purpose, being a continuous flow cryostat capable of generating high magnetic fields of up to 5 T. This is applied through the central axis of the sample chamber which can also be set to temperatures over a broad range (6-310 K).

During the assembly phase of the experiment, the system was modified to act as a closed-cycle system, allowing for re-circulation of Helium in the cryostat-manifold circuit. Other research groups [92] have invested in similar modifications to help circumvent high operational costs. Once successfully implemented, it was found the system could consistently go through many heating and cooling cycles on a single cylinder of helium. This has greatly reduced helium usage, both an expensive and scarce resource [93, 94], during normal operation. This has helped to reduce overheads and environmental impact of this experimental research.

In this section we describe the adaption process followed by a complete characterization of the system behavior. Furthermore, by performing a vibration analysis, the system performance was quantified after implementation of the closed-cycle transition.

We conclude that the system works to a high standard, allowing successful experiments on isolated quantum dot systems, while reducing the environmental and economic impacts of this work.

2.1.1 Closed-cycle components

The Microstat MO is a continuous flow, open-cycle cryostat containing a superconducting magnet. It is commonly used for cryo-microscopy experiments requiring the presence of strong magnetic fields. The magnet generates a maximum magnetic field of 5 T along the central axis of the sample chamber. The sample lies approximately 8 mm from the chamber window making it optically accessible using long distance microscope objectives [95]. The experiments operated through reflective measurements but the Microstat also allows for transmission setups as well.

Operation of the superconducting magnet requires magnet temperatures to be below 5.5 K for the magnet to retain its superconducting state. The open-cycle Microstat MO has a nominal liquid helium (LHe) consumption of $\sim$2 L/hr, equating to a cooling power requirement of $\sim$1.44 W, calculated from the latent heat of vaporization of helium.

By introduction of a commercially available cryocooler (*Coldedge Technologies, Stinger*), it was found that the high cooling requirement [95] for operation could still be achieved. The result of this was a successful transition from open to closed-cycle operation. Figure 2.1(a) shows a 3D rendering of the system showing the Stinger cryocooler which can produce 1.0 W of cooling power at 4.2 K. Helium is cooled by being forced through the cryocooler which then supplies the Microstat MO through a coaxial supply/return.

The complete circuit schematic can be seen in figure 2.1(b), the gas is forced through the system by a helium compressor (*Sumitomo HC-4E*) which is connected to a custom-built helium handling manifold. The closed-cycle circuit is completed by the manifold which connects the supply from the Stinger to the return of the cryostat.

The heart of the Stinger is a Sumitomo Gifford-McMahon (GM) cryocooler driven by a compressor (*Sumitomo F-70*). The cryocooler provides the bulk of the helium gas refrigeration prior to entering the cryostat via a corrugated transfer tube. Here, the flow undergoes Joule-Thomson expansion from 120 psi to atmospheric pressure at the end of the transfer tube. This results in further cooling yielding temperatures of 4 K or lower.

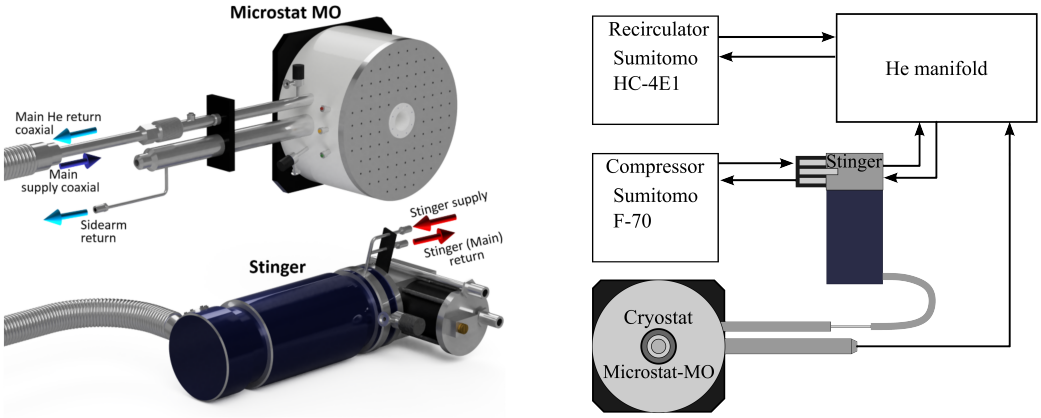

Figure 2.1: (a) Rendering of the cryostat (top) and stinger (bottom) combined system attached via a corrugated transfer line tube. The arrows depict the helium flow in and out of the system with the color associated to the relative temperatures (blue: base T, teal: intermediate T, red: room T). The red, yellow, and green dots on the cryostat casing are electronic connectors for monitoring the magnet and controlling the sample temperature. (b) Schematic diagram showing the entire cryostat-cryocooler circuit along with the associated compressors. The re-circulator is used in combination with the helium handling manifold to circulate helium in and out the stinger and cryostat. The stinger is cooled by a Gifford-McMahon cold head that is driven by the F-70 compressor. Thick arrows depict the helium flow direction in the flexible lines.

Operation of the superconducting magnet requires the magnet and sidearm components remain below 5.5 K and 35 K, respectively. A fine balance between the helium gas flow rates of the main and sidearm return paths is achieved by the custom-built helium manifold shown in figure 2.2.

In figure 2.2(a) the schematic of the internal connections is shown with locations of the valves, gauges and connections. The over-pressurization valves will vent if the system pressure exceeds 20 psi as an additional safety measure. The front panel design is highlighted in 2.2(b) showing the supply and return gauges, the flow meters and the valves which allow for control and monitoring of the circuit.

2.1.2 Temperature profiles of heating and cooling cycles

Cryogenic systems involve developing an understanding of the systems typical behavior and responses under certain conditions. Developing this intuition is essential in helping to minimize downtime if the system misbehaves, ensuring successful op-

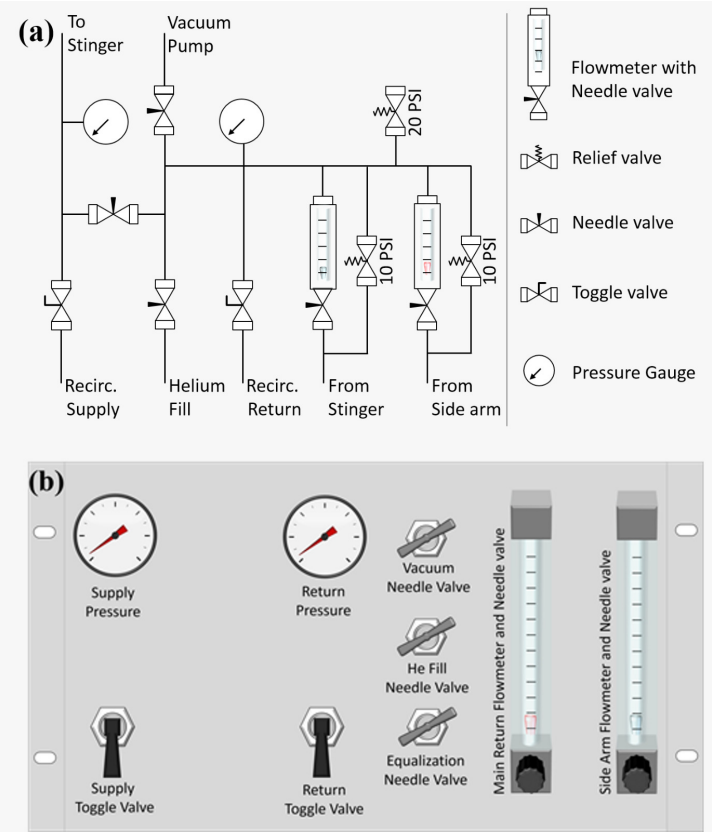

Figure 2.2: Custom built helium handling manifold developed for interfacing the Microstat MO cryostat with the stinger cryocooler. (a) Internal connection diagram. Bypass relief valves are connected in parallel with the flow-meters and a 20 psi relief valve venting to a room ensures the pressure is never above the value in the helium circuit of the cryostat. When opened, the equalization valve allows simultaneous pumping of the supply and return helium circuits. All lines that cross are connected. (b) Front panel design of the control manifold. Supply pressure gauge ranges from 0-160 psi, while the return gauge ranges from -30-60 psi.

eration. Cooling the system from room temperature towards base temperatures of around 6 K takes approximately 10-12 hours, whereas a complete heating cycle may take several days.

As these processes require significant time, finding early indicators of unsuccessful cycles allows for quick intervention. While testing the system, characterization of the temperature profiles allowed for detection of unsuccessful cooling cycles in as little as three hours. This knowledge allowed for quick reaction times resulting in increased performance and productivity with the system.

A typical cooling process begins by ensuring both the magnet casing and the manifold circuit are pumped to high vacuum using a turbo pump (*HiCube, Pfieffer*). Any contaminants within may freeze and block the circuit, affecting the helium flow rates, and preventing the magnet from reaching the required temperatures. High vacuum turbo pumps should aim for a vacuum on the order of 10^{-6}-10^{-7} mbar before initializing the system.

Initially the circuit is filled with helium pressurized in the range of 110-130 psi. The cryocooler will cool the circulated helium to base temperature at which point liquefaction of helium will gradually take place. This begins in the Stinger coldhead and later within the cryostat itself. This can cause a significant reduction in the overall pressure with as much as 50 psi lost as the process continues. By beginning with a high initial pressure the flow rates will remain high enough to maintain the cooling power after liquefaction.

Figure 2.3(a) shows a typical temperature profile during a cooling process for the main components of the setup; the Stinger, sample chamber, magnet and sidearm. Each are measured with temperature sensors which are monitored through a temperature control unit (*Mercury ITC, Oxford Instruments*). The Stingers temperature is measured using a separate sensor (*Model 211, Lakeshore*). The Stinger reaches base temperature of 6 K within 1.5 hours and the rest of the system then begins to follow.

For the next 6-8 hours the system steadily cools until approaching 50 K where a noticeable increase in the rate of cooling occurs that is most easily visible viewing the rate of temperature change in figure 2.3(b). This continues until reaching base temperatures around 10 hours into the cycle. The system can be operated from around the 10-12 hour mark and often some fine tuning of the main and sidearm flows are required. This is with the goal of ensuring the temperatures of both the magnet and sidearm are below the required 5.5 K and 35 K after activating the magnet.

The key metric for success is the rate of cooling and can be seen in 2.3(b), this measurement yields useful insight into the future system performance. The most important is dT_{mag}/dt which demonstrates the rate of change of the magnet temperature. During a successful run this should approach a peak rate of cooling of approximately

-0.8 K/min before tapering slowly towards a value of -0.4 K/min (but no higher) until the temperature of the magnet gets close to 50 K. From here a sharp increase in the rate of temperature change is seen until base temperatures are reached.

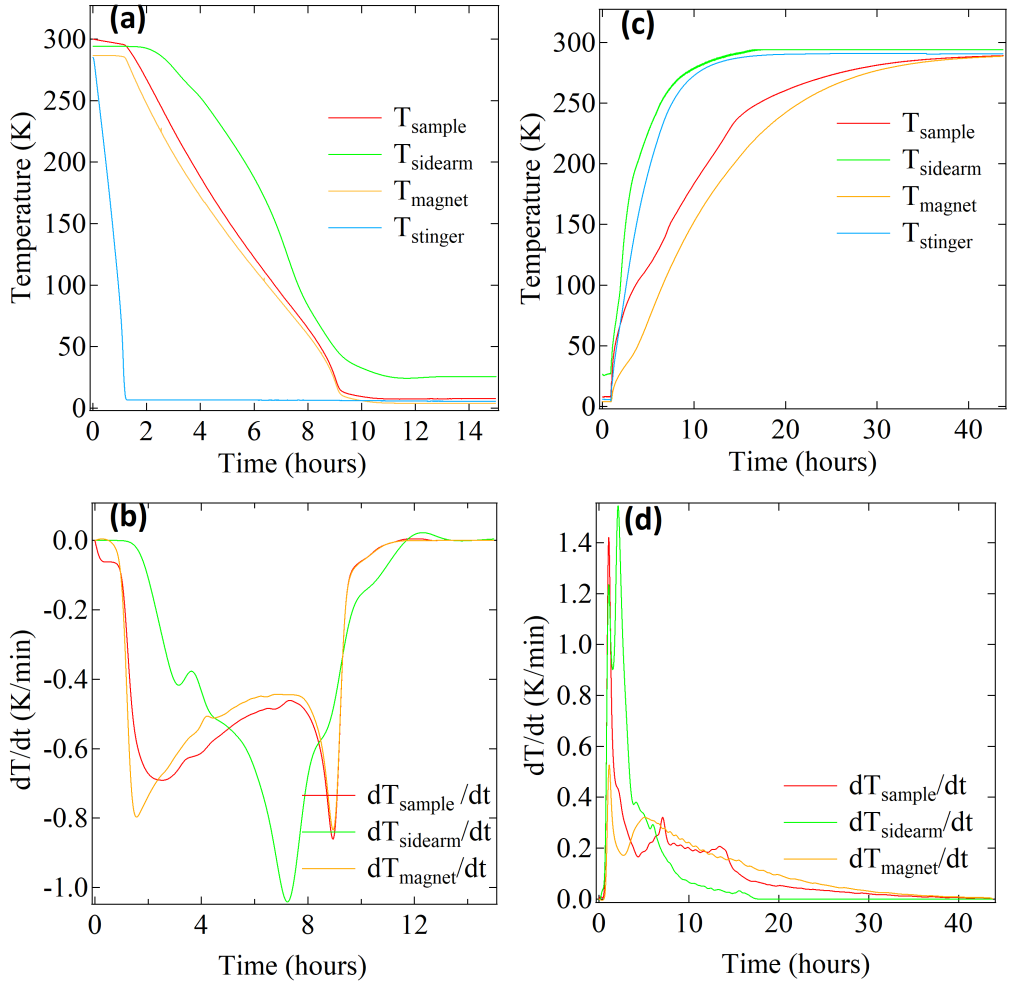

Figure 2.3: Cool-down and warm-up temperature profiles and rate of cooling for the system. (a) Temporal behavior of the cryostat temperatures during cool-down. The stinger reaches bases temperature within ∼1 h, after which the cryostat follows before reaching base temperatures around 10 hours. (b) Temperature gradients during cool-down in (a) for the sample, magnet, and sidearm. (c) Temporal behavior of cryostat temperatures and (d) temperature gradients for a warm-up for the three cryostat components. Typically requiring around 40 hours.

The heating process is considerably longer, as seen in figure 2.3(c)-(d), and is done

by turning off the Stinger and closing helium supply valve on the manifold. It can take around 35-40 hours to naturally reach room temperatures again without any intervention, during this time it is common to pump the manifold and Stinger to maintain a high vacuum. The sample chamber is equipped with a heater allowing the sample to go as high as 310 K whilst the magnet remains at cryogenic temperatures and provides a method of changing the sample without heating up the magnet.

Early diagnostics of a failed cooling cycle prevents wasted time and resources that occur when the system clogs. This typically occurs from air contamination within the helium circuit which then freezes at liquid helium temperatures leading to blockages within the circuit. The blockage results in a reduced flow rate, and thus cooling power, preventing operation of the magnet. This often manifests itself as the system reaching temperatures 3-5 K higher than required and if this happens the system needs to be heated and re-pumped to clear contaminants.

As highlighted earlier dT_{mag}/dt acts as an early diagnostic for a successful cooling cycle which is clearly identified in figure 2.4(a). The dashed red line indicates a failure due to contamination versus the successful orange line. The shallower gradient visible in 2.4(a) can be difficult to discern when observing the live data due to the long timescales.

Evaluation of dT_{mag}/dt makes this more clear as shown in figure 2.4(b). Once the stinger is cold and the magnet begins to cool the maximum rate achieved peaks relatively quickly before falling to a minimal cooling rate. The difference between dT_{mag}/dt and dT_{clog}/dt allows for quick intervention in as little as three hours. In this case, stopping the Stinger and pumping the circuit as the Stinger heats up to around 120 K helps to purify the circuit before resuming cooling.

2.1.3 Vibration analysis of the closed-cycle system

As a closed-cycle system requires the presence of a cryocooler, introduction of significant vibrations is an issue of concern for experimental applications. For the system discussed here, the Stinger coldhead and the compressors will generate noise and vibrations that may affect experiments. Addressing individual quantum dots optically

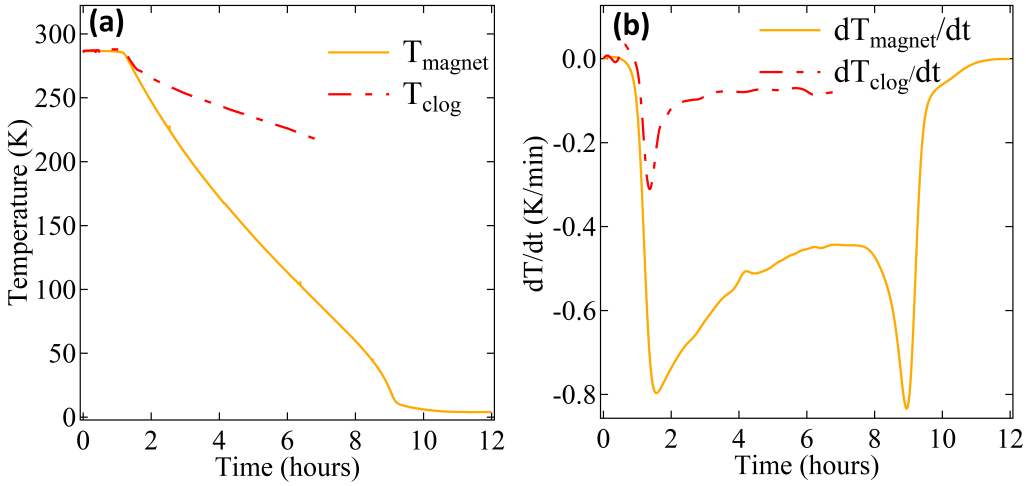

Figure 2.4: (a) Temperature profiles of the cryostat under a successful cooling cycle (orange) compared with the presence of air contamination (red, dashed) indicating the much lower rate of cooling. (b) Gradients showing the rate of change of cooling seen in (a) highlighting the significant difference. Acquisition of the clog (red) data was interrupted after 7 h for the air contaminated case.

require lasers focused down to micrometer scales. Quantifying the vibrations that propagate from mechanical components through to the sample chamber allowed for actions to be taken to minimize the effects.

The adaption towards a closed-cycle system naturally introduces vibrations to the sample holder in numerous ways. The dominant predicted channel is through the mechanical coupling of the cryostat to the cryocooler through a corrugated flexible helium transfer tube. The two compressors shown in figure 2.1(b) will also produce significant acoustic vibrations. There exist several methods to characterize the vibrations in cryogenic environments [96–99] but the method chosen here was an interferometric approach [99, 100].

To reduce the acoustic noise picked up by the interferometer, the compressors were enclosed within a custom casing of aluminium dibond panels padded by 25 mm thick class 'O' acoustic foam. To further reduce the residual acoustic noise from the compressor and re-circulator, they were placed in an adjacent plant room to isolate them from the optical setup.

The cryocooler itself is mechanically coupled to the cryostat and due to the finite length of the helium transfer tube must be located nearby. The Stinger is found under the optical bench but was also enclosed in aluminium dibond padded with the same class 'O' acoustic foam. This proved significant in combating vibrations as measurements from the interferometer showed a reduction of approximately a factor of 2 after implementation. The helium transfer tube was also clamped to the optical table and padded by a layer of acoustic foam at the contact point. This helped to further damp vibrations as it enters onto the optical setup.

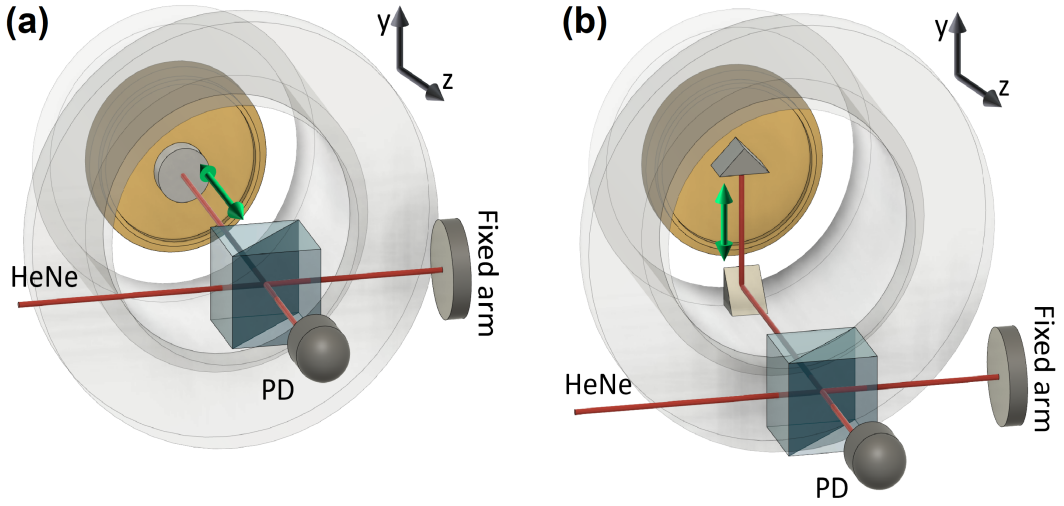

Figure 2.5: Schematics of the Michelson interferometer setups used to determine vibrations in both the z- and y-directions. The sample holder is depicted as the brass colored cylindrical base inside the sample well. (a) Michelson configuration used to evaluate vibrations along the z-direction as indicated by the green arrows. (b) Michelson configuration for measurement of vibrations along y-direction. The bottom silver coated prism is directly attached to the sample well (cryostat casing). Green arrow indicates the sensitive measurement axis.

For the interferometric vibration measurements a custom-built frequency stabilized helium neon laser was used in both Michelson setups depicted in figure 2.5. Each one, (a) and (b), measured vibrations in the z- and y-direction, respectively. The vibrations show up as intensity fluctuations on the photo-diode signal and given the known wavelength of the laser (632.8 nm) with the geometry of the system they can be directly converted to a displacement. To pass from constructive to destructive in-

terference in both setups requires a $\lambda/4$ displacement of the sample holder resulting from the double pass of the laser beam to and from the sample holder.

Each setup contains a fixed arm coupled directly to the optical table and an arm directly connected to the sample chamber itself. The highest sensitivity of these signals will occur away from the extremum of the interference signal so we ensured each interferometric measurements was taken within a 30-70% band of the peak to peak interference fringe amplitude.

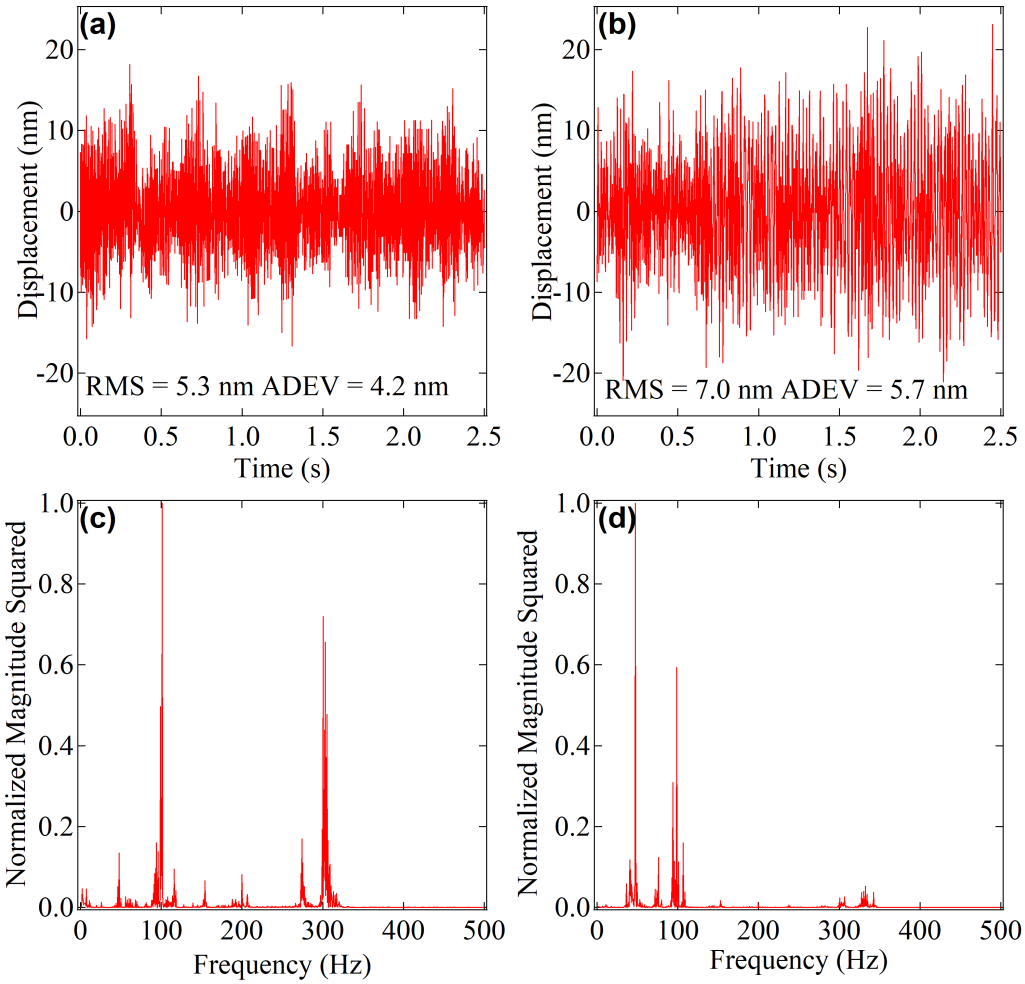

Figure 2.6: (a) Time trace of the sample holder displacement along the z-direction. (b) Time trace of the sample holder displacement along the y-direction. (c) Normalized magnitude squared of the Fourier transform for the time trace shown in (a) showing dominant frequencies at 101 Hz and 300 Hz (d) Normalized magnitude squared of the Fourier transform for the y-direction time trace shown in (b).

The setup in figure 2.5(a) measures the vibrations in the z-direction along the optical axis of the cryostat indicated by the green arrows. Post-processing to remove any slow signal variations [95] ($\nu < 0.10$ Hz) were performed using a boxcar smoothing algorithm. The root mean square (d_{rms}) and average deviation (d_{adev}) for the displacement d were evaluated using,

$$d_{\text{rms}} = \sqrt{\frac{1}{N}\sum_i d_i^2}, \tag{2.1}$$

$$d_{\text{adev}} = \frac{1}{N}\sum_i |d_i - \bar{d}|, \tag{2.2}$$

where N is the number of data points and $\bar{d}$ is the average displacement. Figure 2.6(a) shows typical vibrations along the z-direction showing a peak to peak amplitude of ∼30 nm. The root mean square value was $d^z_{\text{rms}} \approx 5$ nm and the average displacement $d^z_{\text{adev}} \approx 4$ nm. Taking the Fast Fourier Transform (FFT) of the time trace revealed peak contributing frequencies and is shown in figure 2.6(c). Interestingly, the signal does not feature a significant peak at 2 Hz that is typical of mechanical motion from the GM cryocooler in the stinger, instead there are two dominant vibrational frequencies at 101 Hz and 300 Hz.

The y-direction vibrations, measured vertically with respect to the optical axis of the cryostat, were measured by implementing a slightly modified setup as seen in figure 2.5(b). This was sensitive to vibrations in the y-direction indicated by the green arrows. The measurements revealed slightly larger values than the z-direction in both the interference signal and frequency spectra as shown in figures 2.6(b) and (d), respectively. We found a peak to peak value of ∼40 nm, with $d^y_{\text{rms}} \approx 7$ nm and $d^y_{\text{adev}} \approx 6$ nm along the y-direction. There were also two dominant frequencies found at 47 Hz and 98 Hz as seen in the Fourier spectra in figure 2.6(d).

The data was taken at base cryogenic temperatures with the sample chamber held at ∼8 K and the cryocooler active to simulate experimental conditions. Comparative measurements were also taken with the cryocooler turned off while at cryogenic temperatures to reveal the baseline vibrations for the system and the lab. The values here

were found be ∼4 nm peak to peak, with $d_{\text{rms}} \approx 1.4$ nm and $d_{\text{adev}} \approx 1.1$ nm.

The measurements indicate that the transition from open to closed-cycle operation introduces system vibrations with peak to peak values of ∼30-40 nm with root mean square and average deviations of ∼5 nm in both the y- and z-directions. With values in the 1-10's of nanometer ranges the transition to closed-cycle can be said to have been successful. The original concerns were that the introduced vibrations could be as much as 10-100x larger than what was observed. In this case, the likelihood of vibrations significantly altering the power transfer from a focused optical beam onto a quantum dot during single qubit operations would be much greater. Such variations in power transfer can have a significant effect when manipulating spins contained in quantum dots.

If this had proven significant enough it may have resulted in abandoning the closed-cycle transition completely. Thankfully, the result of the investigation performed here indicated that the system should prove suitable for the experiments ahead.

2.2 Excitation Setup

Throughout this work manipulations on the quantum dot spin states are conducted using highly focused, narrow-linewidth beams. There are three main methods of optical excitation in this work described as follows; addressing transitions using continuous wave, narrow-linewidth beams for processes such as spin initialization, application of ultra-fast picosecond laser pulses essential for single-qubit gates and rotations, and above-band excitation used to generate quantum dot photo-luminescence.

Unlike atomic systems in which the characteristics of an ensemble of the species are identical, semiconductor quantum dots often vary due to the spread of size and strain distributions [56, 57, 101, 102]. Growth of a quantum dot sample, such as the self-assembled sample used throughout this work, inevitably leads to a non-uniform distribution even when using well developed methods [56, 57, 101–105].

Regardless, the in-homogeneous broadening leads to variations across the same sample with each quantum dot yielding unique characteristics. This can vary from

central peak wavelengths and emission properties to electron and hole g-factors. As a result, manipulation of quantum dots requires lasers that are highly tunable across a range of wavelengths. In this section we introduce the essential optical components used extensively throughout the rest of this work.

2.2.1 Continuous wave and pulsed excitation lasers

Typical linewidths of quantum dots energies are on the order of 1-10s of μeV or 1-10s of GHz in the frequency domain. This then requires narrow-linewidth lasers to address them that also have sufficient wavelength tunability. A common workhorse, and used in this work, is the titanium-doped sapphire (Ti:sapphire) solid-state laser providing wavelength tuning over a broad range of the near-infrared (NIR) spectrum. Both the resonant and pulsed excitation used contain a Ti:sapphire rod and optics that form a resonator cavity to promote lasing.

The three main lasers within the setup are shown in figure 2.7(b): the 532 nm pump laser (*Millennia eV, Spectra Physics*) powers both the continuous wave (CW) Ti:sapphire (*MBR-110, Coherent*) and the mode-locked pulsed Ti:sapphire (*Tsunami, Spectra Physics*).

A Ti:sapphire rod lases by the introduction of a small concentration, typically 0.1-0.5 % by weight, of Ti^{3+} ions into the material. The ground states of these ions splits into a pair of vibrationally broadened levels yielding different spectral bands. The absorption band lies within the approximate region of 350-650 nm while the fluorescence band is around 600-1080 nm. Due to the slight overlap of these bands the lasing emission range lies from 675-1080 nm though often the laser will be setup for emission in some subset of the total range. To stimulate lasing the Ti:sapphire lasers require a high intensity pump laser (532 nm) to generate a round-trip gain greater than the round-trip losses from all sources.

The pump laser model used is a 532 nm (CW) diode-pumped solid-state (DPSS) laser capable of outputting up to 20 W with a stability of $\pm 1\%$ [106]. Figure 2.7(b) shows how the output is split to act as a pump source for both the resonant and pulsed lasers Ti:sapphire lasers. The intensity division to each laser is tailored using optics

inside the enclosed box prior to the pulsed (Tsunami) and CW (MBR) input.

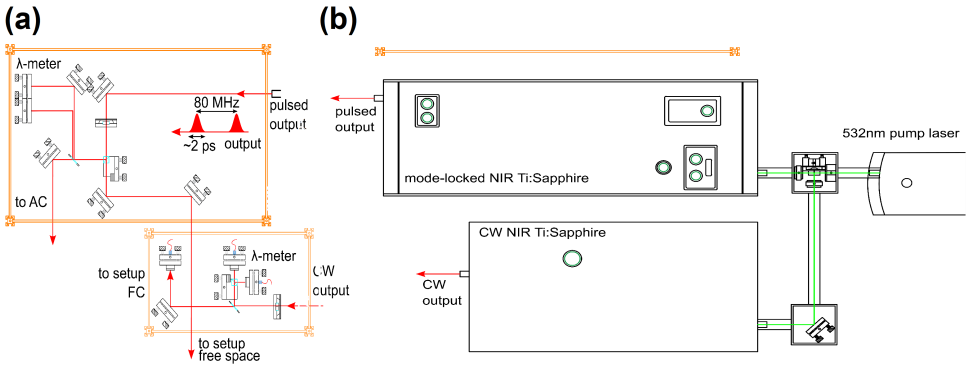

Figure 2.7: (a) Optics of the pulsed (top enclosure) and CW (bottom enclosure) from laser shown in (b). *Pulsed output* passes through waveplate/polarizer combination to control power. One path goes to an auto-correlator (AC) to aid in mode-locking, a 4% reflective glass plate sends light onto a wavemeter. Free space path leads to experimental setup. *CW output* contains similar waveplate/polarizer combination for power control, 4% reflective glass plate passes onto wavemeter and an additional spare output. Light is passed through a fiber-couple (FC) onto experimental setup. (b) 532 nm green laser (right) pumps both pulsed and CW with up to 20 W, waveplate/polarizing elements allow power to be divided across both as required. Outputs of pulsed and CW (left) lead onto optics in (a).

With the CW laser receiving approximately 9 W pump power the output power ranges between 0.8-1.1 W with a wavelength range around 700-950 nm. The output straight from the CW laser is shown in figure 2.7(a) (bottom enclosure). This passes through a combination of a waveplate/polarizer combination allowing control over the output power. A reflective glass plate sends 4% of light onto a single-mode fiber-couple leading to a wavemeter (*Fizeau Wavemeter, Moglabs*). An additional fiber-couple was also setup for future expansion of the lab. The transmitted light leads onto a single-mode fiber with an achromatic lens, optimized for NIR wavelengths, which is then sent directly onto the experimental setup. The CW can be coarsely tuned via a knob on the laser as in figure 2.7(b) or can be electrically/manually controlled with higher resolution detuning over a 40 GHz range.

The Tsunami, pictured at the top of figure 2.7(b), is a mode-locked Ti:sapphire laser that produces a train of high power, ultra-fast pulses at a repetition rate of ∼80 MHz

equating to roughly one pulse every 12.5 ns. The system can be setup to produce pulses in a picosecond or femtosecond regime by changing the internal optics of the resonator cavity.

The cavity contains Brewster angled surfaces to improve the gain of only selected wavelengths and polarization of light. For femtosecond operation wavelength tuning requires a prism sequence and slit in-built into the cavity which can be introduced into the beam path. Picosecond operation instead requires a birefringent filter (bifi) inserted into the beam path orientated at Brewsters angle. In this work the laser was setup to operate in the picosecond regime.

At the top of figure 2.7(a) we see the system generates picosecond pulses with a full-width half maximum (FWHM) of approximately 2-3 ps. The bifi in this regime transforms transmitted polarized light from linear to elliptical where only a narrow range of wavelengths will gain an $n\pi$ phase shift to remain linearly polarized. This wavelength range is a function of the bifi orientation and only these wavelengths maintain sufficient gain to continue lasing. The remaining wavelengths will suffer a loss incurred from each Brewster surface within the cavity. When the loss exceeds the round trip gain the wavelengths will then die out. This yields a means of tuning the wavelength of the pulse train in the picosecond regime.

Selection of the pulse-width is dependent on material properties of the Ti:sapphire rod and the cavity parameters so only the cavity parameters are easily modified in the lab. Once the system is mode-locked the ultra-fast pulses generated are restricted by the time-bandwidth product for pulses. This is related to the Heisenberg frequency-time uncertainty relation [107] which states that as the pulse duration narrows the bandwidth of the frequency inversely adapts to maintain the relation.

The frequency difference throughout the pulse leads to effects such as self-phase modulation, resulting in different frequencies experiencing varying indexes of refraction as they propagate leading to pulse broadening. This is defined by a positive value of the group velocity dispersion (GVD) and must be counteracted to produce stable pulsing. In picosecond operation the introduction of a Gires-Tournois interferometer (GTI) introduces a negative GVD to counteract these effects and is a key component

for alignment to produce pulses with FWHM in the region of 2-3 ps.

To improve the ease of mode-locking the laser, allowing the laser to run approximately 1-2 hours prior will give sufficient time for the temperature gradients to stabilize. Once the central wavelength is close to the desired wavelength we manipulate the GTI and the front and back cavity mirrors of the Tsunami while observing the output on an auto-correlator (*Pulse check auto-correlator, APE*).

The first step is to manipulate both the GTI and phase knobs located on the electronics system to maximize the auto-correlator signal. Then front and back mirrors of the Tsunami cavity are finely tuned with the goal of causing the auto-correlator signal to become as noisy as possible. A noisy signal on the pulse checker indicates that the system is moving closer towards pulsing. By iterating between altering the GTI/phase to maximize background and then GTI/cavity alignment to increase the noise the system will pulse. A successful locking leads to a clean Gaussian peak on the auto-correlator.

Some additional notes, once pulsing the central wavelength of the pulse can be shifted by $\sim$0.5 nm but must be done so adiabatically. Also when maximizing the background on the pulse checker with the GTI there are usually multiple locations across the GTI tuning range where these maxima will occur. This is a result of the periodic nature of the resonator.

2.2.2 Above-band excitation

Above-band excitation is a common technique to observe the photo-luminescence (PL) in semiconductor systems such as quantum dots. Exciting the system at an energy well above the band-gap excites carriers throughout the wetting layer of the material. This leads to a cascading excitation/decay effect that populates the quantum dots levels causing photo-luminescence. The PL spectra can then be collected as the above-band laser spot is scanned across the sample to observe the QDs. For this purpose, a 780 nm laser diode that is sent through a polarization maintaining single-mode fiber is used.

The PL spectra of quantum dots yields numerous methods of characterizing the system; from above-band power dependence [108, 109] to polarization-resolved PL

using either half-wave or quarter-wave plate polarimetry.

2.3 Detection and measurement

To successfully probe the dynamics of quantum dot systems requires detection of single photons emitted from individual quantum dot transitions. The setup was designed to contain two main elements for detection of emitted single photons, the first allows one to resolve micro-photoluminescence (μ-PL) spectra by means of a highly sensitive NIR CCD camera (*iDus 416, Andor*). The second elements are single-photon counting modules (SPCMs) (*SPCM-AQRH-44, Excelitas*) which are used for accurate photon counting for low light levels.

Both detectors require minimal background counts from external sources due to their sensitivity. Thus, it is essential the detectors are contained in well sealed light-proof enclosures to minimize background counts. To resolve QD spectra we require a high resolution spectrometer that can diffract light from a central wavelength to send directly onto the CCD camera or the active area of the SPCM. For this purpose, a custom-built and designed spectrometer was implemented and is discussed shortly.

The iDus 416 CCD contains an active area of 2000 x 256 pixels, each 15 μm x 15 μm in size, allowing for a wide angle of acceptance for diffracted light. In-built cooling allows temperatures down to -70°C which minimizes dark counts and reduces the overall background noise of the signal. The camera is integrated programmatically through a LabView VI (VI's are LabViews file type) that controls all aspects of the camera and spectrometer system. The VI can control camera temperature and integration times and the wavelength and resolution from connections to motorized stages in the spectrometer.

2.3.1 Implementing a spectrometer

As mentioned linewidths of QDs are on the order of 1-10's of μeV and so high spectral resolution is required to resolve individual spectra. Improving the quality of spectral measurement is done through combination of factors from the focal length of the

spectrometer arms, the surface area, grooves / mm and the choice of diffraction grating [110].

For the setup, a double Czerny-Turner monochromator was implemented in line with the annotated CAD schematic of figure 2.8. The Czerny-Turner (C-T) design consists of a diffraction grating and two concave mirrors, the collimating and focusing mirror, as seen in figure 2.8. Each monochromator contains an aluminium, plano-ruled diffraction grating with; 1800 grooves / mm, blaze angle of 26.75°, a blaze wavelength of 60 μm, and 110 x 110 mm active area (*Plano Ruled - 53015 BK01-290R, Richardson Gratings*). For S-plane polarized incident light the grating demonstrates an optimized efficiency of 90% over the 900-970 nm range ideal for the wavelengths used in this work.

Incident light is focused with a 50 mm lens through the entrance slit and travels for F = 1 m before the concave spherical mirror collimates the beam onto the first grating G1. The diffracted light is then refocused by a focusing mirror before being sent through the motorized intermediate slit. The process repeats through the second configuration until the final F = 1 m path from the focusing mirror. This output can now be passed onto two possible detector outputs.

If the flip mirror (FM) is outwith the beam path the light will pass onto the active area of the CCD camera showing the wavelength spectra through the LabView VI. Alternatively, activating the flip mirror sends the path to an exit slit where the output is then collimated and sent onto the active area of the SPCM detectors for single-photon detection.

The VI controls all aspects of the spectrometer from the CCD, to all the motorized elements such as the rotation stage mounted gratings, the flip mirrors and intermediate slits. Each identical grating, G1 and G2, are mounted on motorized rotation stages allowing precise control of the grating angle which in turn controls the central wavelength directed to the detectors. The motors are configured to operate in half-steps yielding 144,000 steps per complete 360° revolution.

The VI was modified to allow for the signal that falls upon the two-dimensional CCD active area to be integrated over the vertical pixels resulting in a one-dimensional

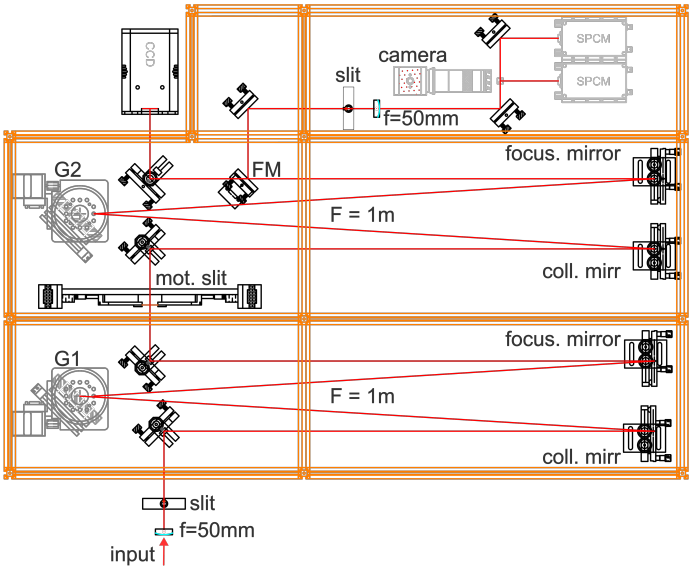

Figure 2.8: To scale CAD drawing of the double C-T monochromator implemented for this work. Incident light is focused by an f = 50mm lens onto the entrance slit before passing through each arm of F = 1m. Gratings G1 and G2 are mounted on motorized rotation stages, the intermediate slit is also motorized. Flip mirror (FM) at final output allows the output to be sent to either the CCD camera (pictured left) or towards the SPCM setup (pictured right) for either spectra or number measurements.

intensity vs wavelength spectra. Calibration of the spectrometer involves matching both G1 and G2 by order and central wavelength alongside the pixel to wavelength conversion of the CCD camera. Successful calibration yields a highly efficient, well-resolved spectra on the CCD output.

To test the absolute efficiency, the CW laser (λ = 910.33 nm, in line with the wavelength of the QDs) was introduced with the polarization optimized to be perpendicular to the gratings. Power measurements at the input slit and the exit slit of either one, or both monochromators, were taken using all combinations of diffraction order for G1 and G2. The diagram in figure 2.9 demonstrates the setup where P_{in} is the input slit measurement, while $P1_{\text{out}}$ and $P2_{\text{out}}$ determined the efficiency of either one or both monochromators together.

The results shown in table 2.1 were taken with the CW laser with an input power of 2.95 mW at 910.33 nm. Using only the G1 monochromator to 1st order, $P1_{\text{out}}$ demonstrates an absolute efficiency of 66.8% resulting in 2/3 photons surviving. Using both

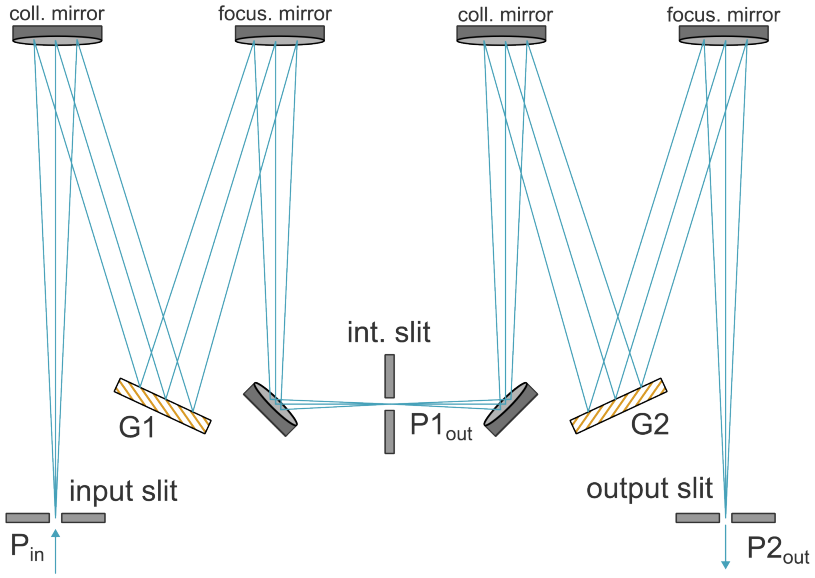

Figure 2.9: Schematic of the double monochromator configuration similar to the actual physical implementation. Power measurements were taken at P_{in}, $P1_{out}$ and $P2_{out}$ with low levels of background light within the laboratory. Data was then collated to determine efficiencies of the complete measurement device.

G1 and G2 in $P2_{out}$ demonstrates that after calibration an absolute efficiency of 50.8% at 1st order, losing 1/2 photons for detection. To maintain such an efficiency at the output is a great achievement that proved useful for experiments in subsequent chapters. When coupled with the reduction in background counts due to the double configuration an excellent signal to noise ratio was obtained.

The resolution of the spectrometer was measured through application of the narrow linewidth CW laser on the CCD pixel array which was then fitted as shown in figure 2.10. From the fit the FWHM Γ was evaluated in terms of both pixels and energy. We find the pixel FHWM to be $\Gamma_{\text{pixel}} = 2.56 \pm 0.14$ and the energy FHWM as $\Gamma_{\text{energy}} \approx 8\,\mu$eV equating to $2.88\,\mu$eV / pixel. This value has appeared consistent as will be shown on the dressed state measurements in chapter 6.

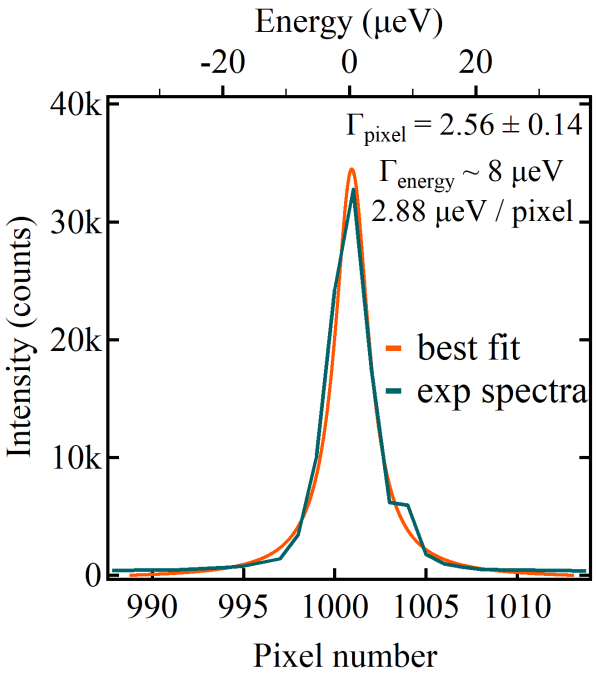

Figure 2.10: Experimental spectra (green) and best fit (orange) of the CW laser on the CCD pixel array with the bottom axis showing the pixel number of the 2000 pixel length array, the top shows the equivalent energy in μeV. FHWM values of Γ_{pixel} and Γ_{energy} are shown in the text.

	G1	G2	Power (mW)	Efficiency (%)
	(Order)			
P_{in}	-	-	2.95	-
$P1_{out}$	0	-	0.41	13.9
	1	-	1.97	66.8
$P2_{out}$	0	0	0.21	7.1
	0	1	0.95	10.8
	1	0	0.95	32.2
	1	1	1.50	50.8

Table 2.1: Efficiency data collected based on the setup in figure 2.9, initial input power of 2.95 mW recorded with a final output of 1.50 mW with G1 and G2 at first order. Additional grating configurations highlight the optimized efficiency of the gratings whilst at a 1st order diffraction.

2.4 Conclusion

This section discussed the importance of a finely tuned environment and the steps that were taken to ensure quantum systems are protected from undesirable effects resulting from external sources. Additionally, the essential components making addressing individual QDs capable via continuous wave, pulsed or above-band excitation were introduced and an explanation of the sensitivity of the detectors that operate at a single-photon level was provided. The equipment was chosen such that it allowed for high efficiency throughput with a good degree of spectral resolution. Subsequent chapters aim to show how these elements are combined to conduct complex manipulations on the single spins confined to QD structures.

Chapter 3

Tailoring an Experiment towards Coherent Control

Chapter 2 introduced some of the essential components found in many modern optics labs. This chapter now brings the setup into context for optical single-qubit control by introducing the additional requirements and challenges. We aim to isolate, excite and detect single quantum dots and apply laser pulses as a function of power and time delay. This is while simultaneously optimizing photo-luminescence and minimizing background noise from other sources.

The chapter is structured as follows: first we describe the magneto-optical setup consisting of confocal microscopy and an opto-mechanical setup. The microscopy setup helps to target single quantum dots, while the opto-mechanical setup allows precise control over the incident laser light. We then introduce two forms of polarimetry, rotating half- and quarter-wave setups, indicating individual strengths and highlighting some challenges faced during implementation. Finally, we discuss methods to tailor the ultra-fast picosecond-pulses which are used to generate spin rotations between the electronic ground-states quantum dots. This involves descriptions of designs for the spectral filter and an unbalanced Mach-Zehnder delay stage.

3.1 Magneto-optical setup

From the magneto-cryostat introduced in chapter 2 we access the sample through a window in front of which the confocal microscopy setup is built. Both excitation and detection occur along the same path in a reflective configuration, and here we present an overview of the implemented optical design.

Figure 3.1(a) separates the system into three main components that complete the setup. Box (1) in 3.1(a) contains the *excitation/optical driving setup* through which the lasers from section 2.2 enter. This contains the additional optics required to precisely control the power and polarizations of the incident light. Each laser input is aligned onto the same beam path prior to being focused on to the sample surface through a microscope objective. The objective can be translated along all three principal axes using a custom-built xyz-translation stage.

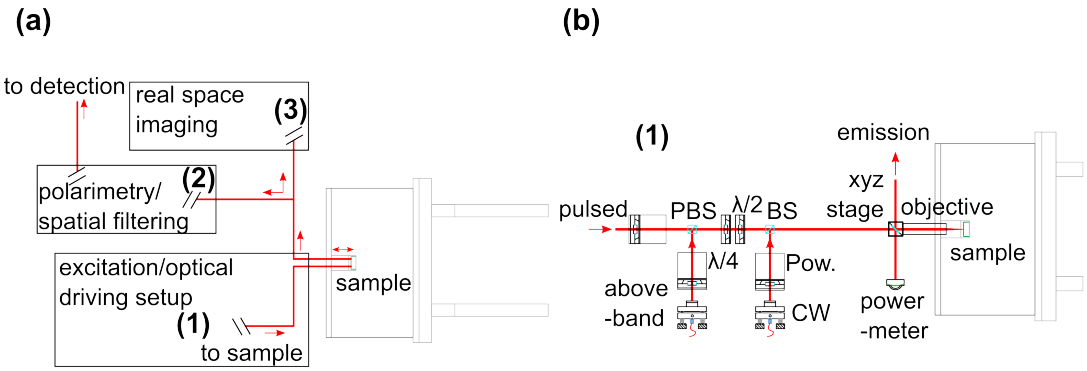

Figure 3.1: (a) Basic schematic of the optical setup in three sections: (1) consists of the input lasers fed into the periscope and objective which is then focused on the sample. (2) is the QD output section with polarimetry and filtering stray light. (3) Camera setup to observe sample surface. (b) Box (1) from (a) - Pulsed laser is a free space input, the above-band and CW are fiber coupled. Power controller optomechanics (Pow.) allows precise power control of each laser. Wave-plates allow varying the polarization of inputs. The xyz-stage is a triple periscope with a mounted objective to focus light onto a diffraction limited spot size on sample surface.

Figure 3.2(a) shows an image of the xyz-translation stage, known as a triple periscope, which allows coarse adjustment using the three knobs. The x-y knobs are to scan

across the sample within the chamber while the z-axis is used to focus the incident and reflected light. Each axis is fitted with piezo-actuators that allow additional fine adjustments of up to 40 μm over an applied voltage from 0-150 V. This is electrically controlled via a custom-built voltage controller which can be controlled either via LabView or from an electronic control box on the physical setup. The coarse adjustment knobs are most often used to quickly scan for target quantum dots. The piezo-controlled fine adjustment helps to optimize the collection from an individual quantum dot during experiments.

The triple periscope in figure 3.2(a) is used for excitation and collection with specific design to ensure complete control over incident laser light. Additionally, using two mirrored prisms aids translation while minimizing effects that may either warp or flip the polarization sent on to the sample. The confocal microscope setup can then be fully translated in the xyz-directions for excitation of individual QDs in the sample chamber.

Figure 3.2(b) shows the design for the sample holder used for experiments in the Voigt configuration. The magnetic field is applied through the central axis of the sample chamber and is fixed. An EQNL machined sample holder is attached to the cold finger for thermalization of the QD sample. The sample lies with the growth axis vertical allowing the magnetic field to be applied in-plane (Voigt), the mirrored prism is oriented at 45° to direct the excitation setup onto the sample. Collection is then redirected back through the prism and collected by the microscope. As mentioned previously, the sample used in this work contains a DBR layer below the InAs QD layer enhancing emisson, and so collection, in the vertical direction.

For the oblique configuration, alterations were required such that the magnetic field was applied at 60° from the sample growth axis. A schematic is shown in figure 3.2(c), of note for this setup that the total sample area available for the excitation was slightly reduced due to the oblique angle and limitations of the cryostats sample chamber. This did not affect the collection of particular QDs notably although it is important that when finding QDs in the Voigt configuration for investigating should be located near the center of the sample.

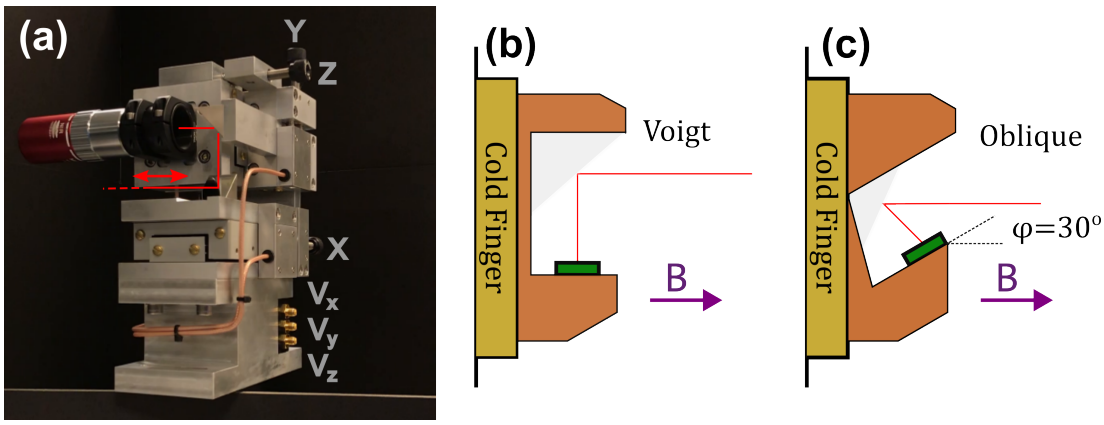

Figure 3.2: (a) The triple periscope or 3d translation stage, coarse tuning knobs (X,Y,Z) are used to scan the sample over a broad range with the X/Y controls moving across the sample, Z is the focusing axis. Piezo-actuators are connected (V_x, V_y, V_z) to allow fine tuning of up to 40 μm through application of a voltage between 0-150 V. (b) Incryo sample holder used for the Voigt configuration, with the magnetic field through the central axis of the sample chamber a mirrored prism allows the field to be in-plane with the QDs. (c) Oblique sample holder was machined to allow the QD sample to rest 30° angle below the central axis for oblique magnetic field configurations.

The detection path passes through box (2) in figure 3.1(a) which is the *polarimetry/spatial filtering setup*. This is where both the quarter-/half-wave plate polarimetry setups are located which have proven essential to enhance collection on the detectors. Box (2) in figure 3.1(a) thus contains optics to isolate single quantum dots and filter back-reflected laser light and neighboring QDs photo-luminescence spectra. Additionally, this allows a range of characterization methods for quantum dots via the polarimetry setups.

Finally, the *real space imaging* path in figure 3.1(a) is within box (3) which contains a CMOS camera setup with lenses, ranging f = 100 mm to f = 300 mm, and a 780 nm IR LED. This illuminates the sample surface to provide a real space image to allow navigation across the sample to find and re-find quantum dots. Quantum dots while often embedded under a host matrix contain special features on the surface. An aluminium mask covers portions of the self-assembled sample aiding with the relocation of target quantum dots due to distinct surface features. This results in methods to consistently relocate quantum dots that exhibit properties of particular interest.

(1) Excitation/Optical driving setup

A schematic of the components in box (1) is shown in figure 3.1(b), each of the laser inputs are combined onto the same path towards the sample. The pulsed input passes through free-space as an optical fiber will lead to pulse broadening in both the time and frequency spectrum through self-phase modulation. The above-band and continuous wave (CW) laser instead enter through a polarization maintaining fiber before the beam paths are combined using the non-/polarizing beam splitters. Each input contains a power block (Pow.) consisting of a fixed and mechanically rotated linear polarizer to control the input powers. Each power control block allows precise automated control of the beam intensities using custom-built Labview VI's.

Figure 3.3(a) displays the sinusoidal intensity curve of the above-band laser power, as a function of step number, related to the angle of the rotating analyzer. A custom-built Labview VI receives the input and will return calculated arrays of motor positions yielding intensity curves with linear, quadratic or logarithmic paths as shown in figure 3.3(b). Implementing such control into the experimental setup provides efficient data collection when performing various experiments on a quantum dot as different scalings benefit particular measurements. Quadratic power will provide a clearer scale for Rabi oscillations while log power is helpful for power-dependent saturation measurements [109].

The pulsed and above-band excitation pass a polarizing beamsplitter (PBS) and a quarter-wave plate (QWP) and half-wave plate (HWP) retarder. The CW laser also contains a set of retarders to control the polarization of the incident beam. Control over each beams polarization is essential for optimizing the effects on the QD spin-states and also assists in minimizing back-reflected laser light.

A 90:10 (T:R) beamsplitter reflects the input onto a triple periscope containing the microscope objective while the transmitted light passes onto a power-meter. The power-meter is calibrated to return the effective power that is reflected towards the QDs through the 90:10 beamsplitter. The triple periscope houses a 100x objective with a 12mm working distance (*Mitutoyo Plan APO NIR Infinity Corrected*) microscope objective (NA = 0.5). The objective focuses the light onto a diffraction-limited spot on the

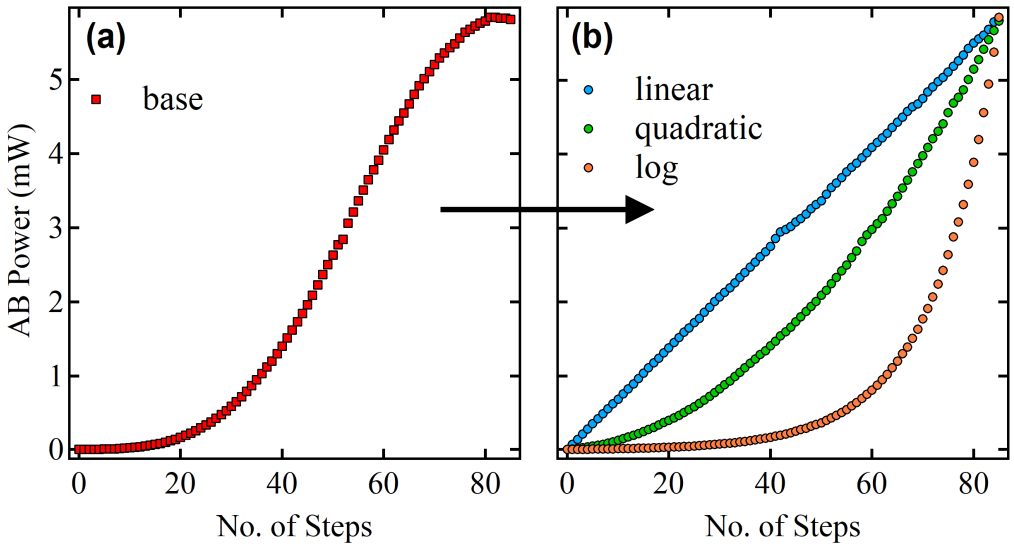

Figure 3.3: (a) Power dependence as a function of step number. The sinusoidal curve is processed in a Labview VI to return various intensity curves. (b) The returned above-band curve in (a) as a linear, quadratic or logarithmic curve. The number of steps remains constant in each.

sample surface to excite single to few quantum dots.

(2) Polarimetry/Spatial filtering

Figure 3.4 highlights the optical paths for the polarimetry/spatial filtering (2) and real space imaging (3). The polarimetry/spatial filtering path (2) travels westward in the figure while the real space imaging path (3) passes northward.

In the detection path, an achromatic focusing lens (f = 300 mm) lies at f from the objective. The focused output passes through a polarimetry setup (discussed shortly) before meeting a micrometer-sized pinhole at f. This spatial filtering aids in minimizing the back-reflected laser light and QD photo-luminescence from nearby QDs. This will continue to diverge after the pinhole until it reaches a distance of $2f$ where the collimating lens re-focuses the emission to send towards the detectors. Various neutral density (ND) filters lie in this path to control the intensity and help avoid saturating the detectors.

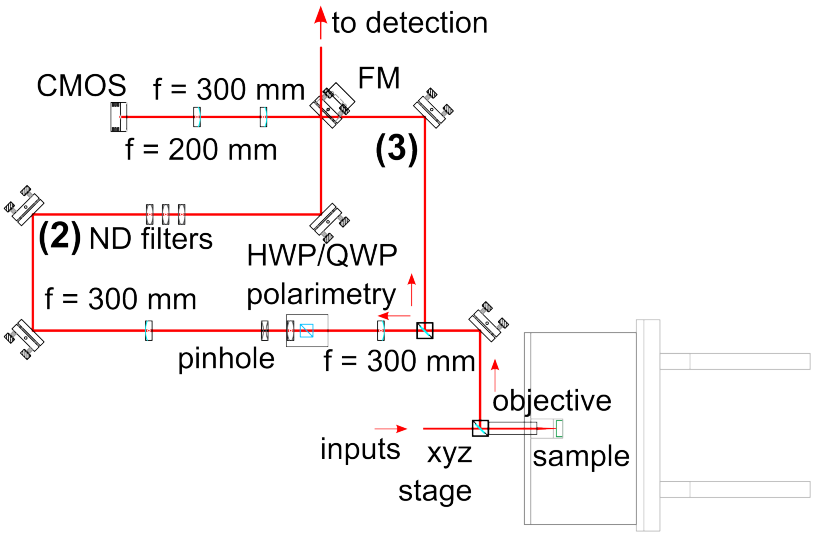

Figure 3.4: Box (2) from figure 3.1 (a) consists of two lens (f = 300 mm) with a pinhole at the foci to eliminate stray light from other QDs or laser light. The HWP/QWP polarimetry allows polarization resolved measurements and doubles to assist with cross-polarized reflectivity. ND filters allow intensity control to eliminate saturation effects on detectors. Box (3) consists of a CMOS cameras with two lens (f = 200/300 mm) which detects the sample surface using a white light to navigate across sample surface.

(3) Real space imaging

The illumination path (northward path) in figure 3.4 consists of an IR light (780 nm LED) that illuminates the sample surface. The reflected output is sent onto the CMOS camera through the main detection path in (2) either by activating a flip mirror or with a pellicle that can also be flipped in and out. Without the flip mirror in place, we see a non-inverted real space image which can be active while viewing spectra on the detectors. If the flip mirror is in place it passes through the $4f$ setup blocking light on the detectors and showing an image that is naturally inverted. During measurements this must be removed alongside the pellicle which will alter the polarization and intensity of emitted photons collected on the detectors.

3.2 Polarimetry setup

Observations of polarization-resolved photo-luminescence helps confirm various characteristics of quantum dots such as the selection rules under various configurations. Figure 3.4 contains the half-/quarter-wave plate (HWP/QWP) polarimetry setup that enables these measurements. The choice of HWP or QWP is dependent on whether the light from the sample exhibits highly linear or circular/elliptical polarization. A HWP is sufficient for the former while a QWP is required for the latter.

Choosing to experimentally implement wave-plate polarimetry requires working with the Mueller formalism that measures polarization states and optical elements using the observable intensities. The alternative approach is the Jones formalism, which instead expresses these states using orthogonal electric field components $E_x(z,t)$ and $E_y(z,t)$. This approach is natural when running simulations to evaluate selection rules because the dipole matrix elements are easily described with electric fields. Since only electric field amplitudes can be experimentally measured the Mueller formalism is more practical for data analysis.

In the Mueller formalism [111] the intensities are described using the Stokes vector defined as $\vec{S} = [S_0, S_1, S_2, S_3]$. The polarization states are given by four parameters relating to the overall intensity and degree of linear, diagonal and circular polarization [111], respectively.

The Stokes parameters shown can be found by applying a time average over the polarization ellipse as shown in [111]. This yields the following relation of the total intensity S_0 to the other parameters as [111]

$$S_0^2 = S_1^2 + S_2^2 + S_3^2. \tag{3.1}$$

Using this definition we are then able to generate the normalized Stokes vector using $|S_0| = \sqrt{S_1^2 + S_2^2 + S_3^2}$ which can be written as $|\vec{S}| = \vec{S}/|S_0|$. This normalization is useful in that it allows one to determine the degree of linear, diagonal and circular polarization from the values $S_{1,2,3} \in [-1, 1]$.

The Jones formalism [111–113] instead expresses the state using electric fields with the Jones vector,

$$\vec{J} = \begin{pmatrix} E_x(t) \\ E_y(t) \end{pmatrix} = \begin{pmatrix} E_{0x}e^{-i\varphi_x} \\ E_{0y}e^{-i\varphi_y} \end{pmatrix}. \tag{3.2}$$

The Jones vector in 3.2 contains information of both the amplitudes and phases of the electric field [111, 114]. The Stokes parameters can be related to the complex electric fields in the Jones vector through [115],

$$S_0 = E_x E_x^* + E_y E_y^* = E_{0x}^2 + E_{0y}^2, \tag{3.3}$$

$$S_1 = E_x E_x^* - E_y E_y^* = E_{0x}^2 - E_{0y}^2, \tag{3.4}$$

$$S_2 = E_x E_y^* + E_y E_x^* = 2\,\mathrm{Re}(E_{0x}E_{0y}), \tag{3.5}$$

$$S_3 = i(E_x E_y^* - E_y E_x^*) = 2\,\mathrm{Im}(E_{0x}E_{0y}). \tag{3.6}$$

The phase information of the electric fields are lost when evaluating the Stokes parameters but the intensities can be experimentally measured.

Both the HWP and QWP polarimeter setups implemented here rely on the same principle, the Stokes vector is measured as a function of a rotating retarder (half-/quarter-wave plate) and a fixed polarizing beamsplitter. We refer the reader to appendix A for the Mueller matrices of the generalized retarder, specific cases and polarizing elements.

Half-Wave Plate ($\lambda/2$) Polarimetry

Using a rotating $\lambda/2$ retarder and filtering the output with a polarizing beam splitter results in the HWP polarimetry setup. Emission from quantum dots can be described by the Stokes vector, S_{in}, and the output polarization after the polarimeter is evaluated using

$$\vec{S}'_{\text{hwp}} = M_{\text{pol}} \cdot M_{\text{hwp}}(\theta) \cdot \vec{S}_{\text{in}}. \tag{3.7}$$

The S'_0 component of $\vec{S}'_{\text{hwp}}$ contains the measurable intensity as a function of the half-wave retarder angle. By evaluating this component from 3.7 we find the intensity follows the function [111, 113, 116, 117],

$$I_{\text{hwp}}(\theta) = S_0 + (\cos^2(2\theta) - \sin^2(2\theta)) \cdot S_1 + 2\cos(2\theta)\sin(2\theta) \cdot S_2. \tag{3.8}$$

From 3.8 we see only the linear components, S_1 and S_2, are measurable indicating the HWP setup will not yield information regarding the circular S_3 component. Polarization's of a circular/elliptical nature require a quarter-wave setup described in the next section that also yields information regarding the S_3 component. Although this is the case, the HWP setup is simple to implement and aids when determining level structures and evaluating in-plane g-factors of QDs. Since QDs under a Voigt configuration are known to exhibit a linearly polarized double-Λ system this setup is sufficient. There have been numerous previous works [118–120] that have benefited from the simpler implementation of HWP polarimetry.

Quarter-wave plate ($\lambda/4$) polarimetry

Replacing the half-wave plate with a quarter-wave ($\lambda/2 \rightarrow \lambda/4$) will yield the ability to determine polarization states with either a circular or elliptical polarization. Taking an arbitrary input, S_{in}, the output polarization can be evaluated with the QWP setup using,

$$\vec{S}'_{\text{qwp}} = M_{\text{pol}} \cdot M_{\text{qwp}}(\theta) \cdot \vec{S}_{\text{in}}. \tag{3.9}$$

Similar to the half-wave case the output intensity S'_0 is determined by taking the first element of the vector, $\vec{S}'_{\text{qwp}}$. The resultant expression can be simplified using

trigonometric formulas to yield the following expression [116],

$$I_{\mathrm{qwp}}(\theta) = A + B\sin 2\theta + C\cos 4\theta + D\sin 4\theta, \tag{3.10}$$

which is a Fourier series with four Fourier coefficients A-D that are evaluated from the data. Each of the Fourier coefficients can be evaluated by transition from the continuous to the discrete case which is highlighted alongside the complete Mueller matrices of the components used in appendix A. From this each coefficient can be related to the Stokes parameters of 3.9 by [117],

$$\begin{aligned} A &= S_0 + S_1/2, & B &= S_3, \\ C &= S_1/2, & D &= S_2/2. \end{aligned} \tag{3.11}$$

Moving from the continuous to the discrete case yields four expressions as a function of step angle of the quarter-wave retarder as in [121]. From this we can determine the Stokes parameters and so evaluate the polarization state of a quantum dots transitions.

The single fixed polarizer and rotating (HWP/QWP) analyzer here is but one of various possible configurations. The HWP polarimetry was chosen based upon those used in the previous works mentioned. The QWP implementation was a required adaption based upon the necessity to evaluate circular/elliptical polarizations. One can find various different polarimetry setups in [113] that may be more appropriate for an interested readers purposes.

Implementing the QWP setup experimentally proved challenging for various reasons that we attempt to address here. The semiconductor quantum dots used in this work show an in-homogeneity in both wavelength, intensity and splitting under an applied magnetic field. Coupling this with the high density of quantum dots leads to difficulty eliminating excess light from neighboring dots while back-reflected light and general background counts from other sources contribute negatively. As

the Stokes parameters are highly dependent upon the measurable intensities, unexpected sources of light will contribute to the experimental error. During analysis the Lorentzian emission lines of dot transitions were fitted using Lorentzian fits to help determine the total intensity. This also allowed evaluation of a background count offset to further help reduce this error.

Finally, retarders themselves can never be ideal and so minute variations in the phase retardation value δ naturally occur across the surface of the QWP. Careful alignment by attempting to strike the wave-plate directly at the center such that when rotated the beam remains on a constant area was performed. Further, efforts to evaluate the variation in δ were conducted by taking measurements of known polarization's through the polarimeter. This resulted in a Mueller matrix of the combined optical elements of the polarimeter and was motivated by [112].

Cross-polarized reflectivity

A final, yet important, application for the polarization optics described in this section are to aid in minimizing back-reflected laser light via cross-polarized reflectivity. This isolation technique extinguishes excess laser light by setting the optics to allow only polarized light orthogonal to the laser input onto the detectors.

Experiments resonantly addressing transitions of a quantum dot with a CW laser involve high intensity lasers that are adjacent to transitions observed on the detectors. This back-scattered laser light can easily saturate and possibly cause permanent damage to the detectors which is why this technique is so important. Under oblique magnetic field configurations it becomes difficult to ensure light is fully orthogonal. Here a balance between stray light levels and optimizing detection is then sought after.

3.3 Techniques for pulse control

When pulsed excitation is correctly applied to a quantum dot it can generate spin rotations in the electron spins state space. The preface to do so optically is a pulsed input with a broadband larger than the level splitting of the spin [122], though further

steps are required to experimentally implement the process.

First, we introduce a spectral filter that allows one to narrow down a subset of the laser pulses broadband spectra. This helps tailor the pulse spectra to minimize back-reflected laser light and assists during both resonant and non-resonant excitation schemes. Secondly, a method to produce time-delayed pulses is necessary to gain control over multiple orthogonal axes of the spin-qubit state space. With a delay stage we show an input pulse can be split and delayed yielding two pulses time-separated by up to 4.8 ns.

Tailoring pulse spectra by spectrally filtering

Recall that ultra-fast pulses of light must adhere to the time bandwidth product described in section 2.2. This narrowing in the time domain yields a broad spread in the spectral domain pictured in figure 3.5(a). This broad spread of the frequency spectra can yield interactions with neighboring quantum dots or lie spectrally close to detection of transitions. The spectral filter helps resolve this by returning only a subset of the entire pulse spectra. This is a method of reducing the pulse spectra overlapping a dots photo-luminescence as shown in figure 3.5(b).

For a 2.5 ps pulse with a center $\lambda_c = 912$ nm, approximate values applied to the InGaAs quantum dot sample, the pulse bandwidth is $\sim$0.3 nm. By spectrally filtering this output as in figure 3.5(b) we can prevent overlap with dot emission from detected transitions.

The experimental setup is depicted in figure 3.5(c) where an ultra-fast pulse enters from the bottom. The telescope expands the beam profile prior to dispersing on the diffraction grating. The dispersed light meets a focusing lens and a mirror with a slit at f from the lens. Filtering the output is a function of the slit width and grating angle, so one can selectively filter the output that is returned along the same beam path. This filtered output is then re-collimated and sent towards the rest of the experimental setup.

The wavelength spectra of a pulse (λ_c = 911.42 nm, τ = 3.3 ps) is shown in figure 3.6(a), the green curve shows the broadband spectra explained above prior to the

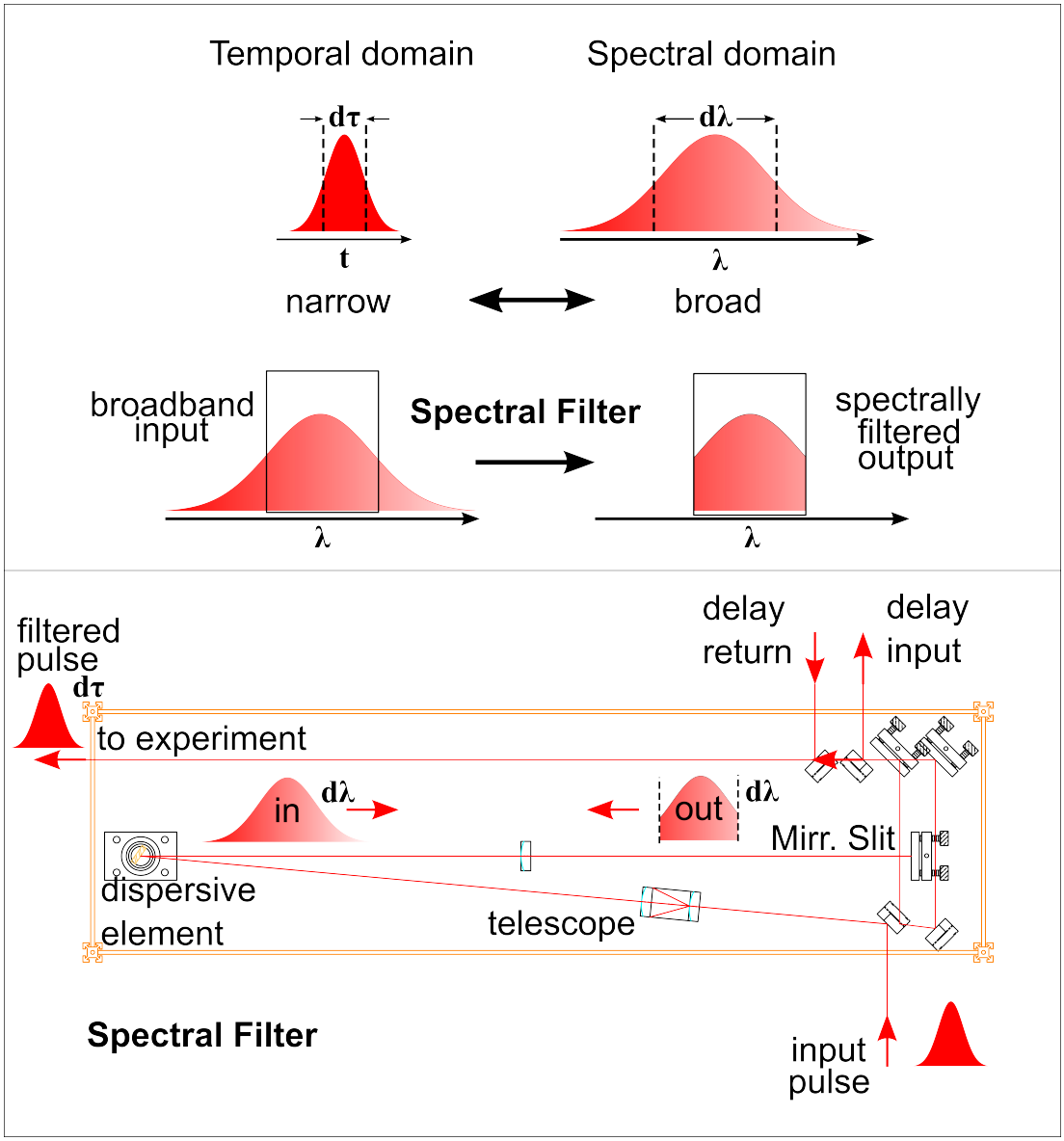

Figure 3.5: (a) A pulse narrow in the temporal domain will be broad in the spectral domain and vice versa. (b) The aim of a spectral filter is to take a broadband spectral input and return a filtered subset as shown. (c) Schematic design of the spectral filter, an input pulse enters from below, passes through a telescope onto a dispersive grating. The lens and mirrored slit at f will allow one to chop the dispersed spectra and reflect only what passes through the slits. The filtered output can be sent on to the rest of the setup.

spectral filter. The red curve is the resultant spectra after activating the spectral filter from figure 3.5(c). By narrowing the pulse spectra with this process, the resonant/non-

resonant pulses can be brought close enough to address individual quantum dot transitions while minimizing back-reflected light. This is essential for data acquisition as rotations using the pulsed laser often involve powers 10-100's mW which is orders of magnitude greater than the detected photon emission from the quantum dot.

The output can then either pass through a delay stage, discussed next, or travel towards the excitation path in figure 3.1. The filter is not an essential requirement for every experiment and as such the setup consists of a series of flip mirrors allowing different combinations of the spectral filter and delay stage. This allows different configurations such as both active, one or the other active, or neither.

Pulse delay

Complete coherent control involves accessing arbitrary locations on the Bloch sphere. The two main axes are the polar and the azimuths angle (θ, ϕ) and through these rotations can reach arbitrary locations in the space. The radial component of the Bloch vector will naturally decrease as decoherence occurs in the system and reducing this rate of decoherence requires additional techniques (see spin echo [71]).

The experimental polar axis is accessed as a function of the laser pulse power. This is synonymous with the pulse area descriptions seen in experiments using atomic systems [123] where modulation of CW laser excitation is used instead. As the mode-locked laser produces a fixed pulse we instead vary the power of each individual pulse.

The azimuthal axis rotates at a rate inherent to charged particles under a magnetic field. Spins in quantum dots will precess as they rotate around the applied magnetic field. By introducing a time-delay between pulses we create a dead time in which the system evolves at the rate determined by the Larmor frequency.

The delay stage schematic is shown in figure 3.7, individual pulses are split using an unbalanced Mach-Zehnder configuration to generate time-delayed pulses with variable delay. The two arms, named the fixed and delay arm, are aligned to match the power and beam profiles of each pulse. These are formed from a single pulse split across each arm as displayed in figure 3.6(b).

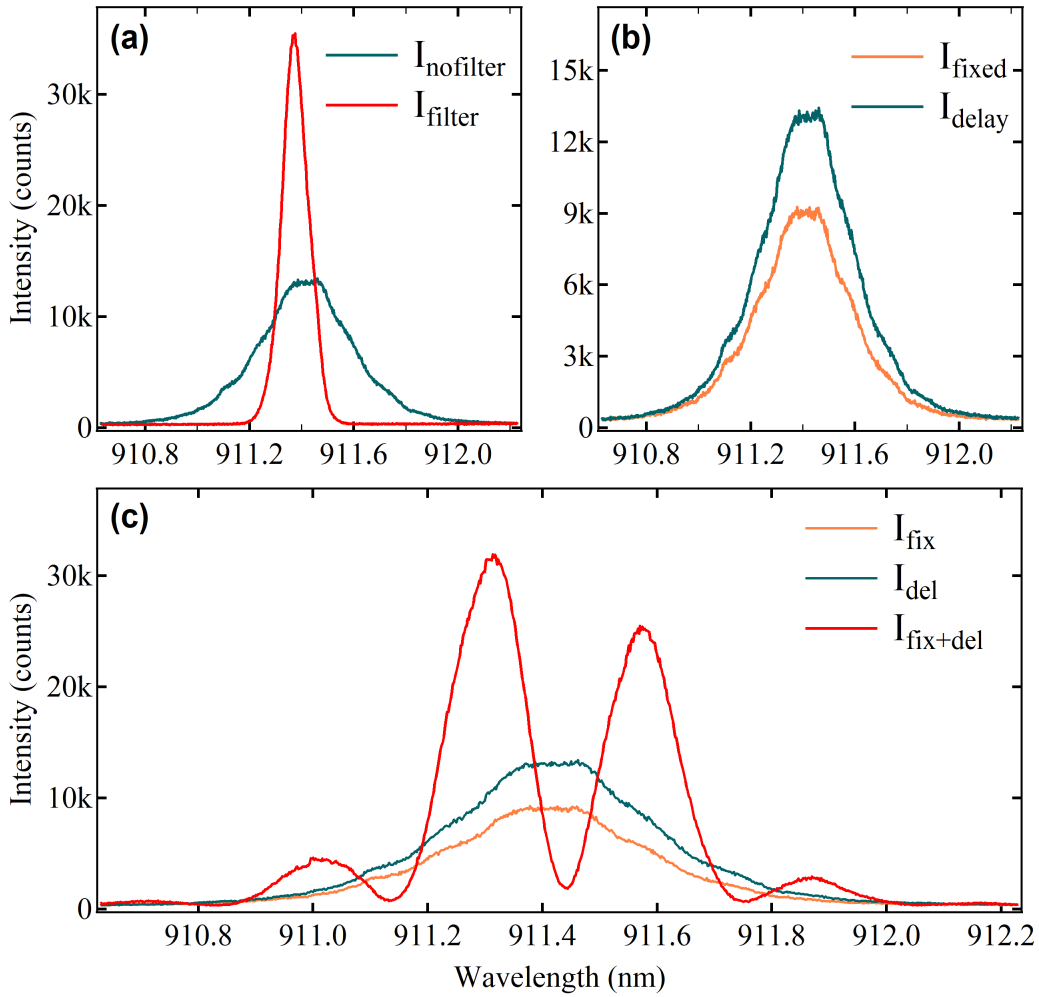

Figure 3.6: (a) Spectra of mode-locked laser pulsing at $\lambda_c = 911.42$ nm. $I_{nofilter}$ exhibits the pulse without alteration while I_{filter} is with the spectral filter active. (b) Pulse through each arm with power P = 100 nW of fixed and delay arms individually. (c) $I_{fixed+delay}$ shows interference fringes present at zero delay when both arms are simultaneously active.

By introducing a variable path length the pulses can then be separated by $\Delta\tau = \Delta L/c$. A retro-reflector mounted onto a mechanical translation stage lies on the delay arm and the lab configuration yields 20 μm/step over 72k steps for a total of 4.8 ns of total delay between the pulses.

In figure 3.6(c) we see the result of both arms being active while $\Delta\tau$ lies close to zero delay, the combined pulse $I_{fixed+delay}$ shows interference resulting from the large

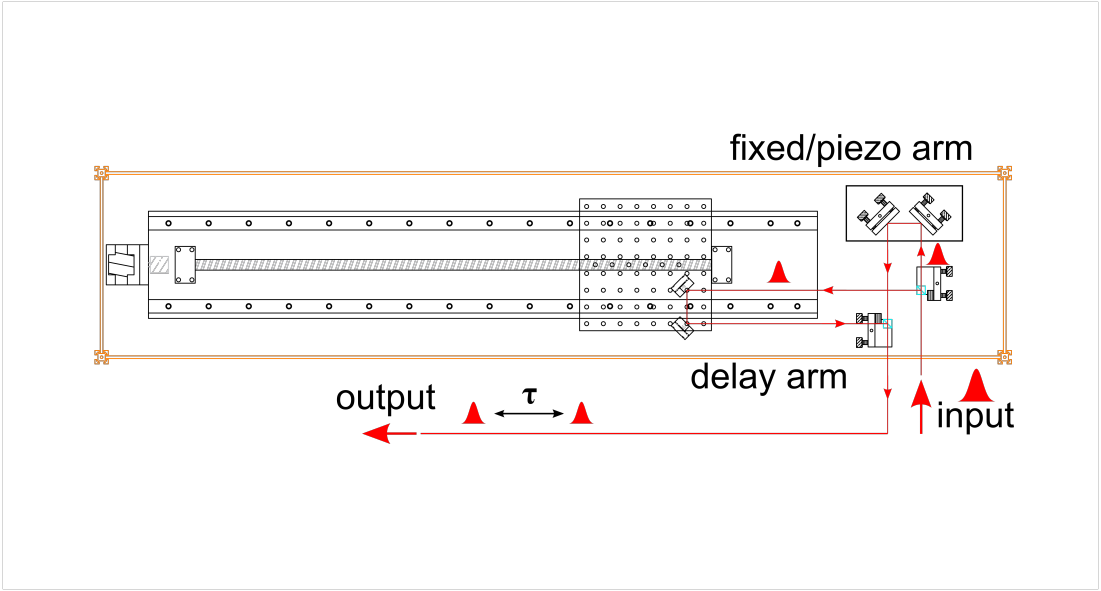

Figure 3.7: Schematic design of the delay stage. The pulsed input is separated through the fixed and delay arm. The delay arm lies on a motorized translation stage with 72k steps at 20μm/step. The fixed/piezo arm may also be varied with an applied voltage at sub-micron scales. Both outputs are recombined and sent onto the rest of the setup.

coherence between the pulses. Data collected using the delay stage close to zero delay must be interpreted cautiously as a result of this interference effect. Stepper motors control the translation stage using a custom electronic control unit operated through a custom-built Labview VI for precise and automated measurements.

Off-resonant pulse experiments find the delay arm is sufficient to resolve the spin rotations along the azimuthal axis. For a resonant experiment the system will evolve at the optical frequency of the pulse [124] in THz frequencies. The fixed arm in figure 3.7 also has optics mounted on a small translation stage operated using a piezo-stack. An applied voltage yields finer sub-micron displacements allowing one to observe these oscillations in the resonant case which are on the order of femtoseconds.

3.4 Conclusion

This section described some additions to the experiment that specifically tailor the optical setup towards coherent control of quantum dot spins. The combination of the op-

tical driving setup, polarimetry and spatial filtering and the real space imaging paths yields a high degree of control. It also allows predictable navigation and relocation of QDs throughout the sample used in this work.

The confocal microscopy setup consisting of the objective fixed to the triple periscope has proven essential to isolate individual quantum dots. The narrowly focused spot sizes excite only a few quantum dots as opposed to a broader ensemble. Filtering techniques, both spatial and via polarizations, allow enhanced detection and further improve characterization of quantum dots using polarization-resolved photoluminescence.

Polarimetry methods introduced in this section will be used to characterize the level structures and selection rules under a range of different magnetic field configurations. The choice of HWP or QWP polarimetry is dependent upon the configuration but both combined help fully evaluate g-factors and the Stokes vector of individual transition lines.

Finally, we gave a brief description of custom-build equipment that tailors ultrafast pulses from a mode-locked Ti:Sapphire. Spectral filtering improves experimental procedures while the delay stage highlights how an unbalanced Mach-Zehnder configuration can be adapted for use in advanced control experiments.

For the rest of this work, we describe how this experimental setup has coalesced to produce a wide variety of results, including characterization and realization of single-qubits using spins confined to quantum dots.

Chapter 4

Calibrating the Setup - Demonstrating Complete Coherent Control

In this section we show techniques used to investigate, manipulate and control spin-states confined within semiconductor QDs. By demonstrating coherent control under a Voigt configuration we verify the experimental setup has an advanced baseline ability from which further research can begin. With this in mind, we introduce the necessary theoretical background before moving through a series of experiments that equate to what we call *calibrating the setup*.

This chapter is laid out as follows: section 4.1 begins by describing how magnetic fields affect the level structure of a charged quantum dot and we show the resultant selection rules for the two most common configurations. Section 4.2 then describes the theory that underpins ultra-fast coherent control techniques used throughout this work in detail. Finally, section 4.3 then applies this understanding by showing a series of experiments where the ground-state spin of the electron is harnessed, demonstrating full control over SU(2) rotations.

Solid-state systems like quantum dots have numerous ways to define two-state quantum systems that may used as a physical qubit. Two-level systems are by no means difficult to find in quantum systems yet the appeal of spin-qubits from charges

confined to quantum dots is the degree of control over system properties through application of electric and magnetic fields. Additionally, the ultra-fast coherent control technique [125] used in this work allows the coherence of the spin-qubit to be limited by the ground-state spin-relaxation rates and coherence times. As highlighted in chapter 1, these have been shown to be many orders of magnitude greater than the short-lived trion state decay processes [70, 126–132].

The electron can be used either as a spin-qubit or a charge-qubit [72, 133] dependent on whether the qubit is defined by the spin properties of the electron (former) or existence/absence of an electron (latter). While numerous systems are possible, the focus of this work is on negative singly-charged quantum dots that after recombination leave a single electron in the ground state forming the spin-qubit state space.

A singly-charged quantum dot contains a three-particle system consisting of two electrons and a hole if negatively charged or the opposite configuration to be positively-charged. For it to be a neutral quantum dot a two-particle system consisting of only an electron and hole pair would be present. Each of these systems contain some similarities and differences [134] but charged quantum dots are the focus due to well documented applications towards coherent control [34, 64, 124, 135, 136].

The hole states are known for having different bands related to the spin projection $\hat{J}_h = 3/2$ which contain the heavy-hole, light-hole and split-off sub-bands [137–140]. Describing these angular momentum states in the form $\left|\hat{J}, \hat{S}_z\right\rangle$ the heavy-hole state is written $|3/2, \pm 3/2\rangle_{hh}$ while the light-hole and split-off states are denoted by $|3/2, \pm 1/2\rangle_{lh}$ and $|1/2, \pm 1/2\rangle_{so}$. The light-hole and split-off states can often be neglected in self-assembled quantum dots due to the strong confinement in the z-direction, causing them to be energetically separated. Henceforth, we thus neglect these states to simplify the system and focus only on the heavy-hole states.

On this assumption the hole state can be viewed as having a pseudo-spin character of $\hat{S}_z = 1/2$. This simplification allows for the evaluation of the hole Hamiltonian to be synonymous with the electron Hamiltonian with a differing pre-factor and sign. The following section now aims to describe the effect a magnetic field has on both the ground state electron spins $\{|\downarrow\rangle, |\uparrow\rangle\}$ and the heavy-hole states $\{|\Downarrow\rangle, |\Uparrow\rangle\}$.

4.1 Singly-charged quantum dots under an external magnetic field

Applying an external magnetic field to either an electron or hole state will result in the magnetic field lifting the degeneracy of the states. To describe the effects of a magnetic field $\mathbf{B} = (B_x, B_y, B_z)$ on the internal electronic spin-states we use the Zeeman Hamiltonian,

$$\mathcal{H}_{zeeman} = \frac{1}{2}\mu_B \sum_{\alpha \in x,y,z} g^{\alpha}_{e/h} \cdot B_\alpha \, \hat{S}_\alpha, \tag{4.1}$$

where μ_B is the Bohr magneton, $\hat{S}_\alpha$ are the Pauli spin operators and $g^{\alpha}_{e/h}$ is the electron/hole g-factors along the principal axes of the quantum dot. The magnetic field can consist of an externally applied field but also may have a component caused by dynamically polarized nuclear spins inside the quantum dot known as the Overhauser effect [40]. The magnetic field direction, field strength and sample properties can all define whether this effect is significant enough to be considered.

Taking the z-axis to be oriented along the growth and optical axis of the self-assembled sample, as in figure 4.1 we can define the common magnetic field geometries for these quantum dots. A magnetic field aligned parallel to the growth axis $\vec{B} = B_z$ is considered to be under a Faraday configuration. Alternatively, an in-plane magnetic field in the x-y plane that is perpendicular to the growth axis $\vec{B} = B_x$ is in a Voigt configuration.

Investigating the resultant states in a Faraday configuration shows that the electron and hole states (which differ only by a sign) are eigenstates of the Hamiltonian written as,

$$\mathcal{H}^z_{zeeman} = \frac{1}{2}\mu_B \, g^z_{e/h} \cdot B_z \, \hat{S}_z, \tag{4.2}$$

$$\mathcal{H}^z_{zeeman} = \frac{1}{2}\mu_B \, g^z_{e/h} \cdot B_z \begin{pmatrix} 1 & 0 \\ 0 & -1 \end{pmatrix}. \tag{4.3}$$

From this we see the applied field is aligned with the quantization axis and simply lifts the degeneracy of the states under application of a magnetic field splitting the states by energy $E^z_{\pm} = \pm\mu_B g^z_{e/h} B_z/2$.

Evaluating the selection rules using the transition dipole matrix elements reveals the Faraday geometry consists of two optically active transitions emitting circularly polarized light $\hat{\sigma}_{\pm}$. The lack of any mixing between these states explains the distinct two-level structure observed in figure 4.1(b) which proves to be insufficient for coherent control experiments between the electronic ground states. This is due to the lack of an available cross-transition that yields a method of coupling the ground states.

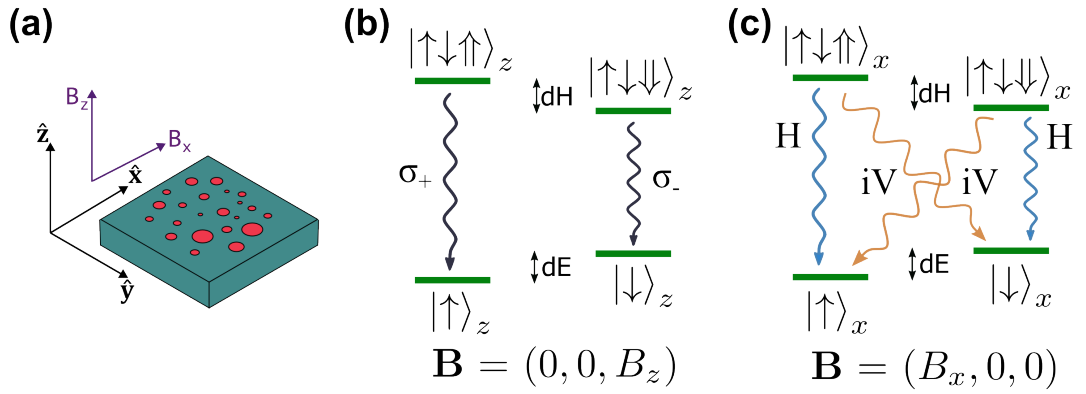

Figure 4.1: (a) Axes of self-assembled sample and applied magnetic field. $\hat{z}$ is taken to be the growth and optical axis of the sample, $\hat{x}$ is in-plane of the QD layer resulting mixing basis states aligned along z. (b) Level structure under a Faraday configuration (B_z) showing two optically active transitions emitting circularly polarized light, $\sigma_{\pm}$, with angular momentum l = 1. (c) Voigt configuration level structure showing the coupled double-λ structure useful for generating rotations between electronic ground states. Linearly polarized emission of transitions can be understood as a superposition of the z-aligned basis states.

To generate coherent rotations between these states we require an axis of rotation

introduced by a Voigt configured magnetic field which will generate a double-Λ system as seen if figure 4.1(c). With an in-plane magnetic field parallel to the x-axis the resultant Zeeman Hamiltonian is,

$$\mathcal{H}^{x}_{zeeman} = \frac{1}{2}\mu_B \; g^{x}_{e/h} \cdot B_x \; \hat{S}_x, \tag{4.4}$$

$$\mathcal{H}^{x}_{zeeman} = \frac{1}{2}\mu_B \; g^{x}_{e/h} \cdot B_x \begin{pmatrix} 0 & 1 \\ 1 & 0 \end{pmatrix}, \tag{4.5}$$

which reveals the energies $E^{x}_{\pm} = \pm\mu_B g^{x}_{e/h} B_x/2$ relating to the new eigenstates. Diagonalizing 4.5 yields the Voigt-configured states,

$$|\uparrow\rangle_x = \frac{1}{\sqrt{2}}(|+1/2\rangle_z + |-1/2\rangle_z), \tag{4.6}$$

$$|\downarrow\rangle_x = \frac{1}{\sqrt{2}}(|+1/2\rangle_z - |-1/2\rangle_z), \tag{4.7}$$

$$|\uparrow\downarrow\Uparrow\rangle_x = \frac{1}{\sqrt{2}}(|+3/2\rangle_z + |-3/2\rangle_z), \tag{4.8}$$

$$|\uparrow\downarrow\Downarrow\rangle_x = \frac{1}{\sqrt{2}}(|+3/2\rangle_z - |-3/2\rangle_z). \tag{4.9}$$

The electronic ground-states consist of symmetric and anti-symmetric combinations of the basis states aligned along the z-axis and similarly, the heavy-hole trion states are also an anti-/symmetric linear combination of the basis states. As mentioned before the light-hole and split-off bands are neglected in this evaluation as they are often separated by tens of meV [141]. This is often a safe assumption and there exist various techniques to check for valence-band mixing through observation of emission in a Faraday configuration [37, 142, 143].

Singly-charged negative quantum dots consist of a trion state containing a singlet electron pair and a hole state, after recombination of the hole spin with a paired electron either a spin up or down electron will reside in the ground state. We can evaluate the selection rules of the transitions from this process as follows: in the Faraday configuration each trion state $\{|\uparrow\downarrow\Uparrow\rangle_z, |\uparrow\downarrow\Downarrow\rangle_z\}$ will recombine with the paired electron

leaving the system in the remaining spin state emitting $\hat{\sigma}_{\pm}$ light with a unit of angular momentum which can be written as,

$$|\uparrow\downarrow\Uparrow\rangle_z \rightarrow \hat{\sigma}_+ \otimes |\uparrow\rangle_z \,, \tag{4.10}$$

$$|\uparrow\downarrow\Downarrow\rangle_z \rightarrow \hat{\sigma}_- \otimes |\downarrow\rangle_z \,. \tag{4.11}$$

The two remaining combinations under a Faraday configuration contain two units of angular momentum and so are the optically-inactive forbidden transitions sometimes referred to as dark states.

Under the Voigt configuration $\{|\uparrow\downarrow\Uparrow\rangle_x \,, |\uparrow\downarrow\Downarrow\rangle_x\}$ the linear combinations of 4.6 -4.9 result in the following calculation,

$$\begin{aligned}
|\uparrow\downarrow\Uparrow\rangle_x &\rightarrow |\uparrow\rangle_x \\
&= {}_x\langle\uparrow| \, \hat{\epsilon}\cdot\hat{p} \, |\uparrow\downarrow\Uparrow\rangle_x \\
&= \frac{1}{2}({}_z\langle\uparrow| + {}_z\langle\downarrow|)\hat{\epsilon}\cdot\hat{p}\,(\hat{\sigma}_+ \otimes |\uparrow\rangle_z + \hat{\sigma}_- \otimes |\downarrow\rangle_z) \\
&= \frac{1}{2}(\hat{\sigma}_+ \otimes |\uparrow\rangle_z + \hat{\sigma}_- \otimes |\downarrow\rangle_z) \\
&= \frac{1}{2\sqrt{2}}((\hat{x} - i\hat{y}) \otimes |\uparrow\rangle_z + (\hat{x} + i\hat{y}) \otimes |\downarrow\rangle_z) \\
|\uparrow\downarrow\Uparrow\rangle_x &\Rightarrow \frac{1}{\sqrt{2}}\hat{x} \otimes |\uparrow\rangle_x \,.
\end{aligned} \tag{4.12}$$

The transition from the trion to the ground state, $|\uparrow\downarrow\Uparrow\rangle_x \rightarrow |\uparrow\rangle_x$, is evaluated using the dipole operator $\hat{\epsilon}\cdot\hat{p}$ as seen in the intermediate steps of equation 4.12 . The recombination of the resident hole with the paired electron leads to the emission of a circularly polarized photon. The resultant state then shows that linearly polarized emission is expected after recombination.

A similar calculation for the remaining three transitions yields,

$$|\uparrow\downarrow\Uparrow\rangle_x \rightarrow |\downarrow\rangle_x$$
$$\Rightarrow \frac{1}{\sqrt{2}} i\hat{y} \otimes |\downarrow\rangle_x \,, \tag{4.13}$$
$$|\uparrow\downarrow\Downarrow\rangle_x \rightarrow |\uparrow\rangle_x$$
$$\Rightarrow \frac{1}{\sqrt{2}} i\hat{y} \otimes |\uparrow\rangle_x \,, \tag{4.14}$$
$$|\uparrow\downarrow\Downarrow\rangle_x \rightarrow |\downarrow\rangle_x$$
$$\Rightarrow \frac{1}{\sqrt{2}} \hat{x} \otimes |\downarrow\rangle_x \,. \tag{4.15}$$

From this we see that mixing the states with an in-plane magnetic field the quantum dot results in a double-Λ system. The Λ-system allows for stimulated Raman adiabatic passage (STIRAP) resulting in methods to generate coherent rotations around the ground-state electron spins.

Since STIRAP which is conducted here using a single far-detuned pulse allows for adiabatic elimination of the excited state, concerns regarding short decay times of these states can be neglected. This naturally leads to longer coherence times and when coupled with speed of operations that can be performed using ultra-fast ps-scale pulses highlights the systems attractive properties.

Figure 4.2(a)-(d) show HWP polarimetry of four randomly selected quantum dots under a $B_0 = 5$ T magnetic field. HWP polarimetry is appropriate for Voigt configuration magnetic fields due to the linear polarization we expect and has been a common measurement technique for research under this configuration [108, 119, 120, 135]. Each profile clearly highlights the distinct linearly-polarized inner and outer transitions defined in 4.12 - 4.15 .

From each of the quantum dots selected we see the in-homogeneity of the g-factors that leads to considerable variations in the spectral profile and also that intensities vary significantly from dot to dot. As a result a pre-selection procedure for a suitable quantum dot is conducted prior to experiments. A preferred choice to perform optical experiments would be the dot in 4.2(a) as the cross-polarized transitions (outer vs in-

ner) are spectrally separated enough that back-reflected laser light could be effectively minimized. This enhances the quality of acquired data when performing coherent control experiments.

Figure 4.1(a)-(c) shows the orientation with respect to the quantum dot plane and the associated level structures present under the Faraday (b) and Voigt (c) configurations, respectively. For the remainder of this chapter we will focus on the Voigt configuration visible in figure 4.1(c). Here, we present coherent control experiments of the ground-state spins under this configuration.

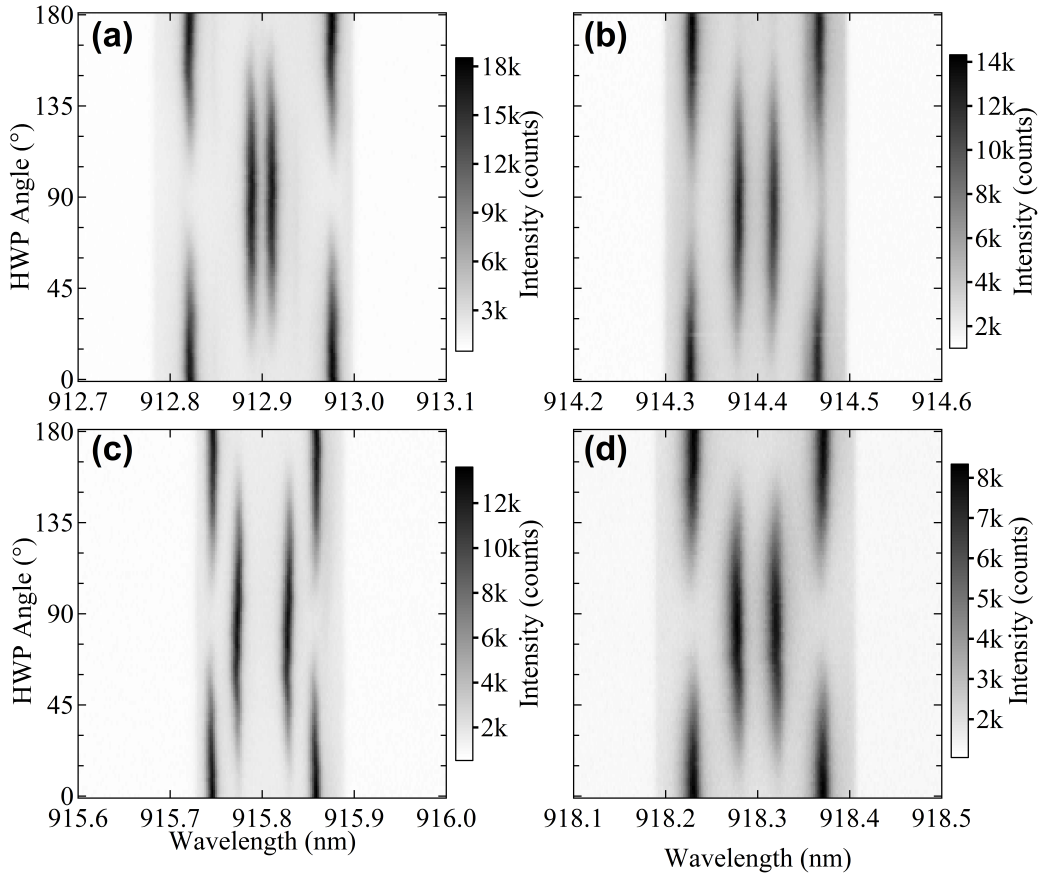

Figure 4.2: (a)-(d) Energy vs HWP angle for arbitrary QDs under Voigt configuration with B_x = 5 T. Orthogonal linearly polarized transitions as shown in (4.1c) can be seen. The variance in electron and hole factors, $g^x_{e/h}$, for each QD leads to various energy separation. The most notable differences can be seen in (a) and (c).

4.2 Coherent control of electronic ground-state spins

Coherent manipulation of the ground states of a quantum dot are of particular interest for quantum information processing with predictions of electron spin lifetimes greater than 1 s [70] and relaxation rates for hole spins in the μs-ms regimes [126, 144].

Extending coherence times are essential for improving capabilities of matter-qubits across many domains. The additional interest of using the ground-state spins is the ratio of the number of possible operations with respect to the coherence times of the spins yielding a high ratio of operations within the lifetime [71, 135].

Either electron or hole spins are available resulting from the growth process and choice of a n-/p-type dopant to charge the quantum dots. Deterministic charging of quantum dots can also be done routinely through application of a voltage bias. Ground state electron or hole spins can be used as a spin-qubit with each showing particular strengths. For example, hole spins benefit from a reduced interaction with the surrounding nuclei by interacting only through higher order dipole interactions [73].

This section details the theoretical methods that allow one to understand ultra-fast coherent control using far-detuned optical ps-pulses. Figure 4.3 depicts a generalized 3-level system consisting of two ground states $\{|g_1\rangle, |g_2\rangle\}$ coupled through an excited state $\{|e\rangle\}$ in a Λ-configuration [145]. The bare energy levels are $\hbar\omega_{e1}, \hbar\omega_{e2}$ and the transitions are addressed through a single optical-pulse with a bandwidth larger than the ground-state splitting ($\delta_g = \Delta_1 - \Delta_2$) [122]. The central optical frequency of the pulse is ν and the Rabi frequencies are $\{\Omega_1, \Omega_2\}$ while the detunings are $\Delta_\alpha = \nu - \omega_{e\alpha}$.

The Rabi frequencies are defined from the electric field (E_0) interaction with the dipole operator ($\hat{\mu}$) and is written as,

$$\Omega_\alpha = 2 \langle g_\alpha | \hat{\epsilon} \cdot \hat{\mu} | e \rangle E_0/\hbar. \tag{4.16}$$

The off-diagonal matrix elements are non-zero due to the parity operation between the ground and excited states. Since optical frequencies lie in the THz regime, we can

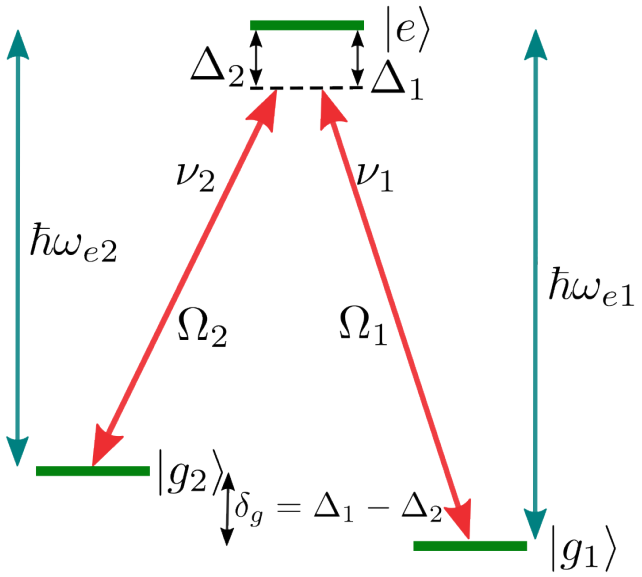

Figure 4.3: A generalized 3-level Λ-system with level splittings $\hbar\omega_{e1/2}$ (blue arrows) and an electric field (red arrows) detuned from the excited state $|e\rangle$ with Rabi frequencies $\Omega_{1/2}$, central frequency ν and ground state splitting δ_g.

ignore fast oscillating terms in the Hamiltonian via the rotating-wave approximation (RWA) and shift to a rotating frame while setting the energy of $|g_1\rangle$ to be zero.

We can then write the Hamiltonian consisting of the bare Hamiltonian $\hat{\mathcal{H}}_0$ which describes the level structure, and the interaction Hamiltonian $\hat{\mathcal{H}}_1$ for the three-level system interacting with the laser as,

$$\begin{aligned}\hat{\mathcal{H}} = &-\Delta_1 |e\rangle\langle e| + \delta_g |g_2\rangle\langle g_2| \,(\hat{\mathcal{H}}_0) \\ &- \frac{1}{2}\left(\Omega_1 |e\rangle\langle g_1| + \Omega_2 |e\rangle\langle g_2| + \Omega_1^* |g_1\rangle\langle e| + \Omega_2^* |g_2\rangle\langle e|\right)(\hat{\mathcal{H}}_1).\end{aligned} \tag{4.17}$$

Introducing the quantum state for the system as $|\psi\rangle = c_1(t)\,|g_1\rangle + c_2(t)\,|g_2\rangle + c_e(t)\,|e\rangle$ we can then solve the Schrodinger equation,

$$i\hbar\partial t\,|\psi\rangle = \hat{\mathcal{H}}\,|\psi\rangle\,. \tag{4.18}$$

By operating on the left with $\{\langle g_1|\,,\langle g_2|\,,\langle e|\}$ we find the system of coupled differential equations to be,

$$i\hbar\dot{c_1}(t) = -\frac{\Omega_1^*}{2}c_e, \tag{4.19}$$

$$i\hbar\dot{c_2}(t) = \delta_g c_2 - \frac{\Omega_2^*}{2}c_e, \tag{4.20}$$

$$i\hbar\dot{c_e}(t) = -\Delta_1 c_e - \frac{1}{2}(\Omega_1^* c_1 + \Omega_2^* c_2). \tag{4.21}$$

Equations 4.19-4.21 can be evaluated for a far red-detuned pulse where $\Delta_1 \sim \Delta_2 = \Delta$. If the detuning $\Delta \gg \Omega_1, \Omega_2, \delta_g$, in other words is much larger than all other timescales in the system then the excited state $|e\rangle$ can be adiabatically eliminated.

By having a large detuning Δ the excited state population is suppressed allowing upper state decay processes to be safely neglected. This is a key reason that manipulations between the ground-state spins of charged quantum dots are attractive. Since they are not limited by the short decay times of the excited trion states and the system naturally will have a larger coherence evaluated from off-diagonal matrix elements of the density operator $\rho_{21} = c_1^* c_2$.

Absorption and emission of a photon within the Λ-system now has the effect of coherently transferring the population between the two ground states $|g_1\rangle\,,|g_2\rangle$. Using adiabatic elimination by taking $\dot{c_e}(t) = 0$ we find,

$$c_e(t) \to c_e = -(\Omega_1^* c_1 + \Omega_2^* c_2)/(2\Delta), \tag{4.22}$$

which can then be substituted back into 4.19-4.20 to reduce the three-level system to a two-level system. This two-level system is now between the ground states and is governed by an effective Hamiltonian,

$$\hat{\mathcal{H}}_{\text{eff}} = \begin{pmatrix} \frac{|\Omega_1|^2}{4\Delta} & \frac{\Omega_2^*\Omega_1}{4\Delta} \\ \frac{\Omega_2^*\Omega_1}{4\Delta} & \delta_g + \frac{|\Omega_2|^2}{4\Delta} \end{pmatrix}. \tag{4.23}$$

The previous works of [122, 146] showed that for this quantum dot system the diagonal terms $|\Omega_1(t)| = |\Omega_2(t)| = |\Omega(t)|$ are equivalent to an AC Stark shift on both states by the same amount. Due to this special case we can subtract off the common diagonal terms and define an effective Rabi frequency as $\Omega_{\text{eff}}(t) = -\Omega_2^*\Omega_1/(2\Delta)$. This results in the simplified effective Hamiltonian between the ground states $\{|g_1\rangle, |g_2\rangle\}$,

$$\hat{\mathcal{H}}_{\text{eff}}(t) = \begin{pmatrix} 0 & -\Omega_{\text{eff}}(t)/2 \\ -\Omega_{\text{eff}}^*(t)/2 & \delta_g \end{pmatrix}. \tag{4.24}$$

To understand how this now relates to a system of coupled ground states which make up the spin-qubit, we move to a frame rotating at the Larmor frequency δ_g by defining the transformation $\left|\tilde{\psi}\right\rangle = c_1 |g_1\rangle + \tilde{c_2} e^{-i\delta_g t} |g_2\rangle$. Upon substitution and the inclusion of an arbitrary phase factor ϕ, the final effective spin Hamiltonian reads,

$$\hat{\tilde{H}}_{\text{eff}}(t) = \begin{pmatrix} 0 & -\frac{\Omega_{\text{eff}}}{2} e^{-i(\delta_g t+\phi)} \\ -\frac{\Omega_{\text{eff}}^*}{2} e^{i(\delta_g t+\phi)} & 0 \end{pmatrix}. \tag{4.25}$$

The previous works of [122, 146] also showed that Ω_{eff} will generate an angular rotation θ around the polar axis of the Bloch sphere. Experimentally, this results from the the rapid application of the pulse from the mode-locked laser.

The Tsunami laser used for the experiments shown operated under ps-timescales sending one fixed pulse every ∼12 ns. As the pulses are static and fixed with a particular width τ, the pulse area is altered by varying the power of the pulse, the amplitude of this pulse is proportional to the Rabi frequency Ω_{eff} of the applied pulse integrated over time.

The angular rotation can thus be written in terms of the pulse energy ϵ_{pulse} and

detuning Δ can be written as $\theta = \varepsilon_{\text{pulse}}/\Delta$ [122, 146]. The result is Rabi-flopping between the ground state spin-qubit which will scale as the square of the electric field as $|\Omega| \propto |E_0|^2$.

The equatorial precession around the azimuth can be observed using Ramsey interferometry involving two time-separated $\theta = \pi/2$ pulses. During the dead time between these pulses the system will freely precess at the Larmor frequency δ_g.

4.3 Experimental details and results

The experimental procedure for the results shown in the remainder of this chapter are briefly described in this section. The quantum dot sample in the cryostat was maintained in the range of 6-8 K and a magnetic field applied in-plane under the Voigt configuration with $B_0 = 5$ T.

In figure 4.4 we see experimental spectra of the target QD with the experiment prepared. The rotation pulse introduced in section 3.3 is red-detuned with a peak center of ∼1358.25 meV while the quantum dot center at $B_0 = 5$ T is ∼1356.50 meV. This is equivalent to a detuning of approximately 423 GHz below the QD.

Of the four optically active transitions the highest energy outer transition was used to detect photons emitted during spin rotations. This was often chosen due to being at the maximum possible spectral distance from the rotation pulse to mitigate back-reflected laser light from the large pulse powers (10-100s mW). Emission from the observed transition is filtered and sent onto the SPCM as described in section 2.3.

The cross-polarized coupled inner transition was resonantly addressed with a CW laser. In ideal experimental conditions the CW laser would be gated, using either an acoustic/electric optical modulator, to prepare the system into a ground state prior to the pulse and readout. Near unit probability initialization system has been shown to occur within a few nanoseconds [64, 131]. For the experiment in this work the CW laser remained resonantly on the transition throughout acquisition.

With the setup as described a range of various experiments are available and will be discussed throughout the rest of this chapter. We begin with spin initialization

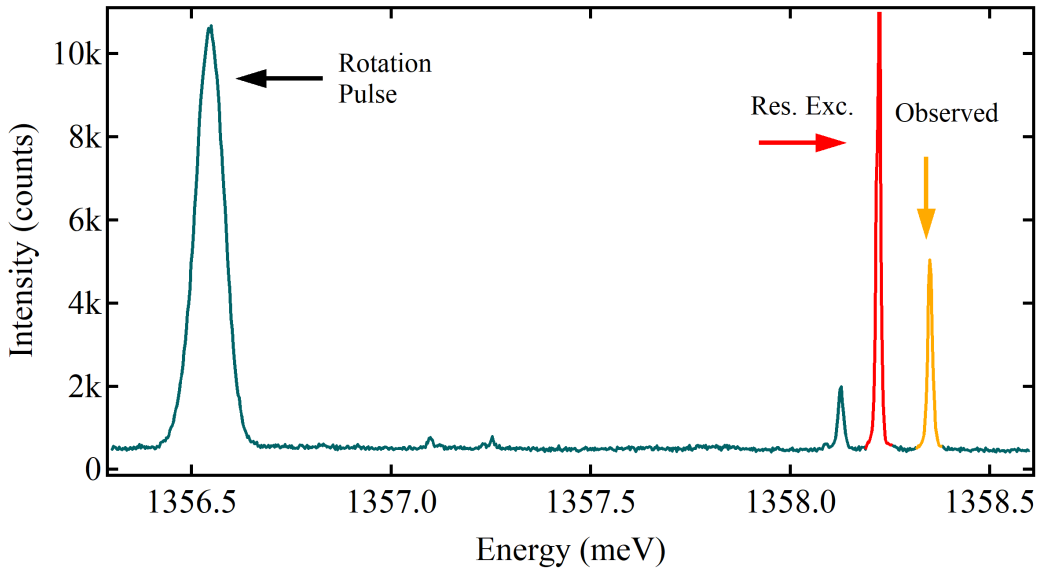

Figure 4.4: Experimental spectra of the setup for a QD centered at ∼1358.25 meV under a $B_z = 5$ T magnetic field. The far-detuned rotation pulse on left at ∼1356.50 meV. The highest energy (orange) is the observed transition while the lower energy inner transition (red) is resonantly addressed.

which is used to prepare the system into a desired ground state.

We then show that we can gain complete control over the state space spanned by the ground-state electronic spins by demonstrating control over two orthogonal axes of the Bloch sphere (θ, ϕ). Combining rotations of the polar and azimuthal axis allow arbitrary locations throughout the space to be accessed and are visualized in figure 4.5.

Figure 4.5 is split into three phases which all occur within successive pulses arriving approximately every 12.5 ns. The initialization phase results from resonant excitation on the QD transition as shown in figure 4.4 which will initialize the system within ∼3 ns through spin pumping. The rotation phase occurs when the ps-pulse with a FWHM of ∼2.5 ps generates the spin rotation between the ground state spins in this time. Finally, the readout phase will occur from the continuous resonant excitation as in the initialization phase. Dependent on the ground-state the system resides in after the rotation determines whether spin pumping occurs after an excitation-decay process, if a spin pumping process occurs a count is observed otherwise there is no

count and the state resides in the opposing ground state.

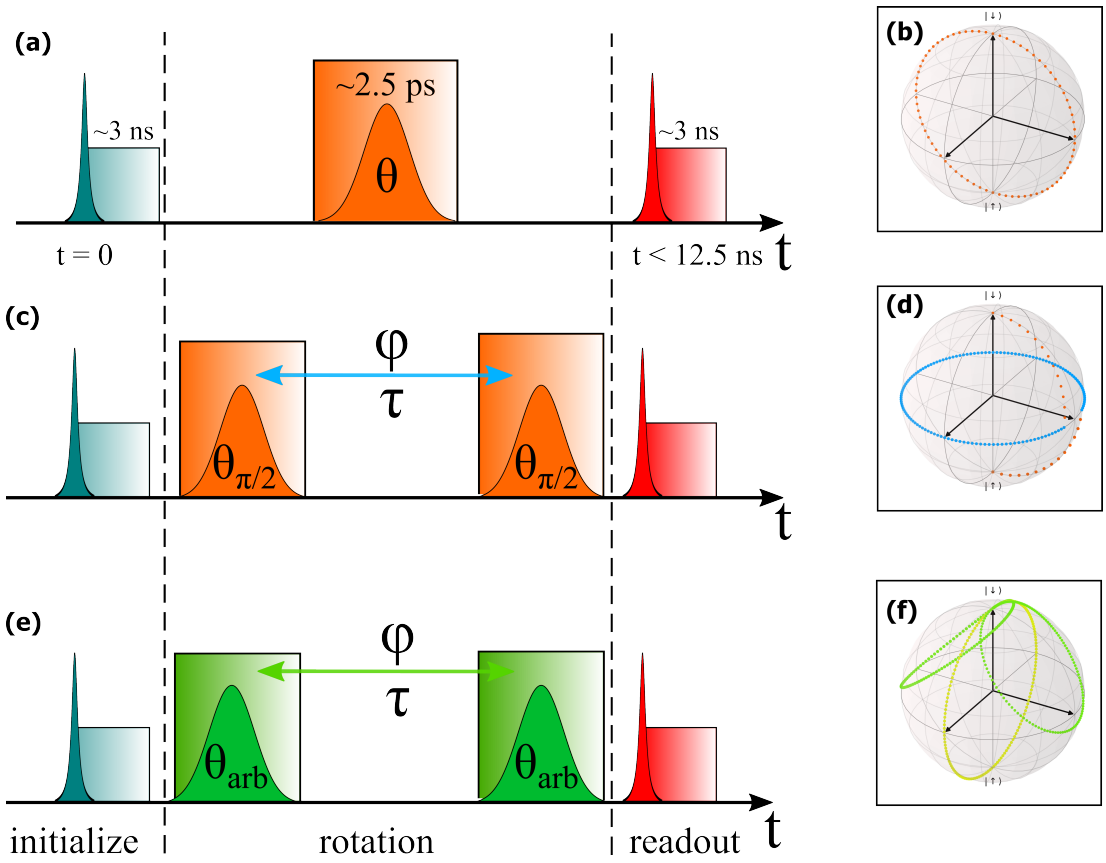

Figure 4.5: Experimental pulse sequences and Bloch representations for each coherent control experiment. The CW resonant laser initializes and reads out the state within an ~3 ns window while the spin rotations are generated by the pulsed laser in between. Each cycle occurs within 12.5 ns from the 88 MHz repetition rate of the pulsed laser. (a) Rabi rotation consisting of single pulse. (b) Rabi oscillations rotate around polar axis of Bloch sphere. (c) Ramsey interference is performed with two $\theta = \pi/2$ pulses separated by time τ. (d) Ramsey fringes precess around azimuthal axis of the sphere. (e) Coherent control is similar to (c) instead with two pulses of arbitrary equal powers θ_{arb} (f) Complete coherent control refers to accessing arbitrary locations as a function of (a) and (c).

We state here that the resonant excitation laser remains on throughout all three phases due to a lack of an optical modulator. An ideal scenario would include an AOM/EOM gated with the arrival of the ps-pulse, this would allow there to be no CW excitation in the rotation phase of the experiment. This is true throughout all experiments shown in this work with the current experimental setup. Future setups

would benefit from the inclusion of this equipment.

The polar axis is a function of the rotation pulse power and generates Rabi oscillations (fig. 4.5(a)-(b)) while the azimuthal axis is accessed using the magnetic field. This equatorial precession is shown via a Ramsey interference experiment (fig. 4.5(c)-(d)).

Finally the section is concluded by successfully *calibrating the experiment* with a demonstration of complete coherent control. Manipulating both orthogonal axes allows for arbitrary locations on the surface of the Bloch sphere to be accessed (fig. 4.5(e)-(f)).

4.3.1 Spin Initialization

As introduced in chapter 1 Di Vincenzo stated five criterion that are essential for implementing physical quantum computation [30] and originally proposed QDs as an ideal spin-qubit [59]. One criteria states that deterministic loading of a qubit system into an initial state is essential prior to any subsequent operations being performed.

Each of the excited states within a Voigt configured QD $\{|\uparrow\downarrow\Uparrow\rangle_x, |\uparrow\downarrow\Downarrow\rangle_x\}$, as in 4.1(c), yield equal probability to decay into the electronic ground states $\{|\uparrow\rangle_x, |\downarrow\rangle_x\}$. Spin-pumping is an initialization process in which we deterministically pump (or load) the system into either the $|\uparrow\rangle_x$ or $|\downarrow\rangle_x$ states with a CW laser resonant on one of the four polarization-resolved transitions.

Consider a laser resonant on the $|\uparrow\rangle_x \rightarrow |\uparrow\downarrow\Uparrow\rangle_x$ transition, any population is transferred to the trion state $|\uparrow\downarrow\Uparrow\rangle_x$ and will decay with equal probability to the either of the ground states $\{|\uparrow\rangle_x, |\downarrow\rangle_x\}$. If the system decays back to the initial state it will simply be re-pumped back to the trion state. After a short period, ~ 3 ns for self-assembled InGaAs quantum dots [64], the system is deterministically *loaded* into the ground state $|\downarrow\rangle_x$ after which it will remain until either the spin relaxes or an operation is performed that will alter the state.

The experimental spin-pumping procedure involves weak ($< 2.5\%$ of saturation power P_{sat}) above-band excitation that randomizes the state of the spin in the ground states. Above-band excitation incoherently excites energies higher than the QD trion levels and through a series of decay processes passes through the trion levels random-

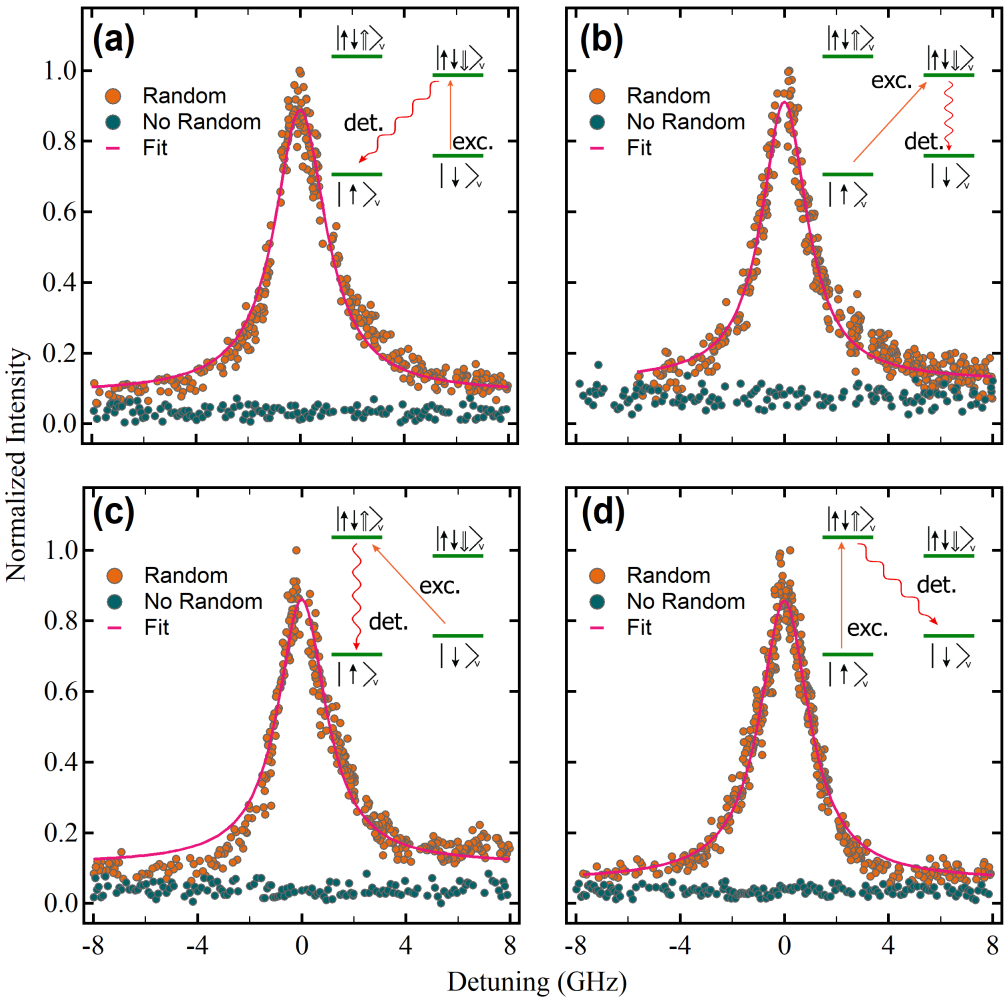

Figure 4.6: (a)-(d) Spin pumping of all available transitions as a function of excitation laser detuning in the Voigt configuration. Normalized emission intensity vs single photon counts with (i) randomization and (ii) no randomization applied. Dashed line Lorentzian best fit. Inset (top right) shows excitation and detection scheme for each.

izing the population. Sweeping the resonant laser across a transition during randomization yields the Lorentzian spin pump curves observed in figure 4.6(a)-(d), with each individual experiment described by the associated inset.

Each detection path is passed onto an SPCM measuring counts in 0.1 ms intervals after the spectra is filtered through the spectrometer slits. The polarization of the excitation laser and emission detected from the quantum dot are orthogonally-polarized

under a Voigt configuration allowing a high signal to background ratio. The back-reflected laser light is easily minimized through cross-polarized reflectivity under this configuration enhancing data collection.

The pink lines in figure 4.6 are the best-fit using a Lorentzian function while the blue data points show the experiment run without any above-band randomization. The lack of counts observed with no-randomization is indicative that the electron spin-lifetime is long with respect to the detection interval of 0.1 ms.

Comparison of the no-/randomization shows there no notable increase in counts observed when the CW laser is on resonance at zero detuning case of no above-band randomization. The ratio of the peak signal at zero detuning for each case could be used to determine the spin pumping fidelity through a rate equation model [120]. The fidelity of the spin initialization would most predominantly be limited by the finite spin lifetime. If the spin lifetime was significantly low it would lead to a reduced fidelity and we would observe an increase in counts at zero detuning for the blue data points in figure 4.6. For all measurements taken here there is no observable increase in counts at zero detuning with each of the counts lying within the noise background. The average value for the count-offset between the randomized and un-randomized, (i) and (ii), was $\sim$250 counts.

An additional effect was also observed during the results presented in chapters 5 and 6 while performing the spin pumping experiments shown here under oblique magnetic fields. This spin pumping protocol can instead be performed using a pulsed laser set to yield a Rabi pulse power (discussed next) with a π-pulse area.

The result should be a complete transfer of the system from the initial ground state to the other coupled ground state resulting in emission of a photon. When the pulse power of the resonant laser is sufficiently low an interference effect can be observed between photons emitted from the quantum dot and the resonant laser tuned to the same frequency. Further details are presented in Appendix B.

4.3.2 Rabi oscillations

From the analysis of the 3-level Λ-system we found the effective Rabi frequency to be a function of the individual frequencies and the detuning, $\Omega_{\text{eff}} = -\Omega_2^*\Omega_1/(2\Delta)$. It was also stated that the rotation on the polar axis is represented by the angle $\theta \propto |\Omega_{\text{eff}}|$.

The 3-level system is useful for demonstrating the physics that occur within a charged quantum dot exhibiting a Λ-structure yet as seen in figure 4.1(c) the complete system is a double Λ-system each containing two cross-polarized transitions. The effect is that the effective Rabi frequency is now a function of the laser pulse affecting the entire system as opposed to the 3-level model described previously. Again, by leaning on previous works that pioneered this physics [122, 146], it can be shown that a slight modification of the effective Rabi frequency can be done. This is to include both Λ-systems and helps to identify the condition that optimizes Rabi-flopping under a Voigt configuration.

This involves defining the Rabi frequencies of the excited trion states as $\{\Omega_{\uparrow\downarrow\Uparrow}, \Omega_{\uparrow\downarrow\Downarrow}\}$ and the electric field polarization in component form as $\varepsilon = E_H\hat{x} + E_V\hat{y}$. From this we can then write [122],

$$\Omega_{\uparrow\downarrow\Uparrow} = -i\frac{\Omega_V^*\Omega_H}{4\Delta + \delta_h}, \tag{4.26}$$

$$\Omega_{\uparrow\downarrow\Downarrow} = i\frac{\Omega_V\Omega_H^*}{4\Delta}. \tag{4.27}$$

On the safe assumption that the detuning far exceeds the level splitting $\Delta \gg \delta_h$, easily verified with figure 4.4, we can define the effective Rabi frequency for the 4-level structure as,

$$\begin{aligned}\Omega_{\text{eff}} &= \Omega_{\uparrow\downarrow\Uparrow} + \Omega_{\uparrow\downarrow\Downarrow}, \\ \Omega_{\text{eff}} &= -i\frac{|\Omega|^2}{4\Delta}(E_V^*E_H - E_VE_H^*).\end{aligned} \tag{4.28}$$

Equation 4.28 shows that under a Voigt configuration the effective Rabi frequency

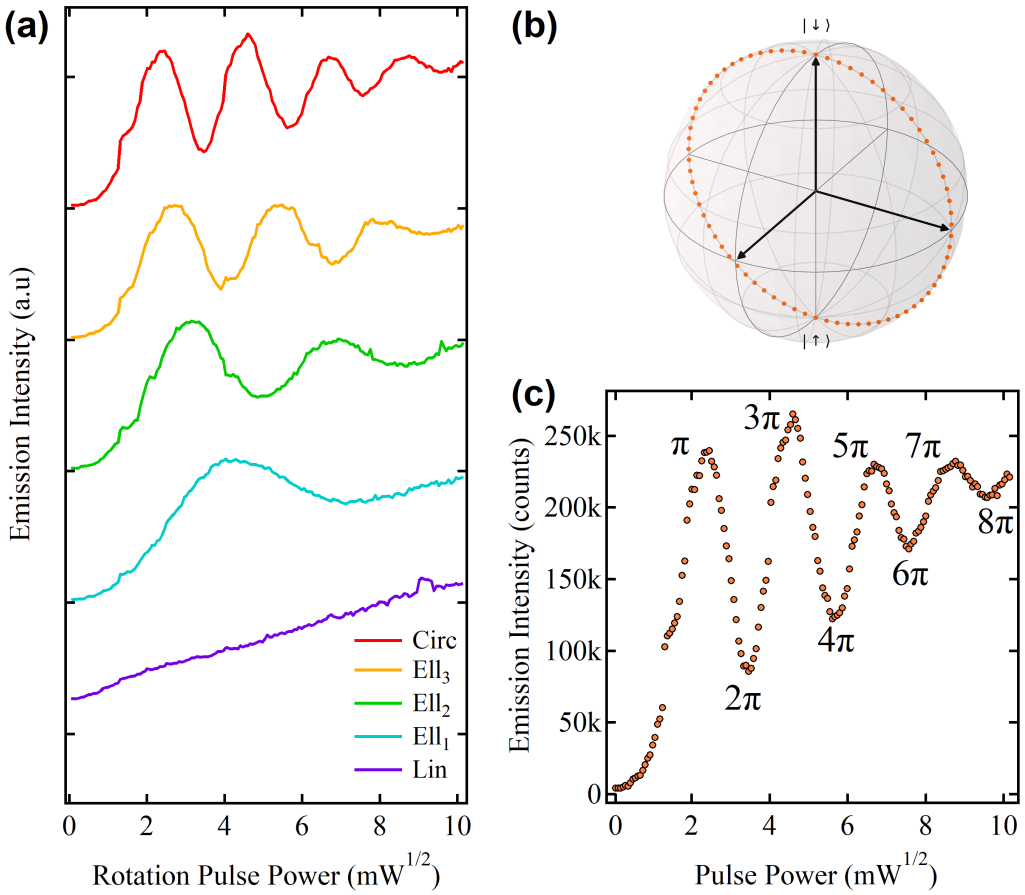

Figure 4.7: (a) Rabi oscillations of a QD as a function of the pulse polarization, fully linear does not generate rotations while the rotations are maximized when circular. Data offset for clarity. (b) Rendition of a Rabi oscillation on the Bloch sphere moving from pole to pole. (c) Rabi oscillation maintaining coherence up to 8π worth of rotations. Diminished contrast at higher values is a result of decoherence effects.

is maximized on the condition that the pulse is circularly polarized such that $E_V = \pm iE_H$. Conversely, $\Omega_{\text{eff}} \to 0$ when the pulse is linearly polarized resulting in no coherent oscillations between the ground states $|\downarrow\rangle$ and $|\uparrow\rangle$.

This effect can be observed clearly with the waterfall plot in figure 4.7(a) demonstrating Rabi oscillations as a function of the pulse polarization with an ~2.5 ps full-width half maximum pulse. When the pulse is entirely linear (purple) 4.28 will equal zero and no oscillations will be observed. With the linear polarization we see only an

increase in background counts that is mostly attributed to back-reflected laser light from the rotation pulse. When performing measurements one run uses the same power curve of the pulse with the absence of a resonant laser to initialize the state. This results in a measurement of the background counts which can then be subtracted from the data to reveal the bare Rabi oscillations.

As we move the pulse polarization through elliptical towards fully circular we see a clear increase in the oscillation frequency as the effective frequency is maximized. At entirely circular polarization (red) the optimized Rabi rotation shows multiple rotations around the polar axis of the Bloch sphere depicted in 4.7(b).

The optimized circular pulse data is shown in figure 4.7(c) where we see the coherence maintained through over 8π of rotations. The reduction in the contrast at larger powers results from the decoherence that can be interpreted as a reduction in the length of the Bloch vector.

4.3.3 Ramsey and SU(2)

Observation of control over the azimuthal axis is most easily seen through a Ramsey interference experiment. The applied magnetic field leads to level splitting of the ground state spins and the system can be prepared in a coherent superposition $|\psi\rangle = (|\downarrow\rangle + e^{-i\omega_{\text{larmor}}\Delta t\varphi}|\uparrow\rangle)/\sqrt{2}$ through application of a rotation pulse with pulse area $\theta = \pi/2$.

Application of two time-separated $\pi/2$ pulses allows control over this axis. The first $\pi/2$ pulse sends the state to the equator where it will precess at the Larmor frequency ω_{larmor} accumulating a relative phase. When the second pulse arrives it will project the system back into either $|\uparrow\rangle$ or $|\downarrow\rangle$ dependent upon the the value of the accumulated phase. This is detected through emission from the observed transition, or lack thereof, respectively.

Practically, by evaluating the pulse power equivalent to $\theta = \pi/2$ in figure 4.7(c) this fixed value upon application will create the superposition state $|\psi\rangle$. The second $\pi/2$ pulse, using the unbalanced Mach-Zehnder delay stage setup in section 3.3, then projects the system back to the states $\{|\downarrow\rangle, |\uparrow\rangle\}$ and is observed in figure 4.8. This maps

on to the Bloch sphere shown in the inset where the orange dots indicate the pulses and the blue dots are the precession.

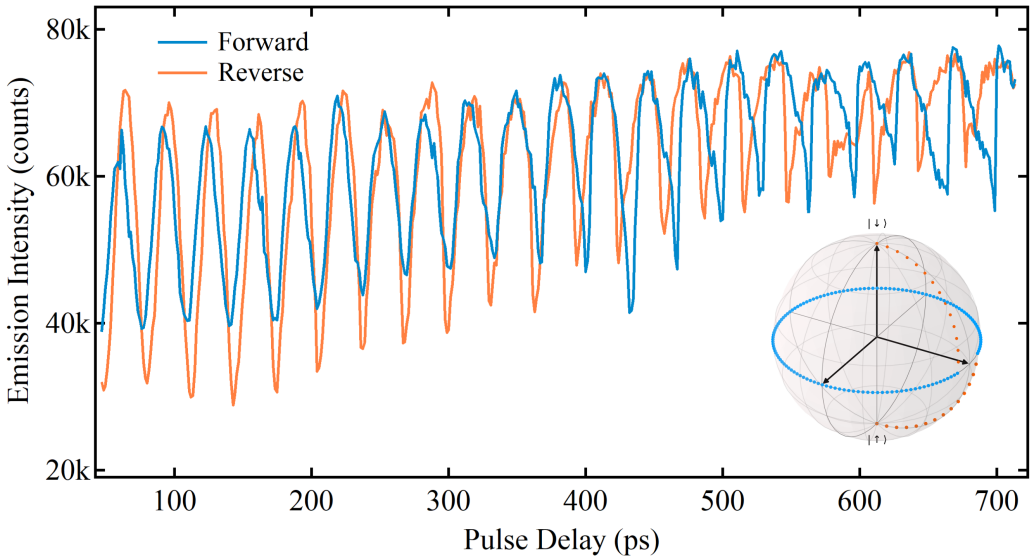

Figure 4.8: Ramsey oscillations for increasing (forward) and decreasing (reverse) pulse delays showing coherence after up to 700 ps of pulse delay. At higher pulse delays (> 450 ps) nuclear polarization is observed by the sawtooth fringe pattern. Inset shows Ramsey rotations on the Bloch sphere precessing around the azimuthal axis.

From the data we see clear Ramsey fringes over ∼700 ps of pulse delay and the forward (reverse) data determines whether the measurements began at the minimum (maximum) pulse delay τ. A sawtooth fringe becomes visible in the data for $\tau > 450$ ps that is mirrored across both datasets. This has been qualitatively described as a result of nuclear polarization processes in [147]. In this work they posit that nuclear spin-flips with the neighboring nuclei generates an Overhauser magnetic field which in turn leads to variations in the Larmor frequency ω_{larmor}. Additionally, the resonant pump laser is shown to affect the trion creation in the system which results in the sawtooth pattern shown. We refer the reader to [147] for further details.

The fringe contrast decays over longer timescales and is related to the decoherence properties of the system for longer precession times. Generating a spin echo pulse sequence ($\pi/2 \rightarrow \pi \rightarrow \pi/2$) would extend these coherence times and the rate of decay of the fringe contrast from which one could extract the T_2^* coherence time [71, 118]. This

would be done by fitting the measured data with a form consisting of a Gaussian envelope and a decaying exponential function which will extract the coherence time. The Hahn-echo pulse sequence greatly extends the coherence and values of $T_2^* = 200$ μs have been demonstrated for GaAs spin-qubits [148].

The center π-pulse required for the spin-echo sequence was not possible to create experimentally as the two-pulse experiment is formed using $\pi/2$-pulses. To introduce the center π-pulse is experimentally challenging for the setup in this work. To gain this degree of control often requires either an AOM/EOM to allow manipulation of the pulses on the ps-timescales presented.

Investigation into methods to produce this pulse sequence led to the understanding that an additional third arm of the interferometer alongside a combination of retarders and polarization optics to control the power would make this possible. Although the implementation would be both complex and require significant additional space and time on the optical bench.

Combining these to form the function $R(\theta, \varphi)$ yields the capability to access every point on the surface of the Bloch sphere and leading to a demonstration of complete coherent control. Varying the pulse power generates coherent superpositions with arbitrary weightings and during the period τ between successive pulses a phase difference accumulates between the states.

Figure 4.9(a)-(b) highlight the pulse power and time delay used for each axis for the Rabi and Ramsey experiments, respectively, and by combining both measurements we observe the two-dimensional map of figure 4.9(c). Each high intensity center can be interpreted as the combination of $R(\theta, \varphi)$ that will project the system into $|\uparrow\rangle$ leading to maximal emission from the QD. The maximal values of the sine curve in fig. 4.5(b) ($\sim$73, 105, 140 ps) align with the optimal contrast Rabi oscillations along the vertical axis of the 2D map. A pulse power of $\sim$4.78 $\text{mW}^{1/2}$ equates to a rotation angle of $\theta = 5\pi$ at which point the coherence of the system has reduced leading to the less distinct peaks. In essence, figure 4.9(c) spans the entire space of SU(2) rotations with approximate bounds for the rotations of $\{\theta \in (0, 6\pi), \varphi \in (0, 5\pi)\}$ where $\sim$60 ps is taken as the relative start position.

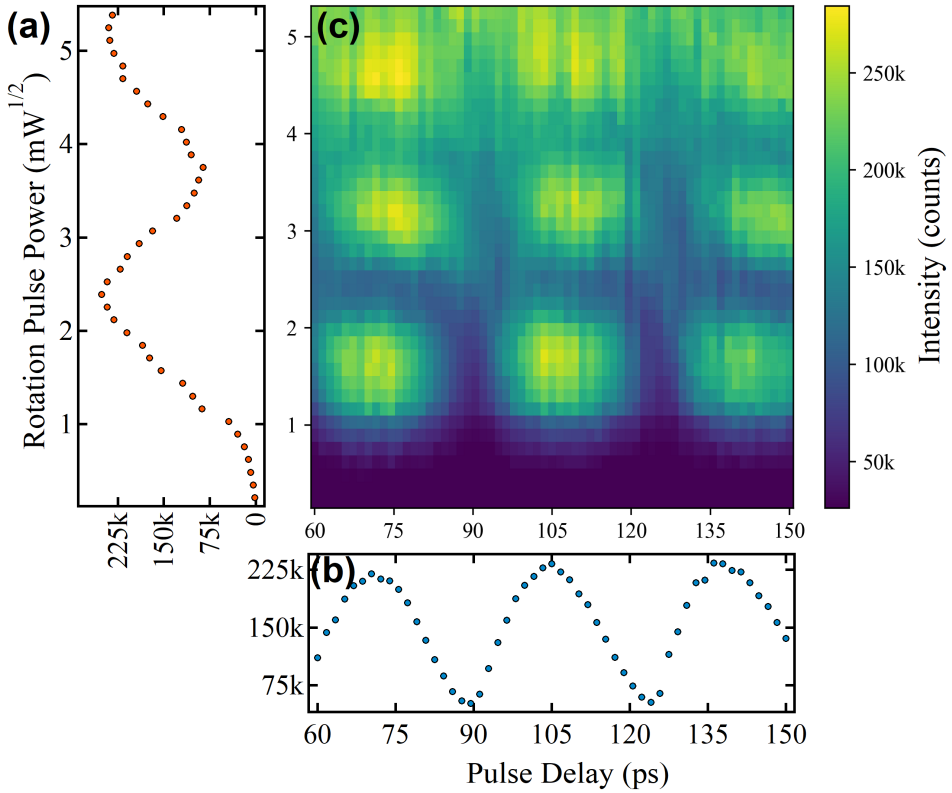

Figure 4.9: (a) Rabi oscillation used for complete coherent control map in (c). (b) Ramsey fringes aligned with coherent control map in (c), the intensity peaks align with a Ramsey projection to the excited state. (c) Complete coherent control map of QD under Voigt configuration. Each high intensity peak can be regarded as mapping to the south pole of the Bloch sphere.

This can also be visualized by generating a surf plot of the data as seen in figure 4.10(a). For a system initialized into $|\downarrow\rangle$ the states located at the north and south poles are $|\downarrow\rangle$ and $|\uparrow\rangle$ respectively. Each of the high intensity peaks then relate to the southern hemisphere of a Bloch sphere and conversely the low intensity valleys correspond to the upper hemisphere yielding a topological map of the space of SU(2) rotations through experimental data.

Figure 4.10(b) shows a vertical slice of the two-dimensional map for $\tau = 74$ ps and shows significantly improved quality with respect to figure 4.9(a). This is not an identical process to the previous data, one-pulse versus two-pulse sequences, yet it is

clear to see that values of τ that ensure maximal population of $|\uparrow\rangle$ appear to enhance the fidelity of either state preparation or readout. The frequency of oscillation shows a 2x improvement using equivalent pulse powers and persists with a longer coherence of oscillation. This is reinforced further as the count-rate for odd multiples of π (peaks) show less deviation than a one-pulse experiment.

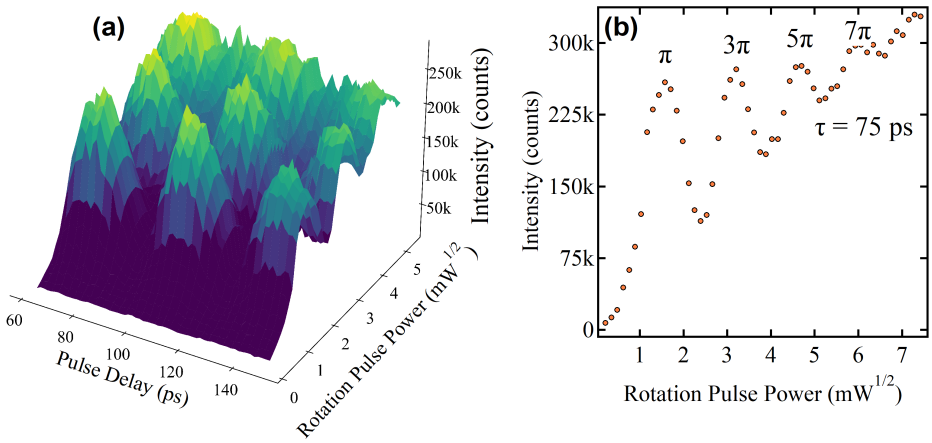

Figure 4.10: (a) Surf plot visualization of the coherent control map in 4.9(c). (b) Oscillations taken from the data in (a) for a pulse delay of τ = 74 ps, at which the Ramsey fringe is at a maximum, showing improved coherence.

Various runs of this experiment were performed on various different quantum dots (not shown in this work) and this observation has proven to be consistent and reproducible. The author believes that experiments focused on quantifying the behavior of the two-pulse sequence would yield understanding to help further enhance fidelity of state preparation and readout to near unity values. This is an essential research goal for many applications in quantum information processing and understanding the physics to reliably enhance spin-qubit systems allows more resources towards scalability and designing new quantum hardware architectures.

4.4 Conclusion

In conclusion, the chapter introduced the charged quantum dot system working from a simple Zeeman Hamiltonian to understand the effects the magnetic field strength and orientation. We highlighted the effects this has on the polarization and selection rules and described the system under both Faraday and Voigt configurations.

A description of a three-level Λ-system was introduced to demonstrate ground-state electronic spins being harnessed as a spin-qubit that is robust against decay processes linked with the excited states. This was shown to be a key feature of ultra-fast coherent control in which the large detuning of the pulse allows adiabatic elimination of the systems upper trion states.

Finally, calibration of the setup was successfully shown through a series of experiments to demonstrate complete coherent control of a negative singly-charged QD using the physics described in section 4.2.

The work presented here proved to be an essential step in developing the high level technical skill and understanding required to generate the new results of subsequent chapters. Henceforth, we aim to characterize charged quantum dots under an oblique magnetic field prior to extending the results of this section to oblique configurations.

Chapter 5

Towards Spin State Tailoring using Oblique Magnetic Fields

Self-assembled semiconductor quantum dots under applied magnetic fields are well understood in both Voigt and Faraday geometries, with each having applications in quantum information processing. The previous chapter demonstrated all-optical coherent control of charged quantum dots under a Voigt configuration highlighting the potential as a solid-state matter-qubit. The techniques were possible due to the double-Λ level structure. We saw that a charged QD transitions under the Voigt configuration are linearly polarized, this is understood as the applied field $\mathbf{B} = \mathrm{B}_x$ mixing the electronic basis states in equal proportions as seen by the $\sqrt{2}$ normalization factor in $|\uparrow(\downarrow)\rangle_x = (|\uparrow\rangle_z \pm |\downarrow\rangle_z)/\sqrt{2}$. This is in opposition with the Faraday configuration known to emit only $\hat{\sigma}^{\pm}$ light where there is not mixing between the basis states.

This begs the question what can be expected from a charged QD under oblique magnetic field configurations, which then drives the experiments shown in this section. On the assumption that there is a continuous smooth transition from an unmixed Faraday configuration to an equally mixed Voigt configuration, there must then exist QD level structures composed of basis states with varying weights of the basis spin-states.

Magnetic fields that are applied with varying angles in the plane perpendicular to the growth axis enable characterization of the in-plane g-factors. Combining

these measurements with magnetic field out-of-plane allows for the estimation of the complete g-factor tensor of a quantum dot. This is typically done via application of magnetic fields in oblique angles using in parallel additional techniques ranging from photo-luminescence polarimetry [37,141–143,149–152], pump-probe Faraday rotation [153–156] and resonant spin amplification [157] to spin-noise spectroscopy [158], magneto-tunneling [159,160], and magneto-capacitance [161].

We verify that the energy levels of a charged QD can be tailored to yield a range of unequal basis state configurations as a function of a non-zero magnetic field. These unbalanced spin-state weights revealed at obliques angles show the ground states can have a tailored spin composition. This may have applications towards spin-selective readout and measurement schemes similar to those that create pseudo-Faraday configurations [162]. Additionally, we find that there still exists a coupled level structure typical of the Voigt configuration that has proven essential for all-optical spin control [124,135] indicating direction for further research.

This chapter is presented as follows; section 5.1 introduces theory and simulations of self-assembled InGaAs QDs using parameters from experiments under an oblique magnetic field ($\theta_{obl} = 60°$). From this we identify the behavior under arbitrary magnetic field angles. Full expressions of the spin-state eigenstates are shown alongside the effective polarizations of the transitions. Section 5.2 shows the experimental methods used to characterize the level structure and techniques to compare theory and experiment. This was conducted using Stokes polarimetry from QWP polarimetry data. Spin pumping of the QD transitions under oblique fields is shown revealing a reduced coupled double-Λ system. Finally, a brief experimental investigation into whether Overhauser shifts were present in the target QD are presented.

5.1 Simulations and Theory

As described in section 4.1 the electronic states of a charged QD are subject to the Zeeman interaction in the presence of a magnetic field. As we work with negatively charged quantum dots it is known that there is no notable exchange interaction [141].

To model the charged QD system we treat both electrons and the trions as pseudo-spins; the electrons naturally have spin $\hat{J}_e = \pm 1/2$ while the trions with spin $\hat{J}_h = \pm 3/2$ that are associated with the heavy-hole (hh) states. We choose to neglect the light-hole (lh) states due to the large strain-induced energy splitting common in self-assembled QDs [141]. Additionally, by verifying and pre-selecting the target QD we find no significant hh-lh mixing occurs. We can then deduce the form of the Hamiltonian for both the electrons and heavy holes within the QD to be given by 4.1 . Now we consider a varying field angle $\theta \in [0, \pi/2]$ in the z-x plane with 0 aligned along the Faraday configuration (z-axis) and 90° the Voigt configuration (x-axis).

For the hole states we use the Luttinger-Kohn Hamiltonian and the valence-band parameters κ_α and q_α, akin to Bayer [141] *et al.* and other works [37, 142, 143]. By introducing the heavy-hole subspace matrices for $\hat{J}_\alpha$ and $\hat{J}_\alpha^3$ [163] the hole Hamiltonian can then be reduced to a form akin to 4.1 . Similarly, this contains only spin-$\frac{1}{2}$ operators and differs by a sign pre-factor. In the presence of hh-lh mixing the full $\hat{J}_h$ matrices with additional parameters relating to the hh-lh mixing ratio would be required. In this case it would be necessary for a model using the full Luttinger-Kohn or Bir-Pikus Hamiltonian [37, 164] or a *k.p* model [165, 166]. Here we simplified the model by pre-selecting the quantum dot studied for minimal hh-lh mixing. Using an additional polarimetry experiment performed under the Faraday geometry it showed a very high degree of circular polarization indicative of a negligible mixing ratio.

These Hamiltonians can be readily diagonalized to understand the quantum dots response to an applied magnetic field. Figure 5.1(a) shows a schematic diagram of the system consisting of the electronic ground states, $|\uparrow\rangle_\theta$ and $|\downarrow\rangle_\theta$, and excited trion states, $|\uparrow\downarrow\Uparrow\rangle_\theta$ and $|\uparrow\downarrow\Downarrow\rangle_\theta$. Here $\uparrow, \downarrow$ relate to the ground state electron spins while $\Downarrow, \Uparrow$ relate to the hole spin states. From this the resultant excited trion state then refers to a charged QD configuration. The angle θ is aligned with respect to the z-axis as is also shown in figure 5.1(a) such that $\theta_F = 0^\circ$ and $\theta_V = 90^\circ$.

Under an applied magnetic field each spin eigenstate is composed of a linear combination of the basis states aligned along the z-axis ($\theta_z = 0^\circ$). These are written as either $\{|\uparrow\rangle_z, |\downarrow\rangle_z\}$ or $\{|\uparrow\downarrow\Uparrow\rangle_z, |\uparrow\downarrow\Downarrow\rangle_z\}$ for the ground and excited trion states, respec-

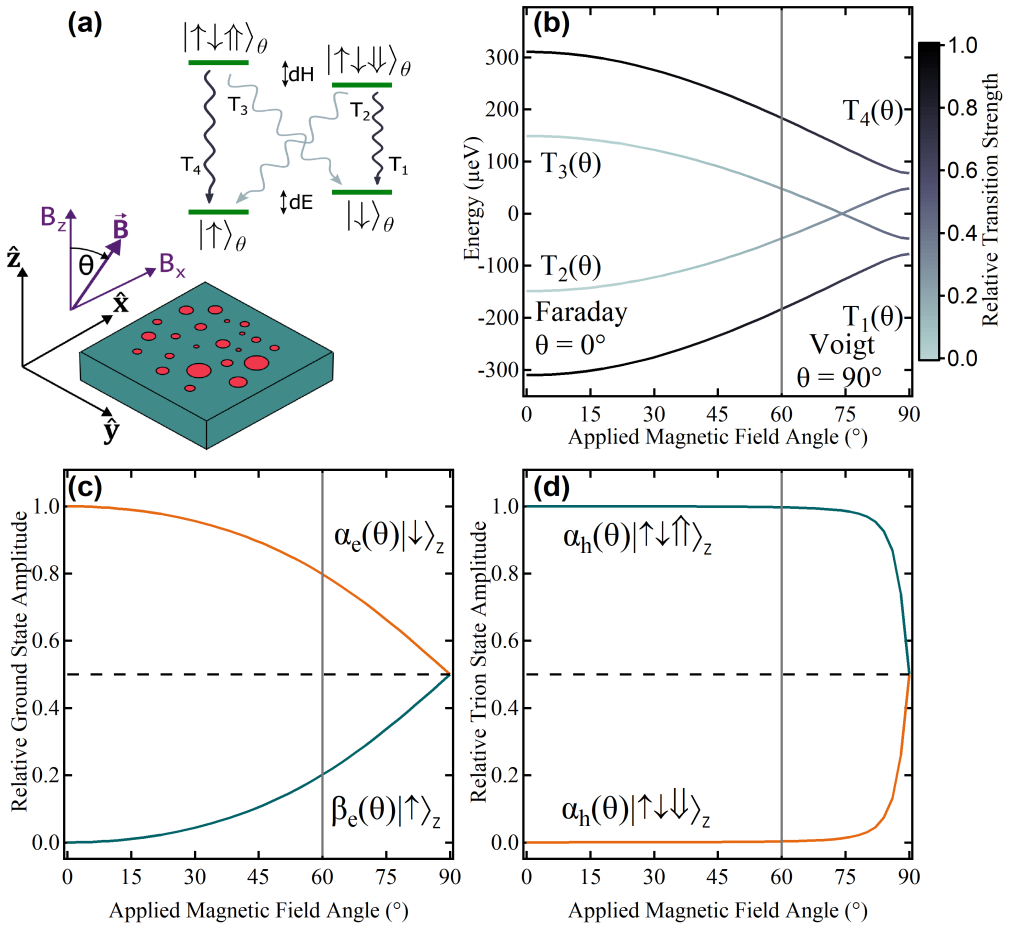

Figure 5.1: (a) Simulated results of a charged QDs four-level splitting (T_1-T_4) as a function of applied magnetic field angle (B_0 = 5 T) using g-factors found from experimental data in adjacent plot. The color bar indicates the relative transition intensity for each transition while the vertical grey bar highlights $\theta_{obl} = 60°$ (b) Level splitting of the QD as a function of magnetic field strength in the Voigt (left) and 60° oblique (right) configuration. T_2 and T_3 exchange relative positions between configurations.

tively. This then allows us to express the eigenstates as a linear combination of the basis states as,

$$|\uparrow\rangle_\theta = \alpha_e(\theta)\,|\uparrow\rangle_z - \beta_e(\theta)\,|\downarrow\rangle_z\,, \tag{5.1}$$

$$|\downarrow\rangle_\theta = \beta_e(\theta)\,|\uparrow\rangle_z + \alpha_e(\theta)\,|\downarrow\rangle_z\,, \tag{5.2}$$

$$|\uparrow\Downarrow\rangle_\theta = \alpha_h(\theta)\,|\uparrow\Downarrow\rangle_z - \beta_h(\theta)\,|\uparrow\Downarrow\rangle_z\,, \tag{5.3}$$

$$|\uparrow\Downarrow\rangle_\theta = \beta_h(\theta)\,|\uparrow\Downarrow\rangle_z + \alpha_h(\theta)\,|\uparrow\Downarrow\rangle_z\,, \tag{5.4}$$

where $\alpha_{e/h}(\theta)$ and $\beta_{e/h}(\theta)$ are the normalized weights of the electron (hole), found through explicitly solving 4.1 . After diagonalization of the Zeeman Hamiltonian we can determine the parameters affecting the spin-state compositions. From this we find the following expressions for both the weights $\alpha_{e/h}(\theta)$, $\beta_{e/h}(\theta)$ and the normalization factor $N_{e/h}(\theta)$. The full explicit expression for each are as follows,

$$\alpha_{e/h}(\theta) = \frac{1}{N_{e/h}}\left(g^z_{e/h}\cos\theta + \sqrt{(g^z_{e/h}\cos\theta)^2 + (g^x_{e/h}\sin\theta)^2}\right), \tag{5.5}$$

$$\beta_{e/h}(\theta) = \frac{g^x_{e/h}\sin\theta}{N_{e/h}(\theta)}, \tag{5.6}$$

$$\begin{aligned} N_{e/h}(\theta) = 2\Big(&(g^z_{e/h}\cos\theta)^2 + (g^x_{e/h}\sin\theta)^2 + g^z_{e/h}\cos\theta\Big)\,, \\ &-\sqrt{(g^z_{e/h}\cos\theta)^2 + (g^x_{e/h}\sin\theta)^2}\Big)\,, \end{aligned} \tag{5.7}$$

where $g^{z/x}_{e/h}$ are the g-factors for the electron(hole) in the z-(x-) directions, θ is the angle of the magnetic field taken with zero parallel to the z-axis.

As one would expect the eigenstates are a function of the particles g-factors and the angle and strength of the magnetic field. The physical shape between the many self-assembled InGaAs QDs found in a sample often yield a larger diameter along the x-y plane, which can be 4-10x greater than the height (∼2-5 nm) which lies along the samples growth axis (z-axis) [167].

The contribution of both in-plane and out-of-plane g-factors intuitively yields a larger relative separation between the transitions under a tilted magnetic field when compared with the Voigt configuration.

5.1.1 Tailoring the Spin-State Weights

We show simulated results of the four available transitions as a function of magnetic field angle θ in figure 5.1(b) for a charged QD ($B_0 = 5$ T). Peak emission of this charged QD at $B_0 = 0$ T was centered at 910.8 nm. We see the energy splitting of each transition as we move from 0 to 90° on the energy axis while each transitions line color shows the relative transition strengths. The transition strengths were found by evaluating the transition dipole matrix elements between the ground-state electron and (assumed) resident heavy-hole. This will be justified through the experiments shown further in this chapter.

Under the Faraday configuration ($\theta_F = 0°$) the two inner transitions become optically inactive as the relative transition strengths falling to zero. This is intuitively understood as an un-mixed composition of the basis states $|\uparrow\rangle_z, |\downarrow\rangle_z$. Upon recombination of the heavy-hole with a ground-state electron we see the circularly polarized emission described in chapter 4.

Conversely, under the Voigt configuration all transitions maintain equally active transition strengths due to a balanced mix of the basis states. The linear combination of the mixed states in equation 5.4 will, upon emission, lead to an equal mix of $\hat{\sigma}^{\pm}$ resulting in linearly polarized transitions.

With this particular charged QD the simulations show the inner energy levels $T_2(\theta)$ and $T_3(\theta)$ exchange position at $\theta \approx 74°$. This aligned well with experimental observations taken in the oblique ($\theta_{obl} = 60°$) and Voigt ($\theta_V = 90°$) configurations. Additionally, while at $\theta_{obl} = 60°$ the model predicts that the ratio of the emission intensity of the inner to outer transitions to be ~0.3.

The normalized weights of the electron spin in the ground state are shown in figure 5.1(c) while the weights of the hole spins in the excited states are in figure 5.1(d). In both cases there is a clear dependence on the magnetic field angle θ. At $\theta_F = 0°$ we retrieve pure spin-up and spin-down basis states, $|\uparrow\rangle_z$ and $|\downarrow\rangle_z$ whereas at $\theta_V = 90°$ the basis state contributions are balanced. In figure 5.1(c) we see that the electrons ground state amplitudes mix as they follow the external magnetic in a smooth continuous motion until θ_V.

A point of interest is the relationship of the trion state amplitudes shown in figure 5.1(d), we see that there is little mixing of the trion spin states until the angle is almost entirely in-plane ($\sim 70°$). This phenomenon can be understood by recalling that while we assume the hole spins to have a pseudo-spin character of $\pm 1/2$, they still have a total angular momentum value of $\hat{J}_h = \pm 3/2$. The result is the hole spins, which couple to linear combinations of opposite parity, are negligibly affected until the magnetic field is almost in-plane at which point there is sufficient energy to align the spins along $\vec{B}$.

By transitioning towards oblique configurations it is clear that the eigenstates are formed from unequal weights. This shows that an oblique external magnetic field allows for precise tailoring of the spin-up and spin-down components in the resultant electronic ground and excited states.

In this work we are most interested in the ground-state spins for the spin-qubit applications. The excited states share a similar behavior but as they exhibit shorter lifetimes the benefits would require more directed research.

5.1.2 Effective Polarizations

Previous research has shown polarization properties of charged QDs in oblique magnetic fields differ significantly from the Voigt configuration [151]. To further shed light on this behavior we characterized the state of QD emission using Stokes polarimetry as described in section 3.2. The elliptical polarizations present under oblique magnetic fields motivated the introduction of the QWP polarimetry setup to correctly evaluate the experimental polarizations.

In figure 5.2(a)-(d) we see the simulated results of the normalized linear (S_1) and circular (S_3) parameters as a function of applied field angle. Because of the chosen symmetry of the simulated system, the diagonal (S_2) component was zero for all magnetic field angles and thus was not displayed. The maximal values of $|S_1| = 1$ in the Voigt ($\theta_V = 90°$) and $|S_3| = 1$ in the Faraday ($\theta_F = 0°$) correctly match expectations. We note that the inner transitions $T_2(\theta)$ and $T_3(\theta)$ maintain some degree of linearity even under oblique angles near the Faraday configurations. However both transitions will

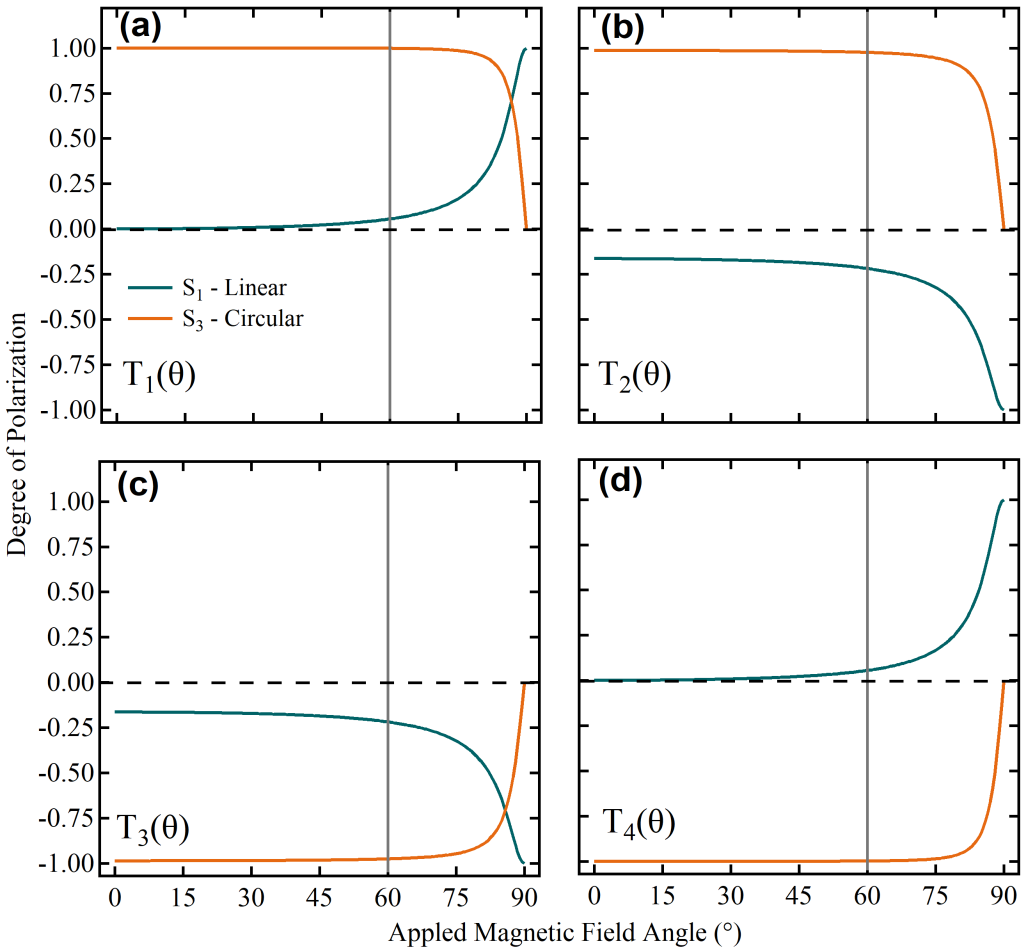

Figure 5.2: (a)-(d) Simulated polarization of light emitted from each transition as a function of applied magnetic field angle (B_0 = 5 T). We show only the linear (S_1) and circular (S_3) component of the Stokes vector as simulations show no diagonal component (S_2 = 0) is observed. A high degree of the linear S_1 component is seen to remain in (b) T_2 and (c) T_3 across all angles, the optical activity of these two transitions drops to zero for θ close to zero.

naturally become optically inactive at low angles making this observation difficult.

5.2 Experimental Results

5.2.1 Characterization of Level Structure

The four-fold splitting of singly charged excitons in the Voigt configuration leads to the characteristic double-Λ system. From this we are able to evaluate the in-plane g-factors in a straight forward manner. Under this configuration, ground and excited state splitting are a result of only the in-plane electron and hole g-factor components g_e^x and g_h^x which are readily obtained from experiment. Measurements of level-splitting and polarization-resolved photo-luminescence were taken under above-band excitation with power in the range of 250 $\pm$ 50 nW throughout data collection. This excitation power corresponds to only 20-40% of the saturation power found for this quantum dot ($P_{sat} = 740 \pm 20$ nW) from the saturation power measurement in figure 5.3. This ensured high-count rates whilst maintaining a narrow transition linewidth. The saturation power value was found by performing intensity-dependent photo-luminescence on the target QD.

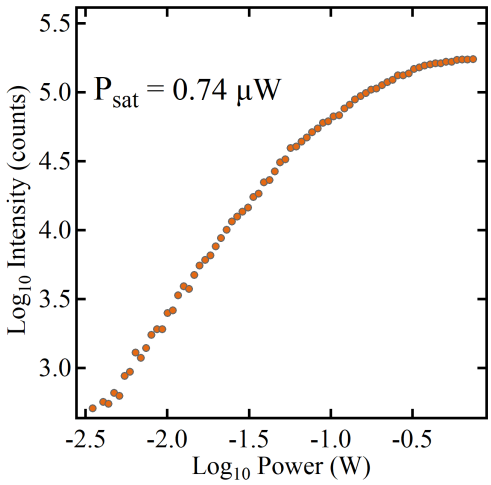

Figure 5.3: (a) Loglog of above-band power versus counts measured on SPCM. The power saturates at approximately 740 nW where power broadening of emission peaks saturates the QD.

In figure 5.4(b) we show level-splitting of the Voigt (left) and oblique (right) configuration as a function of the applied magnetic field strength with the diamagnetic

shift removed. The QD experiences a diamagnetic shift proportional to the square of the applied field alongside the linear Zeeman splitting. This can be removed first to accurately determine the g-factors. The raw data is shown in figure 5.5 for the (a) Voigt and (b) oblique respectively, clearly showing the effect of the diamagnetic on the level-splitting. Measurements of the level-splitting were taken in 0.5 T increments as the magnetic field ranged from 0-5 T, yielding multiple data points from which the g-factors could be evaluated alongside an associated error.

The Voigt diamagnetic shift factors were found to be $\alpha_V = 4.67\,\mu$eV / T^2, while the oblique configuration was $\alpha_{obl} = 6.14\,\mu$eV / T^2. By aggregating the multiple data points the in-plane g-factors were evaluated as $|g_e^x|$ = 0.442 $\pm$ 0.005 and $|g_h^x|$ = 0.111 $\pm$ 0.004.

Transitioning towards the oblique configuration at $\theta_{obl} = 60°$ in 5.4(b) (right) we see a similar four-fold splitting but with a greater magnitude of relative separation between the transitions. At $B_0 = 5$ T, we see an average 3-fold increase in the separation between adjacent transitions with respect to the splittings in the Voigt configuration. Immediate benefits of working in oblique configurations can be seen as to obtain similar level splitting to the Voigt at 5 T, the field strength can be as low as 2 T. Often when performing measurements optically nearby transitions and excitation lasers are spectrally close. This can make data acquisition of the observed transitions more difficult. By simply lowering the requirement of field strength, it can be adapted instead towards improving and extending coherence properties of the system [126].

Using the previously extracted in-plane g-factor components alongside the oblique measurements, out-of-plane g-factor components were evaluated as $|g_e^z|$ = 0.505 $\pm$ 0.032 and $|g_h^z| = 1.575 \pm 0.023$.

Noting the locations of transitions T_1-T_4 in the two different configurations in figure 5.4(b), we see that $T_2(\theta)$ and $T_3(\theta)$ exchange positions between the Voigt and oblique configuration. Figure 5.1(b) showed that this level crossing between T_2 and T_3 would take place at around 74° which lies in-between the two magnetic field configurations used in this work. Figure 5.4(c) demonstrates the experimental technique used to confirm this behavior. By combining above-band and resonant excitation on

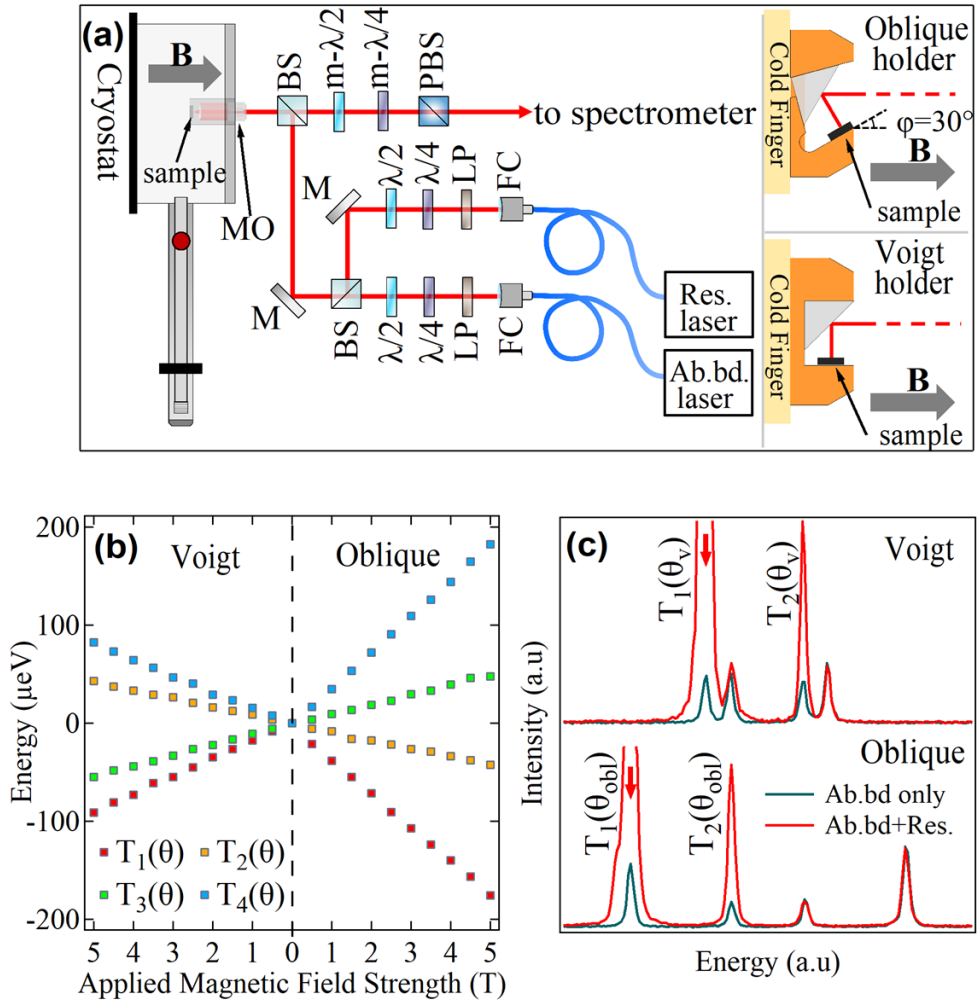

Figure 5.4: (a) Diagram of the experimental setup used for both the oblique and Voigt configurations. A machined sample holder and mirrored prism allows for the laser to access the sample while under a 60° and 90° orientation. (b) Level splitting of the QD as a function of magnetic field strength under Voigt (left) and 60° oblique (right) configuration. T_2 and T_3 exchange relative positions between configurations. (c) Confirmation of the exchanged positions in 5.4(b), resonant excitation on T_1 shows increased emission on either the third peak location ($T_2(\theta_V)$) or the adjacent second location ($T_2(\theta_{obl}$).

the lowest energy outer transition (T_1, left) it reveals the lambda-coupled T_2 inner transition. This is indicated by the increased emission due to spin pumping. Here the increased emission comes from either the adjacent (lowest energy) inner transition when $\theta_{obl} = 60°$, or at the highest energy inner transition when the magnetic field is

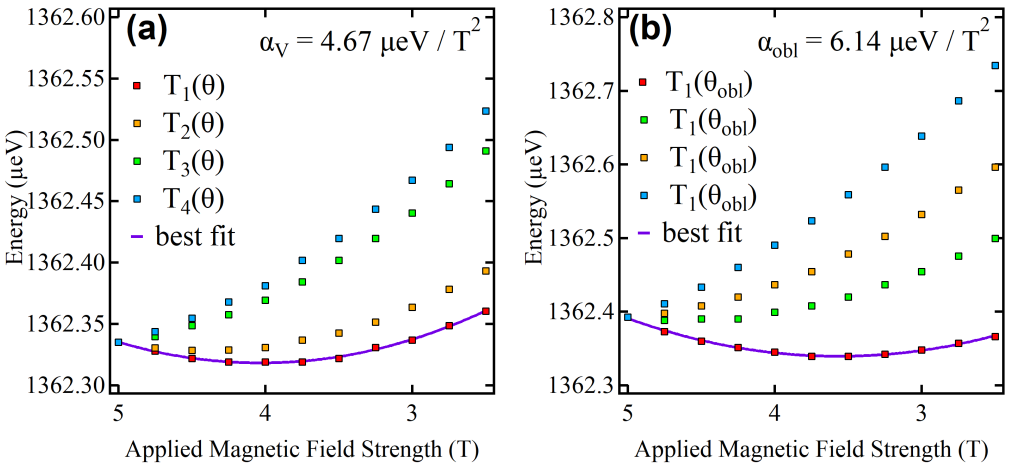

Figure 5.5: (a) Base Zeeman splitting of the QD as a function of the magnetic field strength under Voigt without the diamagnetic shift removed. The diamagnetic shift factor was $\alpha_V = 4.67\,\mu$eV / T^2 (b) Base Zeeman splitting similar to (a) under the Voigt configuration showing a diamagnetic shift factor of $\alpha_{obl} = 6.14\,\mu$eV / T^2. Purple line on each is a quadratic fit on the lowest energy state.

applied at $\theta_V = 90°$. These observations show that in both cases we are observing the same lambda-coupled pair (T_1, T_2). Yet due to the difference in ground and excited level splittings under each configuration, the emission energy is modified and the two inner transitions switch order energetically.

Polarization-resolved spectroscopy using QWP polarimetry is shown in figure 5.6(a) and (b) for the Voigt and oblique configurations respectively. The quarter-wave plate was rotated over 360 degrees with a 2 degree step and a complete spectrum of the photo-luminescence was acquired for each waveplate angle. A multi-Lorentzian peak fit is then used for each spectrum with a common background offset and linewidth for all four peaks. Using the fitted peak parameters, we calculate the overall intensity (peak area) of each transition for all QWP angles γ. This results in an intensity line profile $I_n(\gamma)$ where n $\in [1, 2, 3, 4]$ is the transition number from which the associated Stokes vector can be evaluated [121].

The QWP polarimetry of the Voigt configuration in figure 5.6(a) is indicative of a near unity value for the linear component S_1 and is expected in this geometry. Here, the co-polarized pairs are seen as the outer transitions (T_1, T_4) and the inner (T_2, T_3)

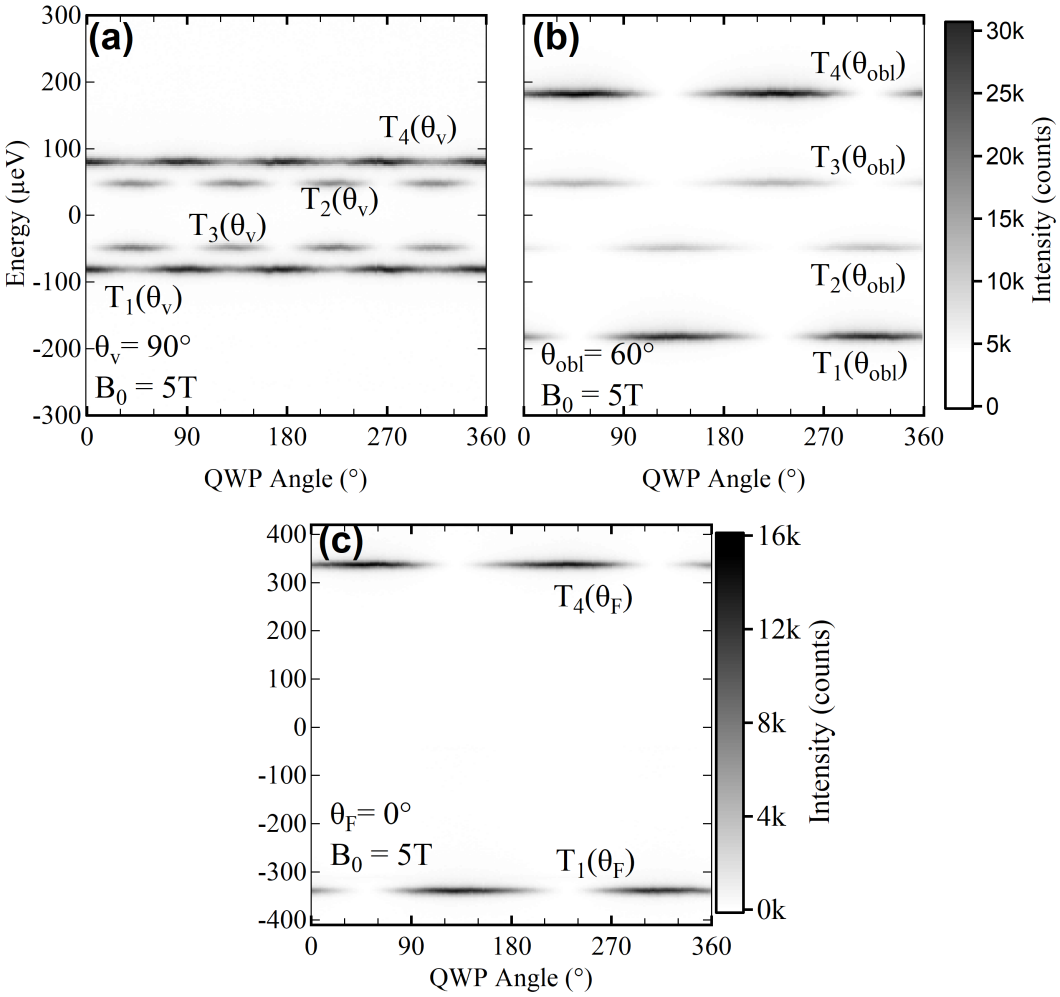

Figure 5.6: (a) QWP polarimetry of the charged QD in Voigt configuration. The intensity profiles vs QWP angle are indicative of highly linear emission. (b) QWP polarimetry of QD in oblique configuration. T_2 and T_3 show reduced intensities than the outer transitions in line with 5.6(b). (c) QWP Polarimetry of QD in Faraday configuration, only T_1 and T_4 remain optically active with circular polarization.

transitions by observing the similar intensity patterns as a function of QWP angle.

Conversely, figure 5.6(b) shows the oblique configurations profile this time indicating the co-polarized pairs are (T_1, T_2) and (T_3, T_4). This is influenced by the high degree of left and right circular polarization that dominates heavily at oblique angles as was shown in the simulated polarizations of figure 5.2(b). A comparison between the experimentally evaluated Stokes parameters and those calculated from the simu-

	S_1		S_2		S_3		Rel. Transition Strength	
	Sim.	*Exp.*	*Sim.*	*Exp.*	*Sim.*	*Exp.*	*Sim.*	*Exp.*
T_1	0.065	0.099 ±0.010	0	-0.001 ±0.004	0.998	0.995 ±0.001	1	1
T_2	-0.223	-0.204 ±0.001	0	0.001 ±0.004	0.975	-0.979 ±0.001	0.292	0.296
T_3	-0.223	-0.173 ±0.001	0	0.015 ± 0.004	-0.975	-0.985 ±0.001	0.292	0.286
T_4	0.065	0.129 ±0.008	0	0.016 ±0.005	-0.998	-0.991 ±0.001	1	1

Table 5.1: Table of simulated vs experimental results for Stokes parameters of target QD transitions with $\theta_{obl} = 60°$.

lations are found in table 5.1.

The circular S_3 components appear similar and the linear S_1 components show a small discrepancy compared to simulated values. The diagonal S_2 component is below 1.5% for all transitions which alongside some expected experimental error may contribute to the noted discrepancy. This aside, the overall behavior of the linear components is consistent in that the inner transitions exhibit a higher, shared degree of linearity. All four transitions showed a near unity degree of polarization evaluated as DOP = $\sqrt{S_1^2 + S_2^2 + S_3^2}/S_0$. The relative transitions strengths calculated by taking the ratio of S_0 for the inner transitions with respect to its corresponding outer transition also show a good agreement with the simulated value of 0.292.

Finally, figure 5.6(c) shows the QWP polarimetry under the Faraday configuration where we observe the two optically active outer transitions $\{|\uparrow\rangle_z, |\downarrow\rangle_z\}$. Each of these are the unmixed basis states under a Faraday magnetic field. Table 5.2 shows the Stokes parameters alongside the degree of polarization for the two active transitions.

	S_1 (*Exp.*)	S_2 (*Exp.*)	S_3 (*Exp.*)	*DOP* (*Exp.*)
T_1	-0.0101 ±0.0058	-0.0237 ±0.0269	-0.9994 ±0.0007	0.99973 ± 0.028
T_4	0.02196 ±0.120	0.0126 ±0.0013	0.9995 ±0.0003	0.99980 ±0.012

Table 5.2: Table of Stokes parameters of target QD transitions with $\theta_F = 0°$

Valence band mixing between the heavy- and light-hole branches can take place in highly deformed and strained quantum dots [37, 164]. The resultant state formed by valence band mixing can be written as,

$$|VBM\rangle = |\pm 3/2\rangle - \eta\,|\mp 1/2\rangle\,, \tag{5.8}$$

where $|\pm 3/2\rangle$ and $|\mp 1/2\rangle$ are the heavy and light-hole states respectively, and $\eta \in [0, 1]$ is a weighted hh-lh mixing factor with the lower limit being entirely heavy-hole and the upper limit entirely mixed. Upon recombination of a valence band mixed state with a ground state electron one would expect to observe elliptically polarized emission since the hole spins have opposite circularity. Valence band mixing is itself a property inherent to the QD and is independent of magnetic field so this ellipticity would be directly observable under a Faraday magnetic field [37, 142, 143].

The circular S_3 components in table 5.2 showed near-unity values of $T_1 = -0.994 \pm 0.0007$ and $T_2 = 0.995 \pm 0.003$, and a near-unity degree of polarization. From this we can infer the QD did not yield any significant valence band mixing. This then means the light-hole states can be safely neglected from the calculations discussed earlier in this chapter.

5.2.2 Spin Pumping in an Oblique Configuration

The fourfold splitting seen in oblique magnetic field implies a coupled-Λ structure should be in operation. From this assumption we identified the Λ-coupled pairs under the Voigt and oblique as in figure 5.4(c). Comparisons were made with the Voigt spin pumping profiles in figure 4.6(a)-(d) which has been extensively studied [131, 168]. A spin pumping process for each of the four available transitions was then performed as a function of the resonate laser detuning.

Figure 5.7(a)-(d) shows normalized photon emission count rates, detected at the energy depicted by the wavy downward arrows, as a function of the laser detuning as the excitation laser is resonantly swept across the transition. The count rate was

recorded either with (i) combined application of above-band and resonant excitation or (ii) only resonant excitation which allowed one to observe the spin pumping process and hint towards the initialization fidelity. In figure 5.7(a) it can be seen that resonantly driving the $|\downarrow\rangle_\theta \rightarrow |\uparrow\downarrow\Downarrow\rangle_\theta$ transition (solid upward arrow in inset) leads to population of the trion state followed by spontaneous decay into one of the two ground states. If the trion decays to the $|\downarrow\rangle_\theta$ state then the system is initialized to that state and a photon can be detected at the energy of the $|\uparrow\downarrow\Downarrow\rangle_\theta \rightarrow |\uparrow\rangle_\theta$ transition.

If the ground state is long lived with respect to the counting interval the system remains in this state and the resonant laser has no further effect. This leads to measuring only background counts for all resonant laser frequencies. Consequently, using weak above-band excitation enables reshuffling of the ground state such that the aforementioned process can occur repeatedly. This results in the clear Lorentzian spin pumping peaks observed. When spin pumping the system we set the resonant laser power to $P_{res} = 50$ nW and the polarization of the laser to linear to aid in cross-polarized detection. The weak above-band excitation was also linearly polarized and set to a power of $P_{Ab.bd.} = 6$ nW (approximately 1-1.5% of peak saturation power as from figure 5.3).

Despite the polarization of the resonant laser (linear) not matching the system under the oblique configuration ($\sim$98% circular) we are still able to drive the transition through the matching circular component of the resonant laser. This is because the linear polarization is a sum of cross-circular left- and right-polarized light.

Since the system emits under circular with a slight ellipticity cross-polarized reflectivity was limited in terms of suppressing the resonant laser light. Using the motorized intermediate slits of the custom spectrometer allowed further suppression of the resonant laser. Under a Voigt configuration the transitions are easily cross-polarized as resonant excitation with horizontally-polarized light will detect vertically-polarized light and vice versa. Instead, closing the intermediate slits on only the detected transition coupled with the less effective cross-polarized reflectivity resulted in good overall suppression.

The high contrast observed between randomizing the state using the above-band and without is a clear signature of a high fidelity initialization in the oblique con-

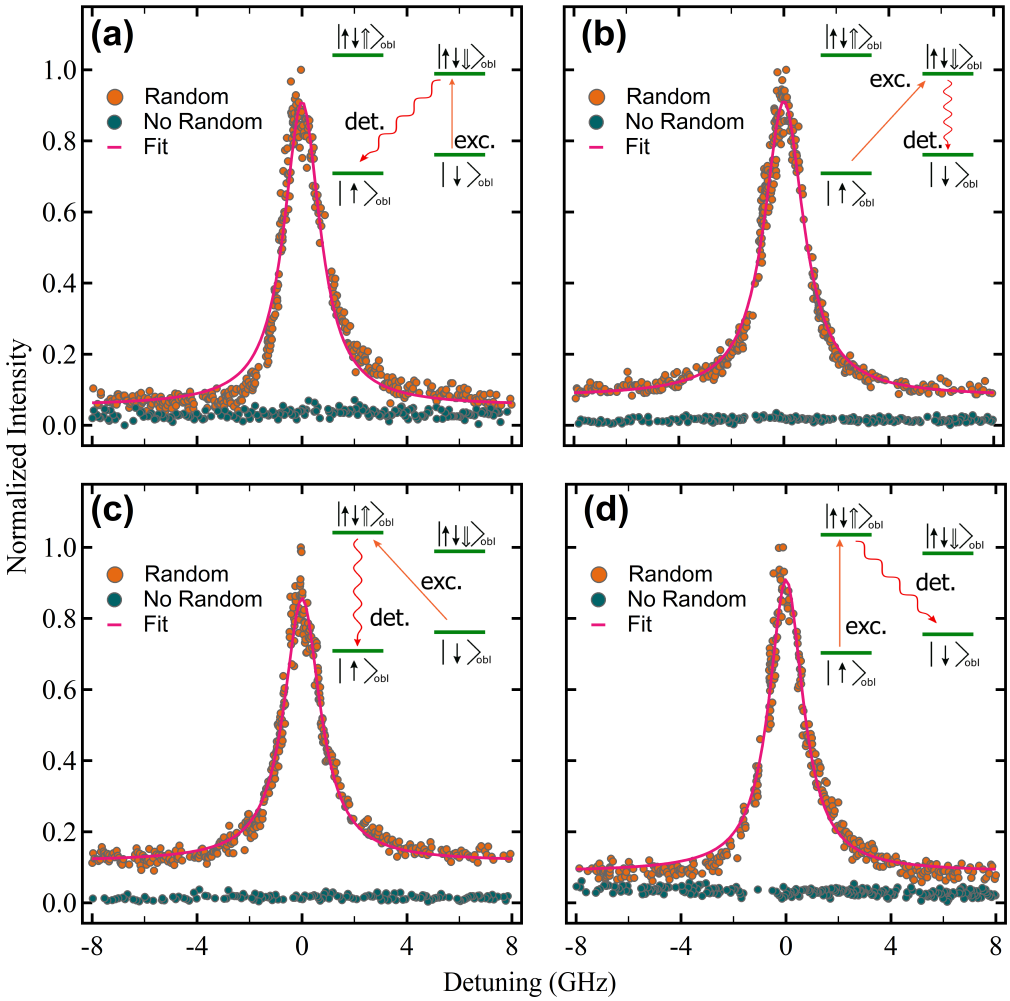

Figure 5.7: (a)-(d) Spin pumping of $T_1 - T_4$ as a function of excitation laser detuning under the Voigt configuration. Emission intensity vs single-photon counts shown with (i) randomization and (ii) no randomization applied. Solid line is Lorentzian best fit. Inset (top right) shows excitation and detection scheme for each.

figuration. The base background counts observed at the tail of the Lorentzian spin pumping peaks in figures 5.7(a) and (d) appear to lie significantly closer to the true background that is measured.

Recall that the relative transition strengths of the inner [5.7(a) and (d)] as opposed to the outer [5.7(b) and (c)] are shown to have an experimentally measured ratio of ~0.292 at $\theta_{obl} = 60°$ and $B_0 = 5$ T. As all other parameters in the experiment were

identical, using the same intensity for the above-band laser and resonant laser when driving all four transitions, the photo-luminescence counts due to this will be ∼3.4 times greater than that of the inner transitions. This conclusion appears consistent with respect to the results found in both the simulations and through experiment.

5.2.3 Considering Other Effects - Overhauser Shift

Upon the introduction of a tilted magnetic field, the measurements on the electronic ground state compositions and g-factors can be impacted by various factors resulting from the solid-state environment. Unlike many atomic systems quantum dots are both formed by and can interact with the many neighboring nuclear spins. Excitonic structures confined to a InGaAs quantum dot are predicted to neighbor approximately N $\sim 10^4$-10^5 nuclear spins at any time [40,41] each of which can give rise to interesting effects such as dynamic nuclear polarization and resultant Overhauser shifts [128,169].

In light of this, efforts were taken to investigate if these interactions played a role in the results discussed above or whether some other interesting phenomena could be observed. This section briefly discusses dynamic nuclear polarization and the Overhauser shift and methods used to verify there was no significant impact.

The negatively charged quantum dot confines two electron spins in a spin singlet state alongside a positively charged hole. The Fermi contact interaction, a magnetic interaction between electron spins and nuclei, requires a finite value of the Bloch wavefunction at the sites of the nuclei for interaction to occur [130]. As electrons exhibit a wavefunction with s-like symmetry they are susceptible to the interaction whereas the p-symmetric holes are not and can only interact via the much weaker dipole-dipole interaction [41].

Interactions between electrons and the nuclei can lead to spin flips through the hyperfine interaction. This results in the nuclei becoming polarized over timescales on the order of ms and longer if the process repeatedly occurs. If the process is not entirely random, such that the mean field effects do not average to zero, then the polarized nuclei can begin to exert a magnetic field known as the Overhauser shift on the quantum dot system.

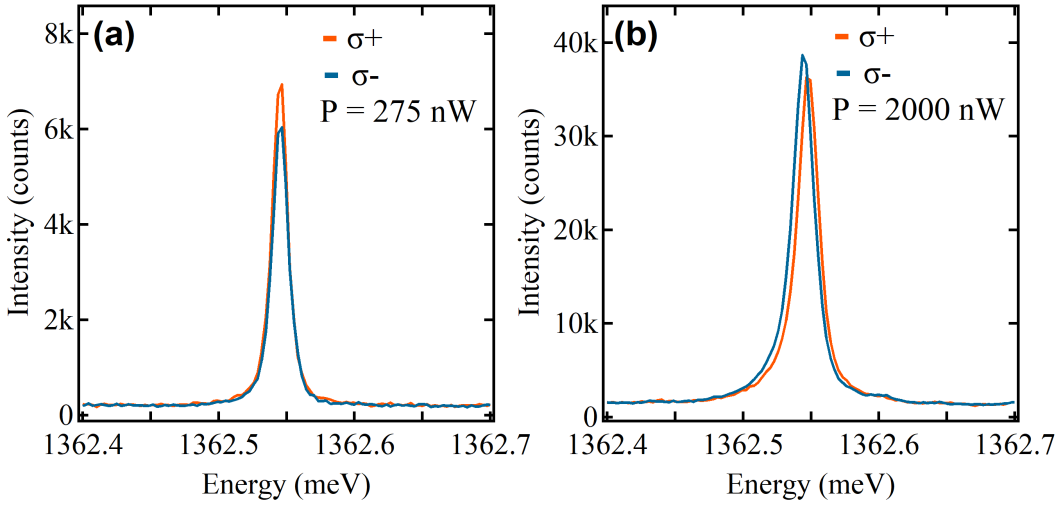

Figure 5.8: (a) Target QD at 0 T with above-band power set to 275 nW, excitation with $\sigma_{\pm}$. No notable shift is observed at low powers. (b) Same as (a) with strong driving of up to 2000 nW with above-band laser, a small yet notable shift is observed.

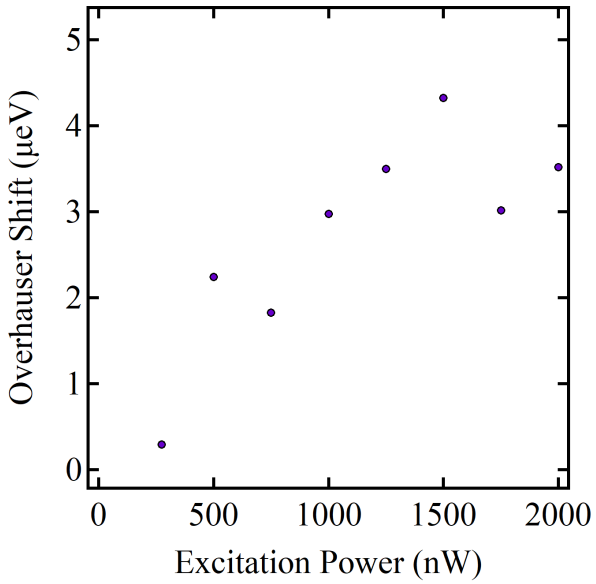

Figure 5.9: Overhauser shift measured as a function of above-band excitation power of the QD with no external magnetic field. Strong driving leads to an observable yet small shift of approximately 4 μeV when driving strongly.

To investigate whether this phenomenon had occurred with the QD discussed in this section measurements were taken as both a function of above-band lasers power

and polarization based upon methods in [128, 170]. Measurements were taken with the QD under zero magnetic field and $B_0 = 5$ T at $\theta_{obl} = 60°$ to identify if Overhauser shifts were present.

The hyperfine Hamiltonian is defined as,

$$\mathcal{H}_{hf} = v_0 \sum_j A^j |\psi(R_j)|^2 \left(I_z^j S_z + \frac{I_+^j S_- + I_-^j S_+}{2} \right), \tag{5.9}$$

where v_0 is the unit cell volume, A^j the hyperfine constant and $|\psi(R_j)|^2$ is the electron density at the jth nuclear site R_j [171]. The Hamiltonian consists of two terms of which the first term is proportional to the polarization of the electron and nuclei along an external magnetic field. The second term indicates the dynamic nuclear polarization where an electron's spin polarization in the quantum dot is transferred through an electron-nuclei spin flip process. Under excitation from a $\hat{\sigma}_\pm$ polarized above-band laser the polarization can then be transferred to the nuclei creating an Overhauser field that can either be aligned parallel or anti-parallel to the applied field which can be observed through photo-luminescence spectroscopy. This should be observable by driving the QD with opposite circularly polarized above-band excitation. If an Overhauser field is present we would anticipate a notable shift in the peak center.

Figure 5.8(a) shows the quantum dot under no external magnetic field at an excitation power of 275 nW. In figure 5.8(a) we see no observable shift at the powers used for the previous characterization experiments. Figure 5.8(b) again shows the system under no external magnetic field with the above-band power set to 2000 nW where the driving is strong. A small, yet notable shift of approximately 4 μeV is observed between the two excitation polarizations. Measurements were taken approximately every 250 nW from the 275 nW used in the previous experiments to 2000 nW shown in 5.8(b).

A Lorentzian peak was then fitted to detect the peak centers as a function of the above-band power and the Overhauser shift was then evaluated from the differences [128]. Figure 5.9 shows the results where we see a linear increase of the shift

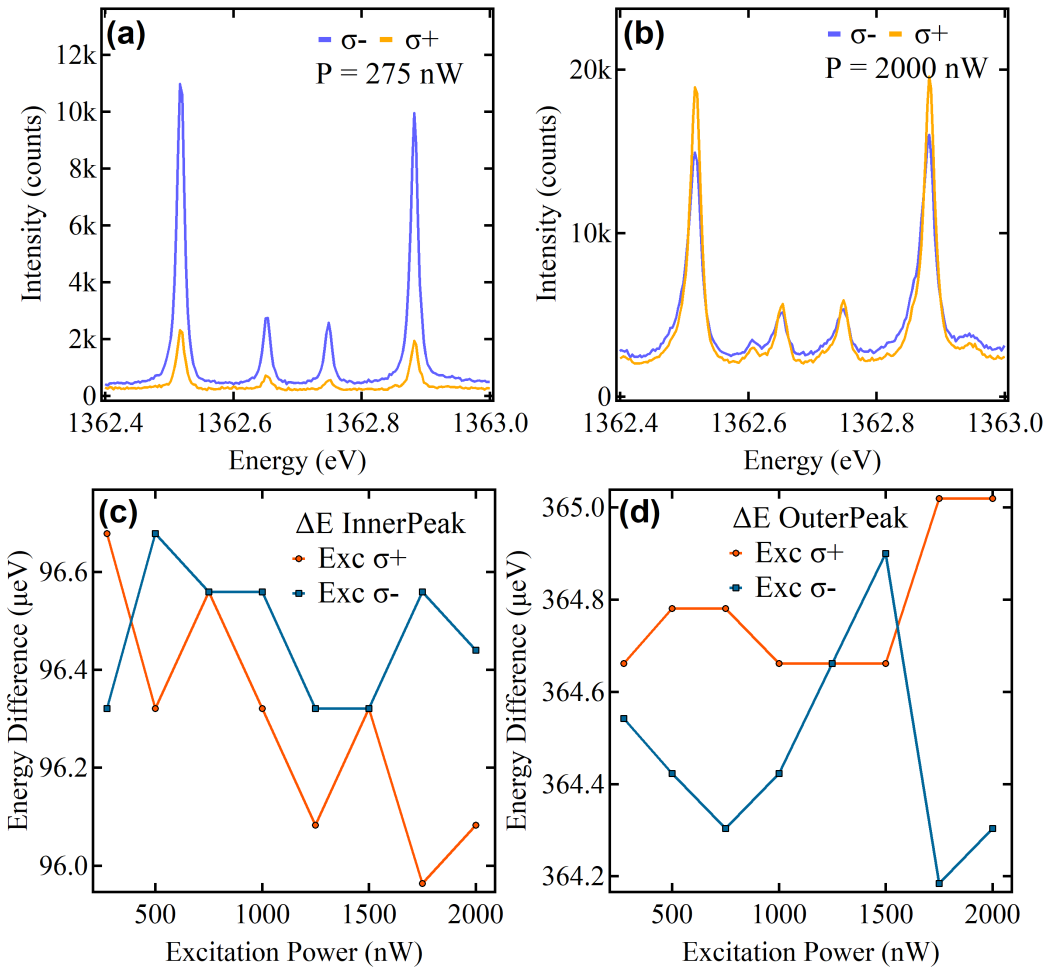

Figure 5.10: (a) QD under a 5 T magnetic field, driving with $\hat{\sigma}_{\pm}$ above-band, similar to 0 T no notable shift observed. (b) Same as (a) with 2000 nW above-band excitation. (c) Energy differences between the inner peaks under varying polarization of the above-band laser, the energy differences appear to show some correlation indicating no significant Overhauser shift. (d) Outer peak energy differences similar to (c), at strong driving of 2000 nW a small shift appears to occur but prior no clear observation of Overhauser shifts at 5 T.

up until approximately 1250 nW where a saturation effect appears to occur. The small Overhauser shift here indicates that the transfer of polarization to the neighboring nuclei is not significant for this particular quantum dot ensuring that measurements of g-factors and other system parameters were not affected directly.

This aside, previous works have observed shifts in similar samples ranging from

10-100's of μeV [128], most commonly this is seen under longitudinal (Faraday) magnetic fields. There have also been observations under transverse (Voigt) magnetic fields where it was predicted the Larmor precession of the electron spin around the external magnetic field should limit Overhauser shifts being present [172]. Due to the oblique magnetic fields there is then an increased chance of Overhauser shifts being present stimulating the measurements presented.

Measurements were again taken using the same process as figure 5.8 under a B_0 = 5 T magnetic field. This was to mimic the conditions used in the experiment. Figure 5.10(a) and (b) show the same process now at B_0 = 5 T for 275 and 2000 nW powers exciting the charged QD. Each of the four transitions had Lorentzian peaks fitted and the differences between the co-polarized pairs were evaluated to determine if there was an observable shift.

In figure 5.10(a) one may note a significant difference in emission intensity between σ^- and σ^+ excitation which may be perceived as indicative of more interesting phenomenon. Unfortunately, this effect was simply a result of having a different angle of the the output polarizer for the σ^+ measurements up until 750 nW. The data was taken from 250 nW to 2000 nW in 250 nW steps and the mistake was noticed and corrected from 1000 nW onward, although the lower power data was mistakenly not retaken. This is why the emission intensities are better matched in figure 5.10(b) as opposed to 5.10(a) and is nothing more than an artifact of a simple mistake when performing the experiment.

In figure 5.10(c) and (d) we see the observed energy differences which appear to show no correlated divergence as would be expected from a magnetic field generated from the neighboring nuclei. This may be a result of the 5 T field being significantly stronger than any hyperfine interactions present as well as the mixing of the configurations in which Larmor precession is then present.

The conclusions were then that while there is a small yet notable shift from the QD under zero external field, at the high magnetic field strengths at $\theta_{obl} = 60°$ we see no significant Overhauser shifts present. This section was included as a means to investigate and understand whether some rich physics under oblique fields could be

present. Although no significant results were observed the methodology was essential to ruling it out.

There are currently works that aim to take advantage of the dynamic nuclear polarization that is transferred from an electron spin to the neighboring nuclei in efforts to reach polarization rates of the nuclei of close to 100% [169, 173, 174]. The benefits of such works would help identify methods to minimize decoherence effects generated by the varying magnetic fields generated through interaction with the surrounding nuclei [175, 176].

5.3 Conclusion

In this chapter we demonstrated simulations and theory indicating oblique magnetic fields will generate unequal spin-state weightings of the ground and excited states in charged QDs. The particular focus was on the ground electronic states as coherent control, spin initialization and readout are conducted in this state space. We found that the excited trion states also exhibit similar behavior, although they will inevitably decay with rates on the order of 1 ns.

From experimental data gathered under both a Voigt $\theta_V = 90°$ and oblique $\theta_{obl} = 60°$, the charged QD selection rules under arbitrary magnetic field angles from 0 to 90° were found. These were then verified using QWP polarimetry with the experimental results showing a slight discrepancy in the linear polarization values of the inner transitions. Yet the ratio of the inner to outer states was shown to match the predictions well.

The characterization of self-assembled InGaAs quantum dots under oblique fields yielded a better understanding of the effect of tilted magnetic fields. These results can have applications towards samples grown in geometries that are not along the principal axes such as pyramidal 1-1-1 InGaAs quantum dots [54]. Due to the 1-1-1 geometry they will exhibit a strikingly similar behavior even under Faraday magnetic fields allowing knowledge transfer of these results to a broader research area.

Spin-pumping was then demonstrated under oblique fields indicating that fur-

ther coherent control experiments under oblique fields will be possible. Finally, an investigation into the presence of Overhauser shifts generated by dynamic nuclear polarization was presented. While the results proved insignificant for the experiments conducted here, the methodology was sound and acted as a further set of experiments to characterize the quantum dots behavior.

Chapter 6

Investigating Coherent Control under Oblique Magnetic Fields

The results shown in chapter 5 allowed for a deeper understanding of how self-assembled quantum dots work under oblique magnetic fields [115]. Such a characterization naturally allows for a range of further experiments based on the knowledge gained. In this chapter we look to test the properties of the QD spin-qubit state space under oblique field configurations. We will introduce various additional experimental methods for spin manipulation and further identification of the quantum states that make up the spin-qubit system.

Section 5.2 identified the contribution of multiple axial components of the g tensor result in greater level-splitting at reduced magnetic field strengths. This will naturally assist with extending coherence properties [126] and simultaneously lead to resolving the states more easily.

The selection rules, transition strengths and level structures quantified in section 5.1 have also been identified to show striking similarities with InGaAs quantum dots fabricated in a 1-1-1 pyramidal geometry [52–54,101]. Upon comparison of the charged excitons found in such samples under what would normally be considered a Faraday configuration (parallel to growth axis) they appear consistent with the results shown in the previous chapter.

Qualitatively, this can be understood to be a direct result of the pyramidal geom-

etry, a Faraday magnetic field with a 1-1-1 lattice plane would have no fixed axis to be taken with respect too. In self-assembled quantum dots the layers are vertically stacked and each layer lies in the x-y plane therefore a Faraday field is applied consistently throughout the sample. The 1-1-1 planes of pyramidal quantum dots will result in an oblique configuration in all directions and observation of a charged exciton here will show similar results as in section 5.1.

With a combination of the knowledge of coherent control under Voigt (as in chapter 4) and the understanding of the level structures in the oblique configuration (as in chapter 5), we now extend this through a series of experiments. That the double-Λ system, verified in the oblique spin-pumping demonstration, persists under oblique fields leads to the natural assumption that coherent control is possible. Yet the efficacy of such techniques warrants further investigation.

Hence, the format of this chapter is as follows; section 6.1 demonstrates rotations between the oblique ground states by means of coherent control experiments. Section 6.2 applies quantum state tomography which allows for the reconstruction of an initial system state. Here the experimental measurements are analyzed to recreate the initial density matrix $\hat{\rho}$. Finally, section 6.3 shows the results of an optically-induced geometric phase-gate in which an additional phase φ is imparted onto the spin-qubit. The result is a measurable change in the rate of equatorial precession around the Bloch sphere as seen in [136, 177].

6.1 SU(2) under oblique fields

We use the same quantum dot that was introduced in chapter 5 with a wavelength center of ~910.8 nm at B_0 = 0 T. The experimental setup for these are again similar to figure 4.4. This can be seen in figure 6.1 which shows the experimental spectra for the setup prior to producing the following results. The peak center of the rotation pulse is found at ~1362.1 meV equating to a detuning of ~400 GHz below the target QD.

Of each of the four available transitions we choose to observe the highest energy transition as the ratio of the inner/outer transitions was verified to be ~0.3 in section

5.2. As a result it is sensible to choose an outer transition exhibiting the dominant relative transition strength to increase the count rate and improve the signal to noise ratio.

Resonant excitation was performed on the adjacent coupled inner transition and cross-polarized reflectivity was implemented to minimize the back-reflected light. As the coupled transitions $T_3(\theta_{obl})$, $T_4(\theta_{obl})$ exhibit the same dominant circular polarization $S_3 \approx 0.99$ (table 5.1) this technique was considerably less effective than under the Voigt configuration. Additional measures involving careful alignment of the pinhole and taking advantage of the intermediate spectrometer slits, in conjunction with cross-polarized reflectivity, allowed for acquisition of acceptable data.

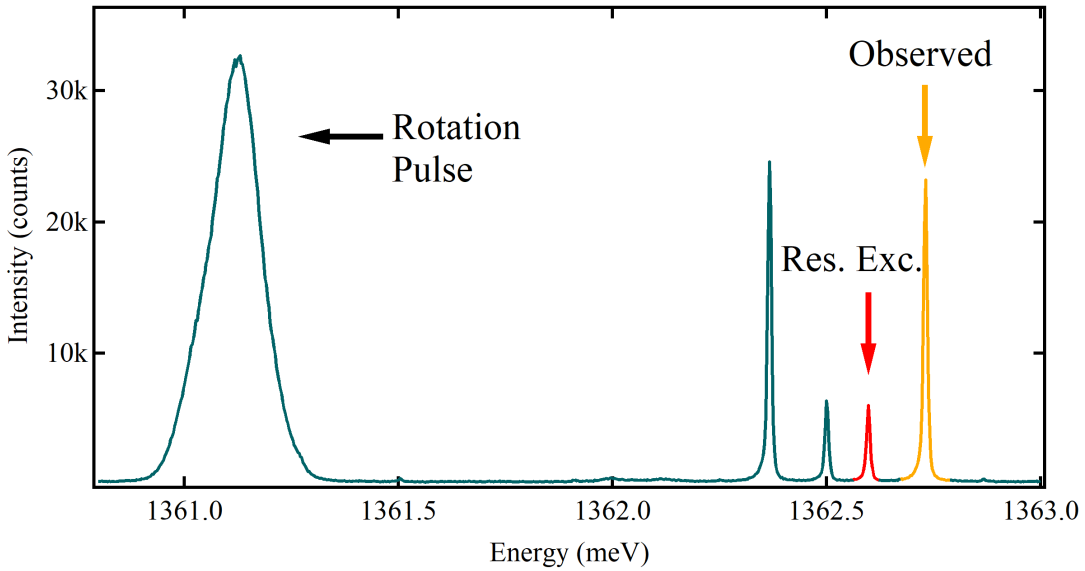

Figure 6.1: Experimental spectra of QD centered at ~1352.6 meV under oblique field configured for coherent control experiments at B_0 = 5 T and θ_{obl} = 60°. Highest energy (orange) transition is observed and the adjacent coupled inner transition (red) was resonantly addressed. Red-detuned rotation pulse on left with center ~1361.2 meV.

In figure 6.2(a) we see 4π of Rabi oscillations at $\theta_{obl} = 60°$ for both the fixed and variable arm of the delay stage. Since small variations inevitably exist in the path length and the beam path between each arm, careful alignment of both arms producing the good agreement in figure 6.2(a) were done. By ensuring, as best as possible, that the time-delayed pulses used in both Ramsey and SU(2) experiments are similar

the rotations performed should match the intuitive expectations. The pulse power for a π-pulse in this experiment was $P_\pi = 27.5$ mW and while there is a slight discrepancy in the count rate between the fixed and varied arm P_π looks to be equivalent within an expected experimental margin for error.

The polarization of the rotation pulse for these experiments was purely circular akin to the Voigt configuration. When the initial investigation of oblique field coherent control experiments began the author anticipated that the differing selection rules found in chapter 5 would result in the optimal rotation pulse polarization to be of an elliptical nature.

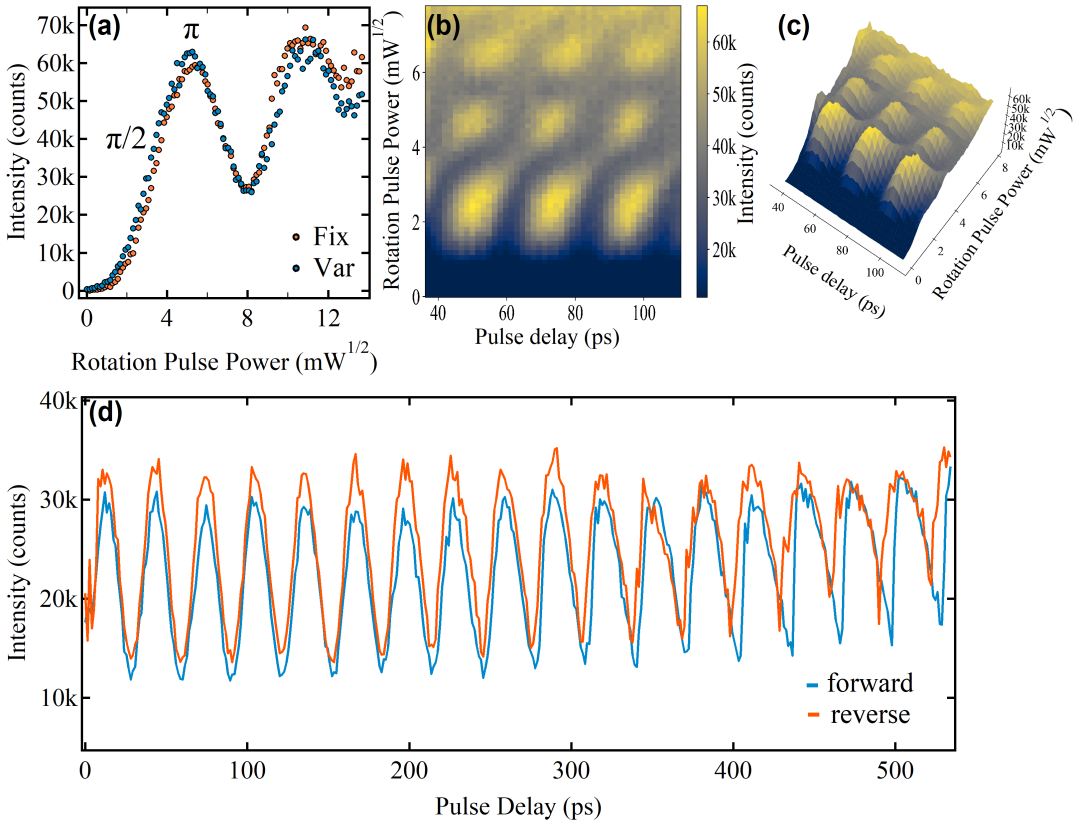

Figure 6.2: (a) Rabi oscillations using both fixed and variable delay arm showing good agreement. (b) Complete coherent control map of QD under oblique configuration. (c) 3d visualized complete coherent control map of (b). (d) Ramsey oscillations up to ~550 ps with the nuclear polarization sawtooth fringe pattern visible from ~450 ps.

Prior to the complete analysis in chapter 5 a series of Rabi oscillation measurements were performed as a function of the rotation pulse polarization to identify polarizations that optimize the frequency of oscillations. The result of these measurements were inconclusive and therefore are not presented in this work. Since then it has been confirmed that the optimal pulse polarization remains circular just as under the Voigt.

After the complete analysis of chapter 5, in particular the data from table 5.1, a calculation similar to 4.28 was performed using the numerically evaluated Stokes parameters. The Stokes vector for each transition was converted into an equivalent Jones vector (valid so long as the phase information is not over-interpreted) which contains information on the electric fields present in the problem. By numerically evaluating $\Omega^{\theta}_{\text{eff}}$ it was found that a $\hat{\sigma}_{\pm}$-polarized pulse remains the optimal pulse polarization at θ_{obl}.

With the system and setup aligned figure 6.2(b)-(c) show the SU(2) subspace map formed between $|\downarrow\rangle_{\text{obl}}$ and $|\uparrow\rangle_{\text{obl}}$. Measurements were taken as a multivariate function of the pulse power and pulse delay to generate the map. Additionally, a measurement was taken with only the rotation pulse active to generate an incoherent background map which can be subtracted to produce the figures shown. The pulse delay (x-axis) was varied from 35-120 ps to cover a little over three full Ramsey fringes.

A comparison between figure 4.9(c) (Voigt) and 6.2(b) (oblique) shows good agreement across both configurations. Under the oblique configuration there is a notable *smearing* effect (diagonally right) as we move from one high intensity peak to the peak diagonally adjacent. A possible experimental error causing this effect may be the alignment of the second time-delayed pulse as the motorized delay stage is translated. Minor variations in alignment and the beam level of the pulse may result in a variation of the second pulse incident on the quantum dot. This in turn will lead to small variations in the pulse power and possibly pulse shape that the quantum dot experiences.

Figure 6.2(d) shows Ramsey fringes over 500 ps of pulse delay taken in both the forward (0 ps $\rightarrow$ 500 ps) and reverse (500 ps $\rightarrow$ 0 ps) directions. At small pulse delays

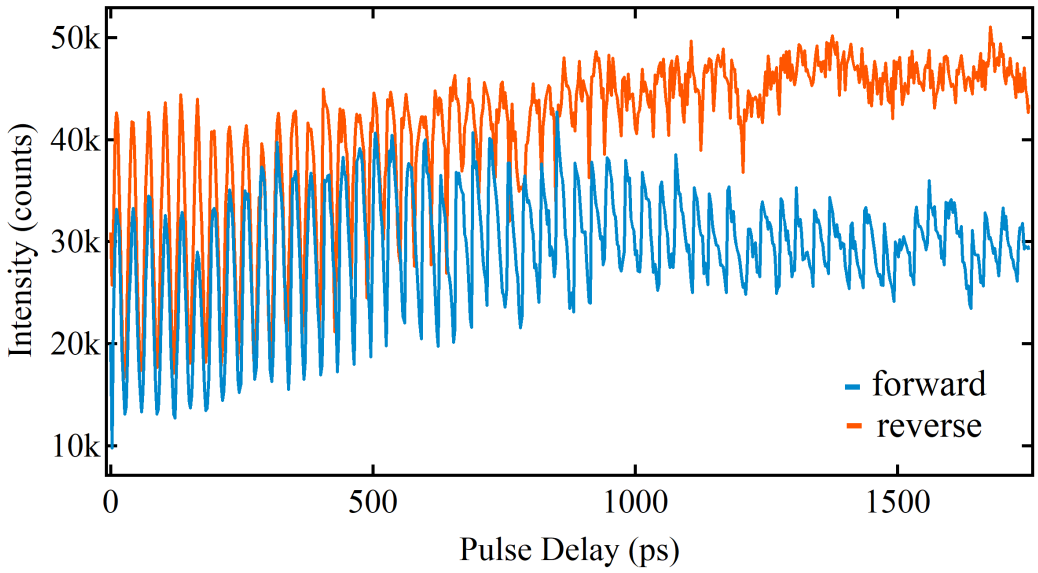

Figure 6.3: Ramsey oscillations over 2 ns of pulse delay with coherent oscillations visible but gaining a significantly reduced fringe contrast.

($\tau < 20$ ps) we see noise in the signal prior to the beginning of the Ramsey fringe which can be attributed to the pulse overlap between the first and second pulses. As both pulses derive from the same highly coherent laser source any pulse overlap that occurs results in constructive and destructive interference effects. When the pulse delay is great enough to temporally separate the pulses the Ramsey fringes become clearly visible.

At longer delays ($\tau > 400$ ps) we begin to see the nuclear polarization effect discussed in 4.3 and observed in figure 4.9(c). Upon further comparison we see that the fringe contrast in figure 6.2(d) across both directions is very similar to the Voigt configured data in chapter 4. This result is most likely from the quantum dot used here exhibiting nice coherence properties, but this can also be attributed to the improved understanding of experimental methods and techniques by the author when performing the measurements presented in this chapter.

Chapter 4 discussed that long Ramsey measurements are indicative of the long-lived coherence of the system due to larger predicted values of transverse relaxation rate T_2*. Again, direct measurement of T_2* would require a spin-echo sequence for

a reliable quantitative value. While these experiments could not be performed, the Ramsey measurements over a greater timescale still yields some indication of coherence properties of the quantum dot under an oblique configuration. Figure 6.3 shows forward and reversed Ramsey fringes over a 2 ns timescale showing clear oscillations until approximately 1250 ps. Here we see the combination of nuclear polarization and reduced fringe contrast as it begins to affect the data. The forward and reverse direction show a notable deviation in the average intensity. In particular, moving towards larger values up to 2 ns the difference in the average counts are separated by more than 10k.

To summarize, the results presented here show that even under oblique field configurations coherent control of the ground spin-states performs remarkably well. This appeared to be intuitively reasonable after observation of the coupled-Λ system under oblique fields in chapter 5. Regardless, it is important to be consistent and stay clear of assumptions by following with the experiment as done here.

For optical experiments that require strong magnetic fields to simply resolve the optical transitions this knowledge is welcome. Additionally, future fabrication processes containing lattice geometries that naturally introduce oblique fields, such as the pyramidal 1-1-1 QDs and other systems that may deviate from the simple axes, can directly apply this knowledge to research into those systems.

6.2 State tomographic reconstruction of single spin-qubit states

Section 6.1 confirmed that complete coherent control of the SU(2) subspace can be achieved efficiently even under oblique magnetic fields. This sections introduces the quantum state tomography (QST) method, a technique in which repeated measurements on an ensemble of states allows for a tomographic reconstruction of the original unknown quantum state. The reconstruction of the quantum system is generally formed by evaluating the input density operator $\hat{\rho}$. By finding the systems density operator full information of the system is said to be known.

Performing QST will allow for the density operator, defined as $\hat{\rho} = \sum_n c_n \left|\psi_n\right\rangle \left\langle\psi_n\right|$,

to be reconstructed. In this expression $|\psi_n\rangle$ are pure states of the system and c_n are their associated weights. The complete information specified by the density operator includes entanglement properties, environmental interactions causing decoherence/decay processes and knowledge of the systems overall populations and coherences. Therefore methods to determine $\hat{\rho}$ are relevant due to widespread applications in quantum information over a range of areas. To name a few there are single/multiple qubit systems [178–182], entanglement generation [183, 184], and more generally applications in quantum computation [10].

Here we show only *single qubit tomography* whereby readout of a complete set of measurements leads to identification of the initial input quantum state of the qubit. Single qubit tomography is but the first rung on a continuous ladder of quantum tomography techniques and is understood as the simplest to understand and implement.

More generally, quantum state tomography applies to multiple-qubit systems and there exists *quantum process tomography* (QPT) which can verify the efficacy of quantum operations [185]. In QPT rather than reconstructing the unknown density operator the efficacy of a quantum process or gate is instead measured. Single-qubit gates such an X- or Z-gate can be quantified and an associated fidelity of the operation can be found. Implementation of higher order quantum state/process tomography is considerably more challenging as the number of qubits scales. For an n-qubit state $2n$ detectors are required to project the n-qubit state into one of 2^n basis states [178].

Tomographic reconstruction of a single-qubit quantum state involves finding the location on the Bloch sphere equivalent to the initial quantum state. This requires measurement across three linearly independent, yet not necessarily orthogonal, bases which each narrow down the exact location. Each of the three basis states allows the unknown state to be narrowed down to a plane, a line and finally a point on the Bloch sphere [178].

This work was inspired by previous published research with a Si quantum dot device in [182]. The author observed the results which were then interpreted and translated into the optical control systems used in this work. From this the techniques

were then applied to the target QD under oblique fields.

6.2.1 Single-qubit tomography

The initial state of a single-qubit formed from the charged exciton ground states $\{|\downarrow\rangle_\theta, |\uparrow\rangle_\theta\}$ can be expressed using the density operator for the system. The density operator can be written in the basis of the Pauli spin operators $\{\hat{\sigma}_0, \hat{\sigma}_x, \hat{\sigma}_y, \hat{\sigma}_z\}$ and is defined as,

$$\hat{\rho} = w_0\hat{\sigma}_0 + w_x\hat{\sigma}_x + w_y\hat{\sigma}_y + w_z\hat{\sigma}_z. \tag{6.1}$$

Here, w_i are the associated weights of for each operator $\hat{\sigma}_i$, additionally we assume $w_0 = 1/2$ for a normalized density operator. In what follows the initially prepared states were the two states $|Z\rangle_{\text{init}} = |\downarrow\rangle$ and $|Y\rangle_{\text{init}} = (|\downarrow\rangle + i\,|\uparrow\rangle)/\sqrt{2}$ through which the analysis should allow reconstruction of their associated density operators $\hat{\rho}_Z$ and $\hat{\rho}_Y$.

The three Pauli spin operators $\hat{\sigma}_x, \hat{\sigma}_y, \hat{\sigma}_z$ represent the three linearly independent bases in which the system was measured. As we shall see a series of experimental measurements along each of these bases can allow one to evaluate the probabilities $P_x(t), P_y(t), P_z(t)$. It is from these probabilities that a numerical evaluation of the datasets allows a reconstruction of $\hat{\rho}(\tau = 0)$.

The experimental setup is similar to figure 6.1 and only the state initialization and pulse sequence are altered to acquire the relevant data for analysis. The experiments were performed at $B_0 = 5$ T and $B_\theta = 60°$, and each initial state was prepared prior to a readout scheme that measures the probabilities $P_x(t), P_y(t), P_z(t)$. The probabilities are proportional to the weights w_x, w_y, w_z of equation 6.1 after scaling and normalizing the data measured in these experiments. This conversion to probabilities was introduced to aid in the data analysis following the method in [181]. Although we should note that as it is impossible to fully account for the background counts not associated with the QD they must be interpreted cautiously as discussed further in the chapter. The probabilities are then related to a time-dependent evolution yielded from the data when measured using time-separated pulses from the delay stage.

To initialize the state into $|Z\rangle_{\text{init}}$, the $|\uparrow\rangle \rightarrow |\uparrow\downarrow\Uparrow\rangle$ transition is resonantly addressed to populate $|Z\rangle_{\text{init}} = |\downarrow\rangle$ within several nanoseconds. Initialization of state $|Y\rangle_{\text{init}}$ was performed with an initial $\pi/2$ pulse with the intention of preparing the coherent superposition state $|Y\rangle_{\text{init}} = (|\downarrow\rangle + i\,|\uparrow\rangle)/\sqrt{2}$.

Each prepared state was measured in each basis as a function of pulse delay and is shown in figure 6.4(a)-(c). The blue and red data points correspond to an initial state of $|Z\rangle_{\text{init}}$ and $|Y\rangle_{\text{init}}$ respectively. The count rates of each measurement in figure 6.4(a)-(c) are related to the probabilities by (a) P_x, (b) P_y, (c) P_z.

In figure 6.4(a) photon count rates as a function of pulse delay measures in the $\hat{\sigma}_x$ basis with a pulse sequence as seen in the inset. After initial state preparation, application of a $\pi/2$ pulse yields a click (no-click) dependent upon the state projecting on to $|\uparrow\rangle$ or $|\downarrow\rangle$ state respectively.

Figure 6.4(b) shows measurement in the $\hat{\sigma}_y$ basis with the pulse sequence visible in the inset. The process is analogous to (a) with an additional offset $Y_{\text{offset}} = 24$ ps introduced which yields an accumulated phase of $\varphi = \pi/2$ after the state precesses at the Larmor frequency ω_{larmor}. Projection with the second pulse and the Y_{offset} yields a count rate related to $\hat{\sigma}_y$.

The final measurement in the $\hat{\sigma}_z$ basis is shown in figure 6.4(c) again with the pulse sequence in the inset. To detect this, the power of the pulse is set to 2π (as opposed to the previous $\pi/2$ pulses) and the count rate is measured on the detector.

Measurements in all three linearly independent bases yields a complete set of data with the required information to reconstruct the associated density operators $\hat{\rho}_Z$ and $\hat{\rho}_Y$. Figure 6.5(a)-(c) are the same data re-scaled and normalized to express the counts in terms of probabilities ($P_i \in (0, 1)$). Using the weights that are calculated $(\omega_x, \omega_y, \omega_z)$ we are then able to evaluate the steady state density matrix $\hat{\rho}(\tau = 0)$.

The re-scaling and normalization is essential for converting count rates to measurable probabilities and were evaluated by implementing knowledge gained from other works using NV centers in diamond [181] and Si based QD-devices [182]. The count rate is then expressed in terms of probabilities that can then be used directly to evaluate w_i. Each weight can then be determined from the experimentally measured count

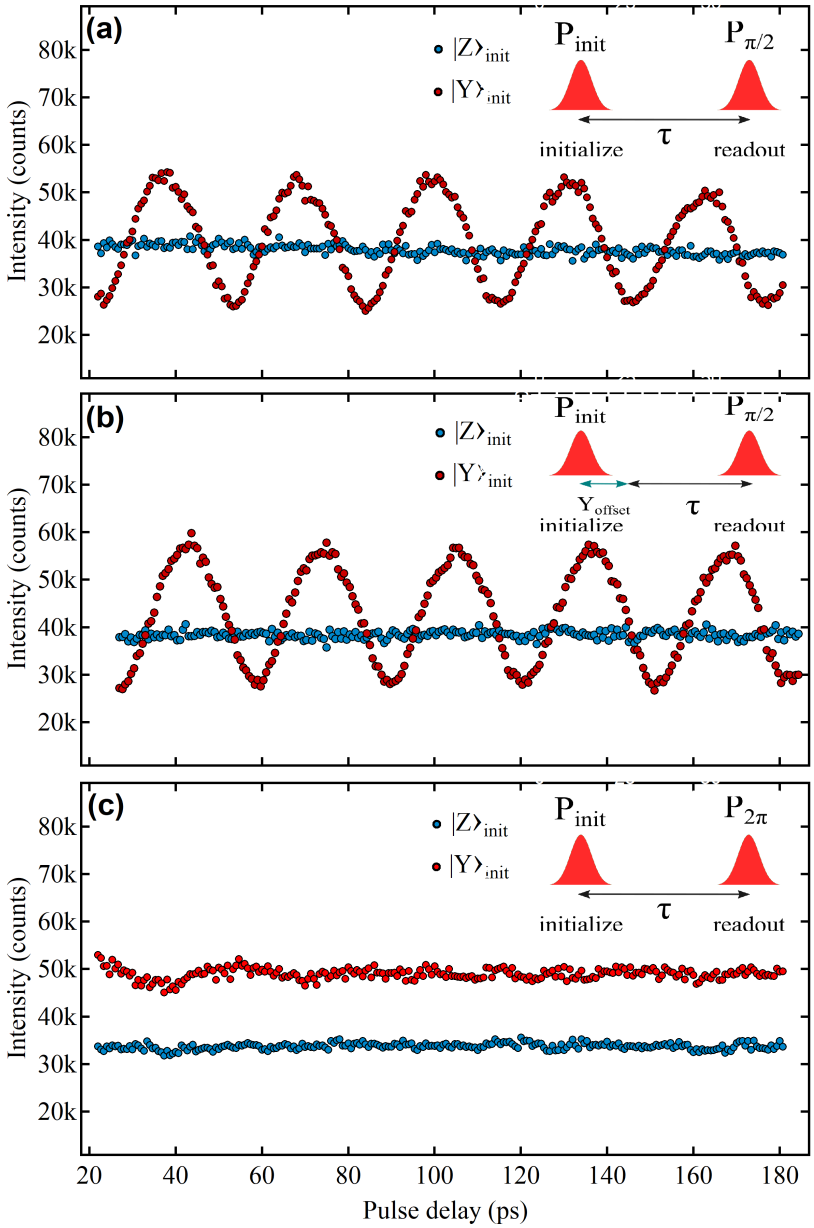

Figure 6.4: (a) Measurement of the output state after projection on the $\hat{\sigma}_x$ basis. The inset shows the pulse sequence used. (b) Output state counts after projection onto the $\hat{\sigma}_y$ basis and associated sequence in the inset. (c) Output state counts after projection onto the $\hat{\sigma}_z$ basis and associated sequence in the inset.

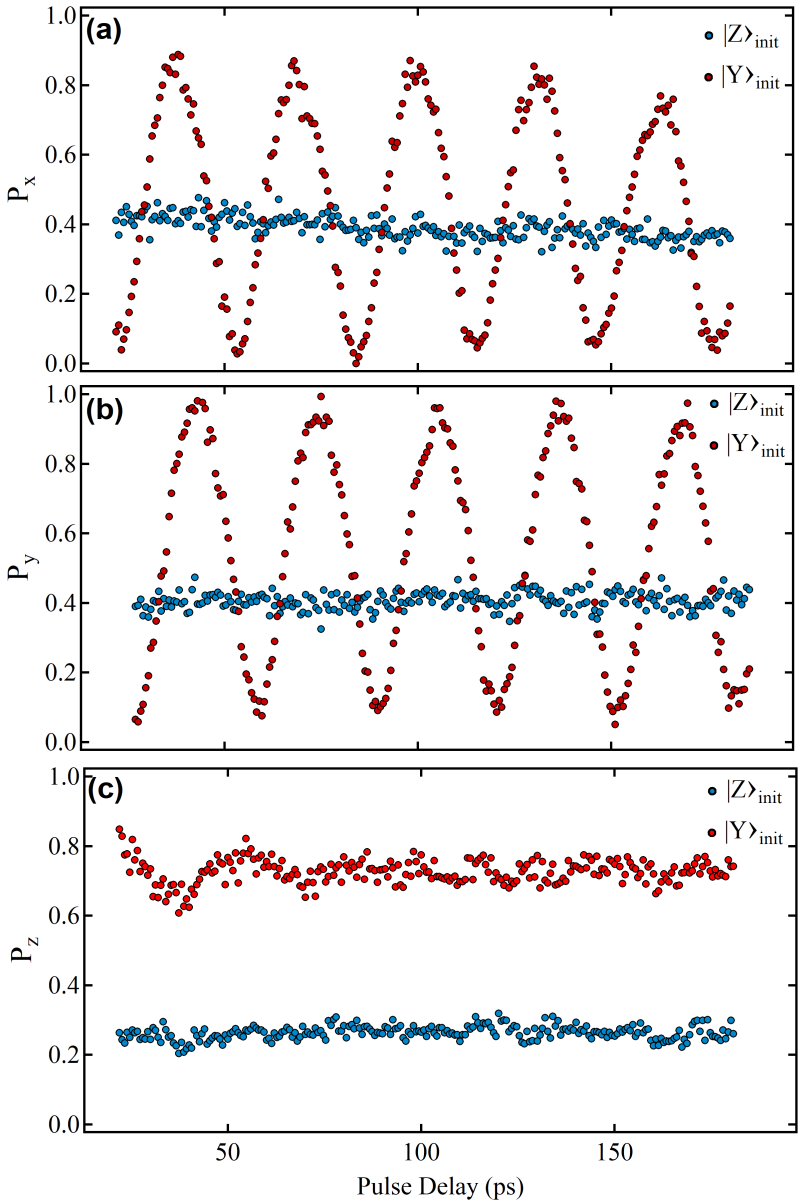

Figure 6.5: (a) Populations P_x for $|Z\rangle_{\text{init}}$ (blue) and $|Y\rangle_{\text{init}}$ (red) after projection onto $\hat{\sigma}_x$. (b) Populations P_x for $|Z\rangle_{\text{init}}$ (blue) and $|Y\rangle_{\text{init}}$ (red) after projection onto $\hat{\sigma}_y$. (c) Populations P_x for $|Z\rangle_{\text{init}}$ (blue) and $|Y\rangle_{\text{init}}$ (red) after projection onto $\hat{\sigma}_z$. Experimental error is clear as we would anticipate (red) to be centered at 1 and (blue) centered at 0.

rate c using [181],

$$\begin{aligned} \omega_x &= 1/2 - (c_y - c_{\text{min}})/\delta, \\ \omega_y &= (c_x - c_{\text{min}})/\delta - 1/2, \\ \omega_z &= (c_z - c_{\text{min}})/\delta - 1/2, \end{aligned} \tag{6.2}$$

where $\delta = c_{\text{max}} - c_{\text{min}}$ is the contrast between the counts. We take a moment here to state that any QST/QPT measurement scheme that detects photons as a form of measurement has a common problem. Determining the true determination of the photon count rate is in essence extremely difficult to achieve and so introduces error into the evaluation of both the density operator and associated fidelity. Hence, these values should be interpreted with some caution unless the experiment is optimized to account for this.

Using the contrast term δ we can then re-scale figure 6.4 to reflect the populations of the state projections as shown in figure 6.5(a)-(c). We may now begin to interpret the results in a more quantitative manner. Figure 6.5(c) indicates some systematic errors were present during the experiment.

From the red data points $|Y\rangle_{\text{init}}$, we observe an average value $\bar{P}_y^{\text{exp}} \approx 0.8$ whereas for a completely pure quantum state we would anticipate $\bar{P}_y^{\text{ideal}} = 0.5$. For the blue data points $|Z\rangle_{\text{init}}$, the average probability is $\bar{P}_z^{\text{exp}} \approx 0.2$ as opposed to $\bar{P}_z^{\text{ideal}} = 0$. Further analysis revealed the identity of the true initial state $|Y\rangle_{\text{init}}$, to confirm that the preparation was far from the idealized state. Regardless, this highlights the benefits of implementing a QST procedure, the *actual* prepared state can be identified as opposed to the *ideal* state that was intended in this case.

Using the experimental results of figures 6.4 and 6.5 alongside 6.1 and 6.2 we are then able to reconstruct the density operators $\hat{\rho}_Z$ and $\hat{\rho}_Y$. In total 240 measurements were performed over a pulse delay with a range of 20-180 ps. Each data point is essentially analogous to a time-evolved density operator $\hat{\rho}(\tau)$. By evaluating $\hat{\rho}(\tau)$ for each point in time we gain a large number of statistical measurements that can then be averaged over to reconstruct the initial density operator $\hat{\rho}(\tau = 0)$ for each input state.

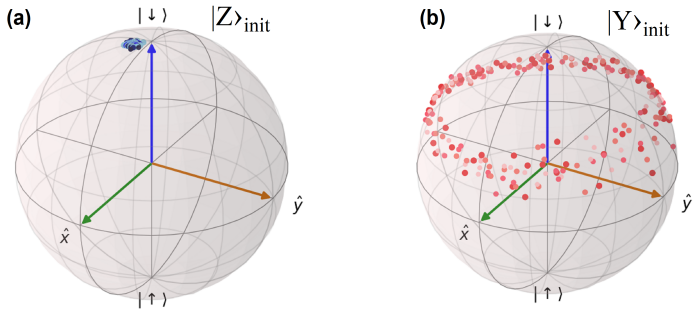

Figure 6.6: (a) State tomographic results of $|Z\rangle_{\text{init}}$ analyzed from (blue) data in figure 6.5. (b) Results of $|Y\rangle_{\text{init}}$ analyzed from (red) data in figure 6.5. The data lies off of the equator due to a poor initialization fidelity.

Upon evaluation we find the density operators $\hat{\rho}_Z$ and $\hat{\rho}_Y$ recreated using QST procedure to be,

$$\hat{\rho}_Z = \begin{pmatrix} 0.905 & 0.076 + i0.090 \\ 0.076 - i0.090 & 0.095 \end{pmatrix}, \tag{6.3}$$

$$\hat{\rho}_Y = \begin{pmatrix} 0.724 & -0.055 + i0.042 \\ -0.055 - i0.042 & 0.276 \end{pmatrix}. \tag{6.4}$$

With any density operator the diagonal elements ρ_{ii} are interpreted as the populations which take on only real values and should sum to 1, the off-diagonal elements ρ_{ij} $(i \neq j)$ are complex-valued and are interpreted as the system coherences.

From $w_i\hat{\sigma}_i$ we can visualize the initial states $|Z\rangle_{\text{init}}$ and $|Y\rangle_{\text{init}}$ on the Bloch sphere, as shown in figure 6.6. The data points for $|Z\rangle_{\text{init}}$, visible in (a), show a highly localized position at the ground state $|\downarrow\rangle$ with little spread. This, coupled with the slight offset from the pole demonstrates there is high precision in state initialization with a small systematic error. Overall there is good agreement with the intended initial state showing spin initialization is both a consistent and reliable technique.

Figure 6.6(b) shows $|Y\rangle_{\text{init}}$ for each data point and can be seen to precess around the azimuthal axis due to the time evolution of $\hat{\rho}_Y(\tau)$ induced by the pulse delay. From this visualization we can can clearly identify that the system was not prepared in an equally weighted superposition state.

As seen in the inset of figure 6.4(b) $|Y\rangle_{\text{init}}$ was initially prepared using a $\pi/2$ pulse, although upon analysis of the data this has proven not to be the case. Using the weights w_x, w_y, w_z we find the pulse applied in the experiment equated to a rotation 60.9° in the polar axis from $|\downarrow\rangle$. From this we find that the actual pulse area of the experiment was instead very close to a $\pi/3$ pulse which would recreate the state shown on the Bloch sphere.

The rank of density operator scales with the number of qubits and so in the multiple qubit case the Bloch sphere is no longer suitable to interpret the data. Instead, an alternative visualization of the unknown system state is through the elements of the density operator and is shown for both states in figure 6.7. Figure 6.7(a) and (c) show the real components while (b) and (d) show the imaginary components for $|Z\rangle_{\text{init}}$ ((a) Re (b) Im) and $|Y\rangle_{\text{init}}$ ((c) Re (d) Im), respectively. The system is shown in the basis $\{|\downarrow\rangle, |\uparrow\rangle\}$ and so the real diagonal elements are interpreted as the populations associated with the initial state and matches the data presented in figure 6.6.

As a final step, and a key benefit of QST/QPT, the fidelity of either the initialized unknown state or the efficacy of a quantum operation can be quantified by comparing the experimentally observed $\hat{\rho}_{\text{exp}}$ with the idealized density operator $\hat{\rho}_{\text{ideal}}$. The fidelity is found using [181, 186],

$$\mathcal{F} = \frac{\text{Tr}\{\hat{\rho}_{\text{ideal}}\hat{\rho}_{\text{exp}}\}}{\sqrt{\text{Tr}\{\hat{\rho}_{\text{ideal}}\hat{\rho}_{\text{ideal}}\}\text{Tr}\{\hat{\rho}_{\text{exp}}\hat{\rho}_{\text{exp}}\}}}, \tag{6.5}$$

and when applied to both states reveals a fidelity and associated error ($\varepsilon = 1 - \mathcal{F}$) of,

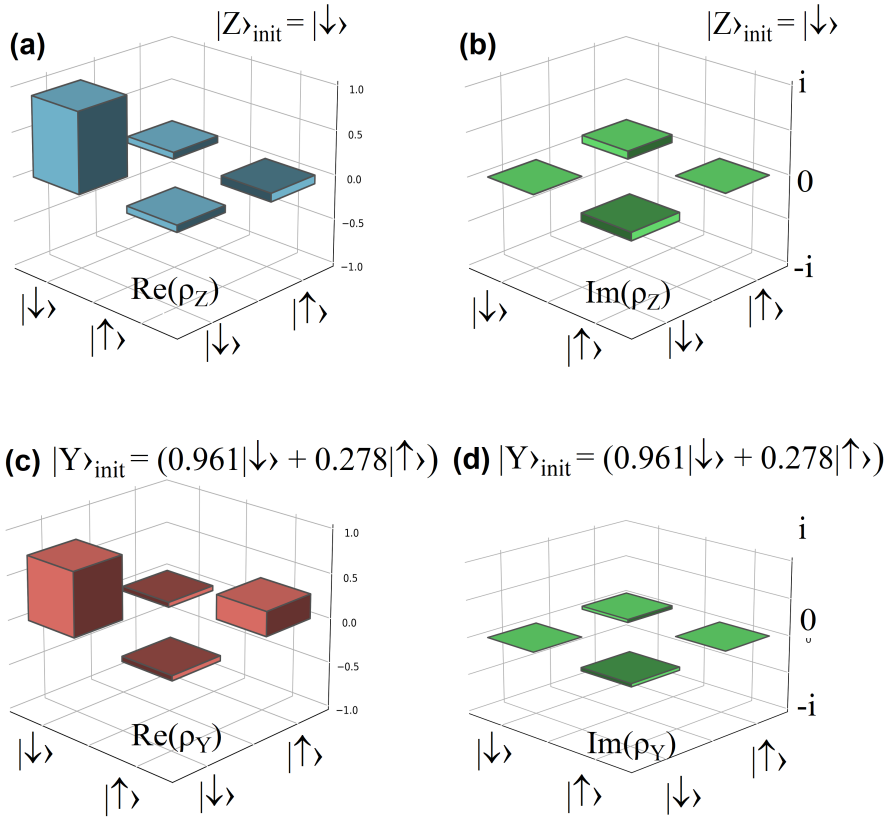

Figure 6.7: (a) Real component of the $|Z\rangle_{\text{init}}$ density matrix, $\hat{\rho}_Z$, recreated from (blue) data in figure 6.5. (b) Imaginary component of $\hat{\rho}_Z$. (c) Real component of the $|Y\rangle_{\text{init}}$ density matrix, $\hat{\rho}_Y$, recreated from (red) data in figure 6.5. (d) Imaginary component of $\hat{\rho}_Y$.

$$\mathcal{F}_Z = 0.978 \qquad \varepsilon_Z = 0.022, \tag{6.6}$$

$$\mathcal{F}_Y = 0.694 \qquad \varepsilon_Y = 0.306. \tag{6.7}$$

From 6.6 ($\mathcal{F}_Z$) we can see that the initialization of the spin pumping procedure even under oblique fields works remarkably well and with more of a focus improve-

ment this should approach near unity values [126,187]. The fidelity of 6.7 ($\mathcal{F}_Y$) shows a large deviation from the ideal state $|Y\rangle_{\text{init}}$ with an error of 30.6%. As highlighted previously this was anticipated from the data yet was not intentional. The cause for such a large error is most likely attributed to experimental error introduced by the author when identifying the $\pi/2$ rotation pulse power which instead was a $\pi/3$ pulse. Even so, the implementation of single-qubit QST revealed an accurate determination of the actual state that was prepared, which shows the strengths of the QST method.

In conclusion, we have shown quantum state tomography techniques applied to a charged quantum dot under an oblique magnetic field. We found high fidelities are possible when preparing an initial quantum state and with a more focused approach these values can be improved significantly. Further works would benefit by taking additional steps towards quantum process tomography to evaluate the efficacy of a range of quantum operations possible on spin-qubits. Common processes to evaluate on a single spin-qubits are X- and Z-gates or rotations, while more complex gates between entangled spin-qubits such as CNOT and SWAP gates are also potential candidates.

This is of course conditional upon having sufficient equipment, time and resources to dedicate towards. The datasets required must be large enough to allow for statistical averaging, for an n-qubit system the number of detectors required scales as $2n$ and the number of linearly independent basis states as 2^n.

6.3 Geometric phase gate and dressed states

Section 6.1 and 6.2 demonstrated that control over the spin-qubit under oblique fields is remarkably consistent with the Voigt configuration. We saw that the target QD demonstrates Rabi oscillations and Ramsey fringes with a coherence maintained for almost 2 ns without the inclusion of a spin-echo sequence to enhance it.

The rate of precession due to the Larmor frequency ω_{larmor} is related to the ground state splitting induced by the applied magnetic field. Varying strong magnetic fields is a slow and laborious process and to vary them on timescales relevant to QD spin-

qubits (ps-μs) is impractical and often times impossible.

The polar angle of the Bloch sphere can be easily manipulated, with a rotation angle θ possible through varying the pulse power that is applied over the short, picosecond width of the optical pulse. Additionally more complex and precise pulse powers and timings are possible with the inclusion of additional modulation equipment (AOM/EOM).

Since magnetic fields can only be slowly varied, techniques that instead use electric fields as a means to control the rate of the azimuthal axis is desirable. To this end, we introduce experiments that confirm that through application of a strong resonant driving field the azimuthal frequency of oscillation φ can be altered by imparting a *geometric phase* onto the qubit system, even under oblique field configurations.

The geometric phase introduced in this section stems from what is commonly known as either the *Pancharatnam* or *Berry* phase [188, 189], named after those who first described the effect. In a QD system this is in principal observed through resonant driving to dress the system states. This will generate a set of new eigenstates that develop a time-dependent evolution of their relative phase. In what follows we demonstrate the relative phase can be imparted onto the ground state spin-qubit, allowing methods to vary the precession rate around the azimuthal axis using electric fields.

The diagram in figure 6.8(a) describes how to observe this effect, by driving the $|\uparrow\rangle \rightarrow |\uparrow\downarrow\Uparrow\rangle$ transition using an electric field with a large Rabi frequency Ω_{drive} new system eigenstates are generated. These dressed states $|+\rangle, |-\rangle$ are (anti-)symmetric combinations of the ground and excited trion state written as [190],

$$\begin{aligned} |+\rangle &= |\uparrow\rangle + |\uparrow\downarrow\Uparrow\rangle\,, \\ |-\rangle &= |\uparrow\rangle - |\uparrow\downarrow\Uparrow\rangle\,. \end{aligned} \tag{6.8}$$

Equation 6.8 refers to the dressed states of the system with the state $|+\rangle$ taken to be the higher energy state by convention. The new states formed can then accumulate a drive induced time-dependent phase $\varphi = i\Omega_{\text{drive}}t$ resulting in the state $|\psi(t)\rangle =$

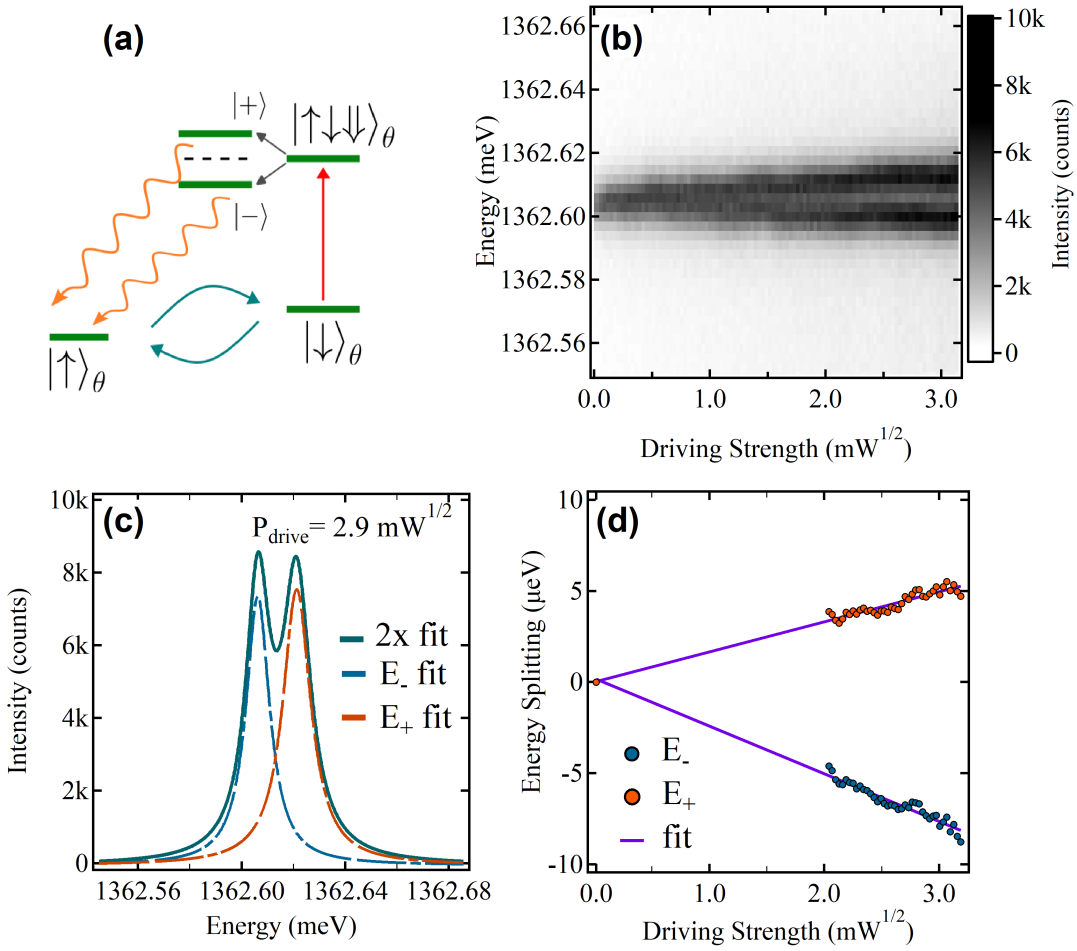

Figure 6.8: (a) Diagram of the oblique double-Λ system under a strong resonant driving field on the $|\uparrow\rangle \rightarrow |\uparrow\downarrow\Uparrow\rangle$ transition which will dress the states. (b) Measured dressed state splitting of the (orange) cross-transition in (a) as a function of the driving field strength. (c) Lorentzian fits of the experimental spectra at $P_{\text{drive}} = 2.9\,\text{mW}^{1/2}$, single Lorentzian fit to the $|\pm\rangle$ dressed state. (d) Energy level splitting as a function of driving field strength with best fit line for $E_{\pm}$, splitting could only be resolved at $\sim 8\mu$eV which aligns well with the measured resolution of the custom-built spectrometer.

$|+\rangle + e^{\varphi(t)}\,|-\rangle$. From figure 6.8(a) we see that there exist new pathways in which the ground state spin-qubit can be coupled by the adiabatically eliminated trion state.

The experimental setup was again similar to 6.1 with the control variable to observe the dressed states the power of the CW laser resonant on a transition at $B_\theta = 60°$ and $B_0 = 5$ T. Figure 6.8(b) shows experimental spectra of the (orange) transition as a function of the resonant driving strength. This clearly demonstrates the new eigen-

states formed from the $|\uparrow\rangle \rightarrow |\uparrow\downarrow\Uparrow\rangle$ transition. Clear observation of the level splitting is visible from $P_{\text{drive}} > 1$ mW$^{1/2}$ and we will find an applied fit to the splitting was possible at values greater than 2 mW$^{1/2}$.

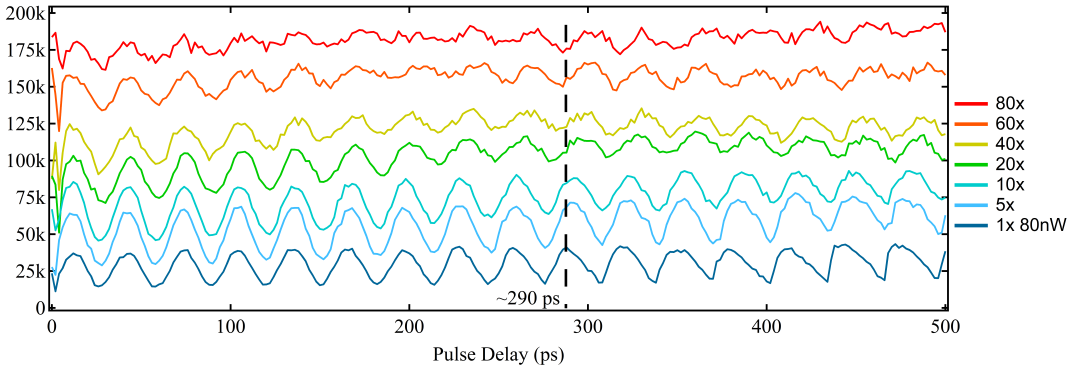

Figure 6.9: Waterfall plot of Ramsey fringe data as a function of driving field strength from 1x (80 nW) to 80x. At 60x-80x we see a geometric phase shift of $\varphi = \pi$ in the signal. Higher driving powers result in increased back-scattered laser light leading to the increase in average counts and a reduced fringe contrast is visible from 20x onwards.

For each spectral slice in figure 6.8(b) a series of Lorentzian curves were fitted to evaluate the energy splitting $E_{\pm}$. An example of this is shown in figure 6.8(c) with a single fit for each $E_{\pm}$ (dashed) and a combined fitting function that is a sum of two Lorentzians (solid line) which matches the experimentally acquired spectra well. Fitting parameters for $E_{\pm}$ were extracted and the peak centers for each are shown in figure 6.8(d).

The previous discussion of the custom-built spectrometer in section 2.3 stated that it was possible to resolve the spectra with an 8 μeV resolution and the data shown here is in excellent agreement. We include a line of best fit as a guide to the eye to extrapolate the splitting for $P_{\text{drive}} < 2$ mW$^{1/2}$ which could not be resolved easily.

The relative phase φ as a function of Ω_{drive} that accumulates between the dressed states has been observed across a range of systems with the main works inspiring these experiments conducted in [136]. Since the ground state spin-qubit is coupled through the upper trion states, which contain a negligible population, it has been shown that performing a Ramsey experiment under this experimental configuration allows direct

observation of the imparted geometric phase φ.

This is demonstrated in figure 6.9 for a range of driving field strengths with the initial strength of the resonant laser being $P_{1x} = 80$ nW. Two time-separated $\pi/2$-pulses were applied at varying delay to observe Ramsey fringes while the CW power was modified. The CW was continuously active for the duration between the pulses and was varied from the initial power ($P_{1x} = 80$ nW) to eighty times ($P_{80x} = 6.4$ mW) to observe an induced phase shift of $\varphi = \pi$.

At 80 nW (bottom) we see clear Ramsey fringes over 500 ps and additionally a nuclear polarization effect from approximately 400 ps onwards with an average count rate of 25k counts. By varying the power of the resonant drive and observing the data at the dashed line ($\sim$290 ps) we see larger field strengths cause an increased rate of the oscillation period in the Ramsey fringes. At values up to 80x a π-shift in the Ramsey signal is clearly observable at $\tau \approx 290$ ps when compared to the 1x acquisition.

At larger driving strengths there is a monotonic increase in the count rate caused by back-reflected laser light that cannot be fully extinguished due to the similar highly circular ($S_3 \approx 0.99$) polarizations of the coupled transitions under the oblique configuration. Additionally, at strengths from 20x onward we see a significant decrease in the fringe contrast as well as the quality of the fringes, this may be a result of the strong driving strength broadening the transitions in the QD leading to varied decay times impacting the measurements at larger fields.

As a means to minimize the impact on the data quality and enhance the effect, fabricating quantum dots confined to a high-Q cavity would greatly increase the QD-cavity coupling strength [28]. A high cavity-coupling strength would allow for induced phase shifts of π (or greater) to be imparted on to the spin-qubit at significantly reduced powers.

This impact upon both the fringe contrast and the background counts caused by back-reflected laser light would be anticipated to be greatly reduced. Finally, inclusion of cavity modes to strongly couple electric fields with enclosed QD's would also open up avenues for additional physics of strong light-matter interactions in the form of polaritons (exciton-photon quasi-particles) which are of particularly interest in many

spin systems and semiconductor materials.

While notable issues exist with both the contrast and count rate at greater driving powers, we have shown under oblique fields it is simple to implement an all-optical technique to impart a geometric phase on the rate of azimuthal precession of a QD spin-qubit. We find the precession frequency can be written as a sum of the magnetic field induced Larmor frequency and an optically-induced geometric phase ($\omega_{\text{azimuth}} = \omega_{\text{larmor}} + \omega_{\varphi}$). This geometric phase introduced is capable of manipulating the system on timescales comparable to the spin-qubits properties as opposed to a magnetic field that varies on timescales longer by many orders of magnitude.

6.4 Conclusion

The experiments performed in chapter 6 extended much of the knowledge and understanding regarding QD spin-qubits under a Voigt configuration to the oblique fields characterized in chapter 5. A complete coherent control demonstration was performed at $B_\theta = 60^\circ$ showing observations of Rabi, Ramsey fringes and a map of the SU(2) state space formed of the electronic ground states. Slight variations in the data from the Voigt case are observable yet even under oblique fields the spin-qubit performs remarkably well. The combined results of chapters 5 and 6 have successfully characterized and demonstrated that complex control of spin-qubits even under oblique magnetic fields to be straight forward with minimal impact to the efficacy of manipulations using an oblique configuration.

This has direct applications to the self-assembled quantum dots shown in this work but is also applicable to quantum dot systems fabricated in non-standard geometries such as the pyramidal QDs [50–52].

An experimental procedure to perform single-qubit quantum state tomography was demonstrated yielding successful reconstruction of two initial input states. We found the spin initialization process for the initial state $|Z\rangle_{\text{init}}$ yielded a fidelity $\mathcal{F}_Z = 0.978$ with near unity values predicted given optimization of experimental conditions. The second state $|Y\rangle_{\text{init}}$ was shown to deviate from the intended initial state prepared,

although this (accidental) result stood only to confirm the benefits of applying QST techniques by revealing quantitative results related to the actual initial spin-state as opposed to the idealized case.

The author highlighted ideas for further works regarding the state tomography method with QDs given dedicated time and resources. Further implementations of more complex tomographic techniques such as quantum process tomography would yield fruitful avenues if the results were used to iteratively improve the efficacy of spin rotations such as Z- and X-gates,

State tomography techniques are also directly applicable to investigate higher order density operators involving entanglement in QD systems, for example spin-photon entanglement can be quantified in QDs and other systems [191–193].

Quantum process tomography techniques could also be implemented with the same level of complexity and resources as multiple-qubit measurements. This would allow characterization of a range of operations applicable to QD spin-qubits (and qubits generally). Fidelities of the processes such as X- and Z-gate rotations can be extracted yielding quantifiable results with which to further enhance the efficacy of the processes.

The final section of this chapter successfully demonstrated an experiment that allows for an optically-induced geometric phase to be imparted. This impacts the rate at which the QD spin-qubits phase accumulates through application of a resonant driving field in-between time-delayed rotation pulses. Strong driving on the $|\uparrow\rangle \rightarrow |\uparrow\downarrow\Uparrow\rangle$ transition was shown to dress the transition leading to two new system eigenstates $|\pm\rangle$ that accumulate a variable phase φ dependent upon the energy splitting. While the excited trion state is never populated, resulting from the large pulse detunings far greater than the QD Zeeman splitting, a phase induced by the dressed states can be imparted on to the ground state spin-qubit and was clearly observed here.

A series of Ramsey measurements performed for various driving fields, and thus dressed state splittings, verified that a π-phase shift could be achieved for this QD by application of laser powers 80x the initial power used. The author posits these values could be reduced significantly by fabricating QD-cavity systems that greatly

enhance the light-matter coupling strength resulting in larger geometric phase shifts at lower driving fields. Such systems would show greatly improved control as well as an improved quality of the data. We would predict an improved fringe contrast and a notable reduction in the back-reflected laser light that led to a monotonic increase in the count rate.

In conclusion, we have shown that QD spin-qubits under oblique magnetic fields can reproduce results akin to a Voigt configuration remarkably well using the analysis of chapter 5 regarding oblique configurations. These results could be applied directly for research specifically interested in oblique magnetic field configurations or simply provide useful knowledge for researchers regarding non-standard magnetic fields to reduce barriers to work in such configurations by the clear, consistent and reproducible results present in chapters 5 and 6.

As the Voigt configuration has proven so successful much research typically defaults to this configuration as a path of least resistance. By disseminating the results gained here this should make such a choice less stringent and generally more flexible since reproducing results in these configurations has shown to be both effective and with minor issues.

Finally, fabrication of quantum dot samples in non-standard geometries in which oblique magnetic fields are essentially always present will benefit from the knowledge of the charged excitons shown here and may assist in helping future works to characterize such samples more easily based on the analyses shown.

Chapter 7

Conclusion and Future Outlook

With the last of the results in this body of work this final section contains concluding remarks and thoughts on what was presented. We follow this up with some of the authors thoughts towards a future outlook to continue this research. There are many possible avenues available and in general any further research, regardless of direction, has the possibility to bear fresh findings.

Quantum dots are an active and continuing branch of nanoscale semiconductor physics and the quality and capabilities will only improve over time. The results and methods shown here, which characterized charged quantum dots behavior under the non-standard magnetic field configurations, extends the existing body of knowledge for future researchers to build upon.

This work began with chapters 2 and 3 providing an in-depth explanation of the experimental setup that was used to produce all the results shown. This felt an essential inclusion for a variety of reasons. Firstly, the design and assembly phase required approximately 16-18 of the total 42 months prior to being able to obtain the first experimental results, making up a significant portion of the total time. More importantly, this resulted in both a broad and deep understanding of the experimental setup and the roles and functions of the components. By disseminating this knowledge in the manner that was done here, those who come to work with such setups in the future should have all the information necessary to develop the intuition. Once this intuition has been developed experiments such as presented here are able to operate at their

full potential.

Chapter 2 described the foundational components for many experiments performed at cryogenic temperatures. The magneto-cryostat was introduced and characterized after a successful adaption towards closed-cycle operation. This is beneficial as it is more sustainable and economical when applied to the research conducted. Both of these are important factors that should be taken into account when designing and building experiments. The design and build of a custom spectrometer and the lasers relevant for the experiment were also discussed. Chapter 3 further introduced the magneto-optical setup, alongside polarimetry techniques and pulse control equipment. The combination of which yields a high degree of control over the spin-states confined to semiconductor QDs.

The main results of this work were then introduced in chapters 4 through 6. Chapter 4 introduced the necessary theoretical background prior to recreating the seminal works demonstrating coherent control of ground-state electronic spins.

Reproduction of previous works has become something in research that is not performed as often as it should be, yet the author believes this to be an integral step prior to producing further research results. This is one of the reasons this chapter was included and termed *calibrating the experiment*. Verification of the setups capabilities allowed all future experiments to be conducted and interpreted with confidence. Complete coherent control of a singly-charged quantum dot under the Voigt configuration was demonstrated. The results when compared with previous works [64, 71, 122, 146, 194] were shown to be in good agreement.

In chapter 5 we performed an in-depth characterization of singly-charged quantum dots under non-standard oblique magnetic field configurations. The methods presented were clear and comprehensive allowing successful identification of the oblique field properties. Measurements taken at only $\theta_{obl} = 60^\circ$ and $\theta_V = 90^\circ$ allowed us to understand the expected behavior for arbitrary magnetic field angles. It was found that the spin-states of the quantum dot can be formed from unequal contributions of the basis states. This can be tailored through application of oblique magnetic fields yielding an additional axis of control. Furthermore, demonstration of spin pumping

under oblique fields highlighted that oblique field coherent control was possible and stimulated the further research of chapter 6.

Finally, in chapter 6 we demonstrated a variety of complex spin-qubit control experiments under the non-standard magnetic field configuration. This began by extending the demonstration from chapter 4 into this configuration by performing the complete coherent control experimental sequence. From this we found that oblique field charged QD spin-qubits perform remarkably well. Upon comparison with coherent control under the Voigt configuration there appears to be no significant degradation in the efficacy.

An implementation of the quantum state tomography technique allowed for successful reconstruction of two initial input states. Both states were compared with the idealized case where one state was shown to be incorrectly prepared. Regardless, from the evaluated fidelities we found that the fidelity for the spin initialization $|Z\rangle$ under oblique fields was $\mathcal{F}_Z = 0.978$. This value should be taken with slight caution as optimization of the spin initialization procedure was not conducted, yet it is still indicative of QD spin-qubit capabilities under non-standard field configurations.

Finally, we demonstrated the capability to impart a geometric phase on the spin-qubit through application of a strong resonant driving field. By dressing the system states we showed an accumulated π phase shift onto the spin-qubit. This equates to increasing the rate of precession around the azimuthal axis on the Bloch sphere.

The understanding that the spin-states of a charged QD can be specifically tailored using tilted magnetic field opens up a range of possibilities for further research. Quantum dots show great potential when harnessed as a single spin-qubit and fabrication methods yield high densities of quantum dots (and so possible qubits) that have the potential to build scalable systems for quantum information processing. Yet as stated in chapter 1 quantum dots still exhibit no consistent and reliable method of interacting between distant quantum dots.

The introduction of oblique magnetic fields in chapter 5 demonstrated the composition of the spin-qubit states can be tailored to contain unequal spin-state weightings as a function of the magnetic field. This imbalance between the spin-states hints to-

wards separate internal spin-qubit states that could respond differently to specifically tailored excitation methods. Additionally, it hints towards emission from such spin-qubits to also have an unbalanced signature that could either be detected or interacted with preferentially.

Here we propose some ideas for a future direction to take advantage of the results presented to try and address the issue of interaction between distant quantum dots. The introduction of a 2D quantum well like structure some nanometers below the quantum dot layer is a key avenue of interest. If enclosed in a high-Q cavity to allow the strong-coupling regime with a high Purcell factor [28] this can allow for the generation of exciton-polaritons within this layer. If there is wavefunction overlap then interactions can occur [102] between a QD and an exciton-polariton confined to the 2D layer.

The appeal is that exciton-polaritons [195], a light-matter quasi-particle, contain polarization degrees of freedom from both their photonic and spin-based matter components. The transfer of a QDs polarization information onto an exciton-polariton thus yields an interaction medium with which to communicate with distant QDs. Since the polarization state in a Poincare sphere picture is synonymous with the Bloch sphere single-qubit representation [196], then the single-qubit can be retained and transferred. The proposal then is the fabrication of a self-assembled quantum dot sample coupled with a 2D quantum well layer enclosed in a DBR cavity.

The impact of the results presented in chapters 5 and 6 contribute additionally by the unequivocal demonstration that non-standard configurations can be readily challenged with only minor adaptions. While at first this may not appear essential much of the body of existing knowledge with QD spin-qubits has defaulted to the Voigt configuration. By verifying the properties of quantum dots under non-standard configurations, this can then be easily applied to other quantum dots such as the pyramidal (111) quantum dots [50–53]. These samples are grown using metal-organic vapor phase epitaxy (MOVPVE) [54] which allows for precise site-controlled growth methods. This is promising for future applications of quantum dots in scalable quantum information processing, allowing for predictable and scalable arrays of quantum dots.

In conclusion, the results presented in this work demonstrated the strengths of quantum dots as spin-based single-qubits. This was shown to persist into non-standard magnetic field configurations highlighting the flexibility of using such structures. The key setback is the lack of a reliable method for interactions between distant quantum dots from which we conclude that applications for more complex information processing purposes is limited. However, combining the results shown here with future works incorporating exciton-polariton interactions with a nearby 2D quantum well like structure to take advantage of the imbalanced spin-states that can be deterministically produced may be a key component to bridge this gap. Further research in this direction would be an excellent avenue for further research related to this work.

Appendix A

Appendix A - Mueller Matrices

This short appendix provides a brief explanation of how we transition from the continuous Stokes intensity function to the discrete case, followed by the Mueller matrices commonly used.

A.1 Fourier components - continuous to discrete case

By transition to a discrete expression the experimentally acquired data can be analyzed using the polarimetry techniques discussed in 3.2. Using equations 3.3 -3.6 the expression for the Stokes intensity function can be found (discussed in detail in [114]). This expression in its most generalized form is written as,

$$I(\theta, \phi) = \frac{1}{2}[S_0 + S_1 \cdot \cos 2\theta + S_2 \cdot \cos\phi \sin 2\theta + S_3 \cdot \sin\phi \sin 2\theta], \tag{A.1}$$

where θ is an angle related to the angle of a waveplate component and ϕ is the phase retardation. Setting $\phi = \pi/4$ as with a quarter-waveplate and noting that A.1 can be expressed using Fourier series analysis we can arrive at 3.10 . The coefficients A-D in the continuous case can be found by evaluating the following,

$$A = \frac{1}{\pi}\int_0^{2\pi} I(\theta)\, d\theta, \qquad B = \frac{2}{\pi}\int_0^{2\pi} I(\theta)\sin 2\theta\, d\theta,$$
$$C = \frac{2}{\pi}\int_0^{2\pi} I(\theta)\cos 4\theta\, d\theta, \qquad D = \frac{2}{\pi}\int_0^{2\pi} I(\theta)\sin 4\theta\, d\theta. \tag{A.2}$$

Experimental data acquired using the polarimetry setup was typically conducted using 2° steps of the waveplate angle from 0-358° yielding 180 data points. To transition from the continuous to the discrete case we perform a change of variables, with $\Delta n = 2\pi/N$, to find the following expressions,

$$A = \frac{2}{N}\sum_{n=1}^{N} I(\theta_n) \tag{A.3}$$
$$B = \frac{4}{N}\sum_{n=1}^{N} I(\theta_n)\sin 2\theta_n, \tag{A.4}$$
$$C = \frac{4}{N}\sum_{n=1}^{N} I(\theta_n)\cos 4\theta_n, \tag{A.5}$$
$$D = \frac{4}{N}\sum_{n=1}^{N} I(\theta_n)\sin 4\theta_n. \tag{A.6}$$

Equations A.3 -A.6 thus allow for evaluation of the intensity function using experimental data acquired through the polarimetry techniques discussed.

A.2 Mueller matrices

The expressions for some common Mueller matrices used are listed below for a linear polarizer and the generalized waveplate and quarter- and half-waveplate. θ relates to the angle of rotation while ϕ is the retardation angle.

These are as follows:

Generalized linear polarizer

$$M_{\text{pol}}(\theta) = \frac{1}{2}\begin{pmatrix} 1 & \cos 2\theta & \sin 2\theta & 0 \\ \cos 2\theta & \cos^2 2\theta & \cos 2\theta \sin 2\theta & 0 \\ 0 & \cos 2\theta \sin 2\theta & \sin^2 2\theta & 0 \\ 0 & 0 & 0 & 0 \end{pmatrix} \tag{A.7}$$

Generalized waveplate

$$M_{\text{wp}}(\theta, \phi) = \begin{pmatrix} 1 & 0 & 0 & 0 \\ 0 & \cos^2 2\theta + \sin^2 2\theta \cos\phi & \cos 2\theta \sin 2\theta(1 - \cos\phi) & -\sin 2\theta \sin\phi \\ 0 & \cos 2\theta \sin 2\theta(1 - \cos\phi) & \cos^2 2\theta \cos\phi + \sin^2 2\theta & \cos 2\theta \sin\phi \\ 0 & \sin 2\theta \sin\phi & -\cos 2\theta \sin\phi & \cos\phi \end{pmatrix} \tag{A.8}$$

Quarter-waveplate

$$M_{\text{qwp}}(\theta, \phi = \pi/2) = \begin{pmatrix} 1 & 0 & 0 & 0 \\ 0 & \cos^2 2\theta & \cos 2\theta \sin 2\theta & -\sin 2\theta \\ 0 & \sin 2\theta \cos 2\theta & \sin^2 2\theta & \cos 2\theta \\ 0 & -\sin 2\theta & -\cos 2\theta & 0 \end{pmatrix} \tag{A.9}$$

Half-waveplate

$$M_{\text{hwp}}(\theta, \phi = \pi) = \begin{pmatrix} 1 & 0 & 0 & 0 \\ 0 & \cos 4\theta & \sin 4\theta & 0 \\ 0 & \sin 4\theta & -\cos 4\theta & 0 \\ 0 & 0 & 0 & -1 \end{pmatrix} \tag{A.10}$$

Appendix B

Appendix B - Photon Interference

Here we discuss an interesting effect that was observed during the course of coherent control experiments under oblique magnetic fields. The spin pumping discussed in chapters 4 and 5 was performed using resonant CW excitation to initialize the system and above-band excitation acted to randomize the ground state spins. The result is the typical Lorentzian profile shown throughout this work.

This experiment can similarly be conducted using pulsed excitation to generate coherent rotations between the ground states as described in chapter 4. As shown in figure B.1, with the pulse laser power set such that $\theta = \pi$, a population initially in $|\downarrow\rangle_x$ will be transferred to $|\uparrow\rangle_x$ with near unit probability. Figure B.2(a) shows Rabi oscillations under the Voigt configuration showing a π-pulse power P_π $\sim$4.2 $\mu W^{1/2}$ which can then be used to initialize a π-pulse spin pump experiment. This acts as the state initialization previously performed using resonant CW excitation, by having a CW excitation on the coupled transition we can detect if the system was successfully transferred through emission of a photon.

This is shown in figure B.1(b) shows the expected Lorentzian profile for the spin pumping experiment using a π-pulse to initialize the system. The CW laser had a power of P = 50 nW which was used to perform a readout operation. As shown previously the experiment was performed both with and without low power above-band excitation to randomize the ground states.

The CW used for readout on the diagonal cross-transition in B.1 shares a near iden-

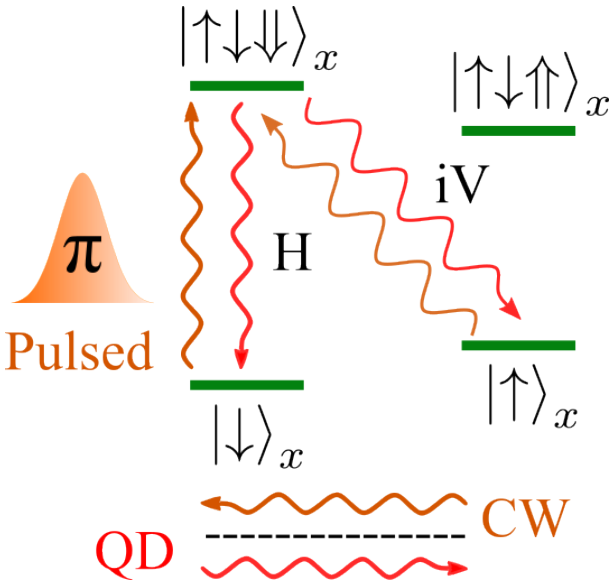

Figure B.1: The CW cross-transition initializes the system into the state $|\downarrow\rangle_x$ at which the π-pulse will excite the $|\downarrow\rangle_x \rightarrow |\uparrow\rangle_x$ transition synonymous to a spin pumping experiment. Once the CW resonantly excites the system to the upper trion state, this will decay with equal probability into the ground states $\{|\uparrow\rangle_x, |\downarrow\rangle_x\}$. If the CW is of sufficiently low power when the system decays back to $|\uparrow\rangle_x$ destructive interference between CW laser photons and the QD emission from the $|\uparrow\downarrow\Uparrow\rangle_x \rightarrow |\uparrow\rangle_x$ leads to the observed results of figure B.2.

tical frequency and polarization to photons emitted from the QD on the same transition. As these photons are similar and hence maintain a degree of coherence resulting in a destructive interference effect if the conditions are correct. With the CW power is sufficiently low (P = 5 nW) the photons emitted from the QD into the cross-transition can destructively interfere with the CW laser. This is clearly visible in figure B.2(c) (purple) and in figure B.2(d) which is the same data zoomed in for better clarity. We see that there is an on resonance dip in counts that is a result of the destructive interference occuring when the frequency of the CW laser matches the QD transition frequency.

The data shown here was performed under the Voigt configuration although the effect was initially observed when gathering the results presented in chapter 6 under an oblique configuration. When the author initially saw this effect they believed this may have been some coherent population trapping/electromagnetically induced

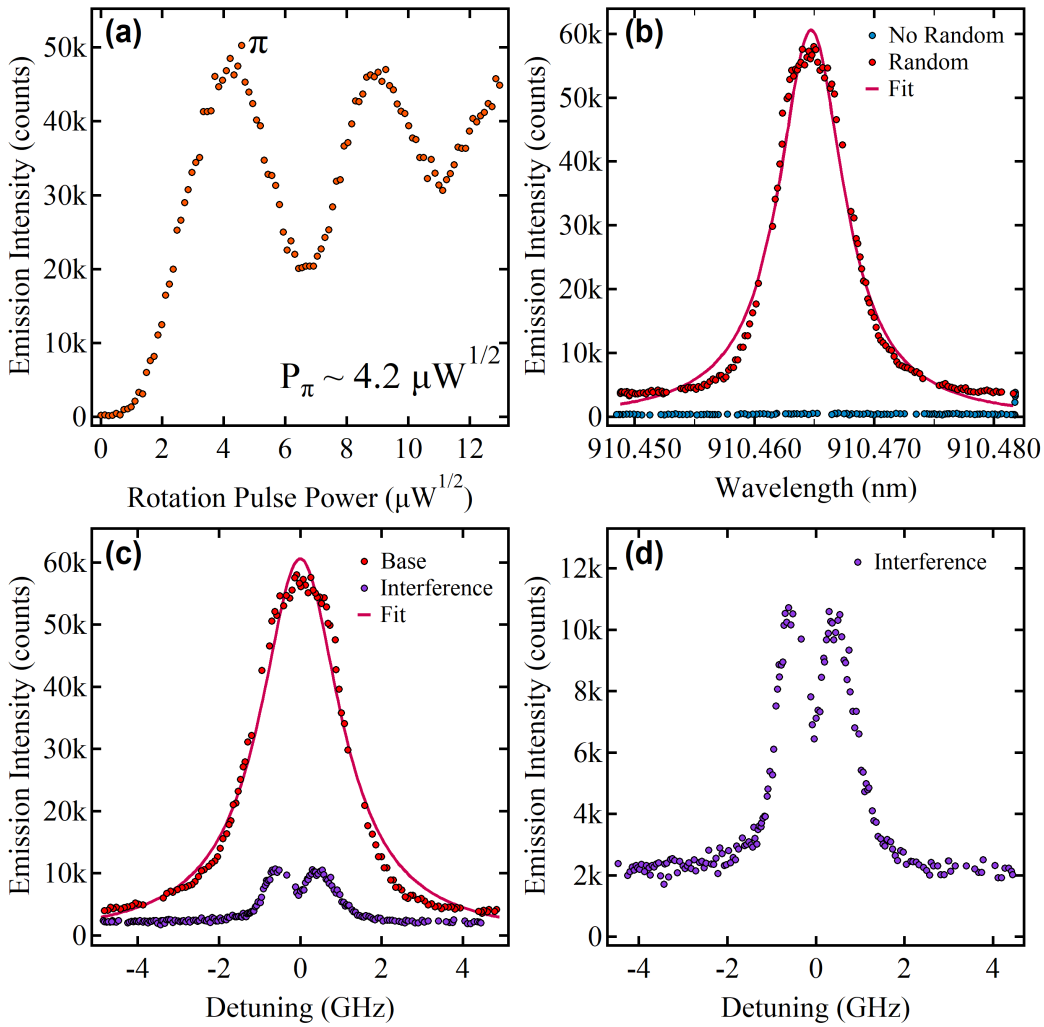

Figure B.2: (a) Rabi rotations as a function of the square root of the pulse power with the value π-pulse power $\sim$ 4.2 $\mu W^{1/2}$. (b) Spin pumping results of experiment performed with the pulse power set to P_π both with and without above-band excitation to randomize the ground states. The CW initialization laser power was set to P = 50 nW. (c) Red shows the same data as in (b) and the results when the CW is set to 1/10 of the power P = 5 nW. An observable dip in counts is observed at zero detuning. (d) Same interference data as in (c) only zoomed in for better clarity.

transparency (CPT/EIT) like effect (leading to quite some excitement!). Although instead the much simpler explanation presented here correctly interprets the results. To correctly identify this effect the data was reproduced under the Voigt configuration, this was to reduce the complexity of the system since the Voigt configurations proper-

ties are well understood. In doing so, the reproduction of the results allowed for the interpretation presented here.

While the effects were not related to CPT observing such an effect and taking steps to reduce the system complexity and methodically identify the causes was a valuable process. This brief appendix exists simply to highlight that while not all effects are groundbreaking, there can be interesting effects to observe when you least expect it. Additionally, that when observations are unexpected finding methodical ways to characterize the system is at the heart of good research.

Bibliography

[1] A. Aspect, J. Dalibard, and G. Roger, "Experimental Test of Bell's Inequalities Using Time-Varying Analyzers," *Physical Review Letters*, vol. 49, pp. 1804–1807, Dec. 1982.

[2] J. F. Clauser and A. Shimony, "Bell's theorem. Experimental tests and implications," *Reports on Progress in Physics*, vol. 41, p. 1881, Dec. 1978.

[3] D. M. Greenberger, M. A. Horne, A. Shimony, and A. Zeilinger, "Bell's theorem without inequalities," *American Journal of Physics*, vol. 58, pp. 1131–1143, Dec. 1990.

[4] J. M. Raimond, M. Brune, S. Haroche, and L. K. Brossel, "Colloquium: Manipulating quantum entanglement with atoms and photons in a cavity," *Rev. Mod. Phys.*, vol. 73, no. 3, 2001.

[5] M. Brune, S. Haroche, J. M. Raimond, L. Davidovich, and N. Zagury, "Manipulation of photons in a cavity by dispersive atom-field coupling: Quantum-nondemolition measurements and generation of "Schr\"odinger cat" states," *Physical Review A*, vol. 45, pp. 5193–5214, Apr. 1992.

[6] S. Gleyzes, S. Kuhr, C. Guerlin, J. Bernu, S. Deléglise, U. Busk Hoff, M. Brune, J.-M. Raimond, and S. Haroche, "Quantum jumps of light recording the birth and death of a photon in a cavity," *Nature*, vol. 446, pp. 297–300, Mar. 2007.

[7] C. Monroe, D. M. Meekhof, B. E. King, and D. J. Wineland, "A "Schrödinger Cat" Superposition State of an Atom," *Science*, vol. 272, pp. 1131–1136, May 1996.

[8] R. J. Glauber, "The Quantum Theory of Optical Coherence," *Physical Review*, vol. 130, pp. 2529–2539, June 1963.

[9] S. M. Barnett, "Introduction to Quantum Information,"

[10] M. A. Nielsen and I. L. Chuang, *Quantum Computation and Quantum Information: 10th Anniversary Edition*. Cambridge University Press, Dec. 2010.

[11] S. Stenholm and K.-A. Suominen, *Quantum Approach to Informatics*. John Wiley & Sons, Sept. 2005.

[12] P. W. Shor, "Polynomial-Time Algorithms for Prime Factorization and Discrete Logarithms on a Quantum Computer." https://arxiv.org/abs/quant-ph/9508027v2, Aug. 1995.

[13] L. K. Grover, "Quantum Mechanics Helps in Searching for a Needle in a Haystack," *Physical Review Letters*, vol. 79, pp. 325–328, July 1997.

[14] D. Deutsch and R. Penrose, "Quantum theory, the Church–Turing principle and the universal quantum computer," *Proceedings of the Royal Society of London. A. Mathematical and Physical Sciences*, vol. 400, pp. 97–117, Jan. 1997.

[15] S. Gulde, M. Riebe, G. P. T. Lancaster, C. Becher, J. Eschner, H. Häffner, F. Schmidt-Kaler, I. L. Chuang, and R. Blatt, "Implementation of the Deutsch–Jozsa algorithm on an ion-trap quantum computer," *Nature*, vol. 421, pp. 48–50, Jan. 2003.

[16] "Exploring the many-body localization transition in two dimensions." https://www.science.org/doi/10.1126/science.aaf8834.

[17] "Controlling quantum many-body dynamics in driven Rydberg atom arrays." https://www.science.org/doi/10.1126/science.abg2530.

[18] P. Scholl, M. Schuler, H. J. Williams, A. A. Eberharter, D. Barredo, K.-N. Schymik, V. Lienhard, L.-P. Henry, T. C. Lang, T. Lahaye, A. M. Läuchli, and A. Browaeys, "Quantum simulation of 2D antiferromagnets with hundreds of Rydberg atoms," *Nature*, vol. 595, pp. 233–238, July 2021.

[19] C. Lagoin, U. Bhattacharya, T. Grass, R. W. Chhajlany, T. Salamon, K. Baldwin, L. Pfeiffer, M. Lewenstein, M. Holzmann, and F. Dubin, "Extended Bose–Hubbard model with dipolar excitons," *Nature*, vol. 609, pp. 485–489, Sept. 2022.

[20] C. Lagoin, S. Suffit, K. Baldwin, L. Pfeiffer, and F. Dubin, "Mott insulator of strongly interacting two-dimensional semiconductor excitons," *Nature Physics*, vol. 18, pp. 149–153, Feb. 2022.

[21] "String patterns in the doped Hubbard model." https://www.science.org/doi/10.1126/science.aav3587.

[22] J. Koepsell, J. Vijayan, P. Sompet, F. Grusdt, T. A. Hilker, E. Demler, G. Salomon, I. Bloch, and C. Gross, "Imaging magnetic polarons in the doped Fermi–Hubbard model," *Nature*, vol. 572, pp. 358–362, Aug. 2019.

[23] A. J. Daley, I. Bloch, C. Kokail, S. Flannigan, N. Pearson, M. Troyer, and P. Zoller, "Practical quantum advantage in quantum simulation," *Nature*, vol. 607, pp. 667–676, July 2022.

[24] I. H. Deutsch, "Harnessing the Power of the Second Quantum Revolution," *PRX Quantum*, vol. 1, p. 020101, Nov. 2020.

[25] T. D. Ladd, F. Jelezko, R. Laflamme, Y. Nakamura, C. Monroe, and J. L. O'Brien, "Quantum computers," *Nature*, vol. 464, pp. 45–53, Mar. 2010.

[26] X. Li and W. Chen, "Economic Impacts of Quantum Computing: Strategies for Integrating Quantum Technologies into Business Models," *Eigenpub Review of Science and Technology*, vol. 7, pp. 277–290, Nov. 2023.

[27] P. G. Eliseev, H. Li, A. Stintz, G. T. Liu, T. C. Newell, K. J. Malloy, and L. F. Lester, "Transition dipole moment of InAs/InGaAs quantum dots from experiments on ultralow-threshold laser diodes," *Applied Physics Letters*, vol. 77, pp. 262–264, July 2000.

[28] A. Kavokin, J. J. Baumberg, G. Malpuech, and F. P. Laussy, *Microcavities*. USA: Oxford University Press, Inc., Jan. 2008.

[29] P. W. Shor and J. Preskill, "Simple Proof of Security of the BB84 Quantum Key Distribution Protocol," *Physical Review Letters*, vol. 85, pp. 441–444, July 2000.

[30] D. P. DiVincenzo and IBM, "The Physical Implementation of Quantum Computation," *Fortschritte der Physik*, vol. 48, pp. 771–783, Sept. 2000. Comment: Prepared for Fortschritte der Physik special issue, Experimental Proposals for Quantum Computation. Version 2: many small corrections. Version 3: more small corrections & references added.

[31] A. Mittelstädt, A. Schliwa, and P. Klenovský, "Modeling electronic and optical properties of III–V quantum dots—selected recent developments," *Light: Science & Applications*, vol. 11, p. 17, Jan. 2022. Publisher: Nature Publishing Group.

[32] G. Ragunathan, "Nuclear Spin Phenomena in III-V and II-VI Semiconductor Quantum Dots,"

[33] L. Sapienza, R. Al-Khuzheyri, A. Dada, A. Griffiths, E. Clarke, and B. D. Gerardot, "Magneto-optical spectroscopy of single charge-tunable InAs/GaAs quantum dots emitting at telecom wavelengths," *Physical Review B*, vol. 93, p. 155301, Apr. 2016.

[34] Ł. Dusanowski, C. Nawrath, S. L. Portalupi, M. Jetter, T. Huber, S. Klembt, P. Michler, and S. Höfling, "Optical charge injection and coherent control of a quantum-dot spin-qubit emitting at telecom wavelengths," *Nature Communications*, vol. 13, p. 748, Feb. 2022.

[35] A. Kors, J. P. Reithmaier, and M. Benyoucef, "Telecom wavelength single quantum dots with very small excitonic fine-structure splitting," *Applied Physics Letters*, vol. 112, p. 172102, Apr. 2018.

[36] S. Lee, M. Dobrowolska, and J. K. Furdyna, "6 - Epitaxial II-VI semiconductor quantum structures involving dilute magnetic semiconductors," in *Chalcogenide* (X. Liu, S. Lee, J. K. Furdyna, T. Luo, and Y.-H. Zhang, eds.), Woodhead Publishing Series in Electronic and Optical Materials, pp. 153–187, Woodhead Publishing, Jan. 2020.

[37] Y. Léger, L. Besombes, L. Maingault, and H. Mariette, "Valence-band mixing in neutral, charged, and Mn-doped self-assembled quantum dots," *Physical Review B*, vol. 76, p. 045331, July 2007.

[38] Y. Léger, L. Besombes, L. Maingault, D. Ferrand, and H. Mariette, "Geometrical Effects on the Optical Properties of Quantum Dots Doped with a Single Magnetic Atom," *Physical Review Letters*, vol. 95, p. 047403, July 2005.

[39] R. M. Abolfath and T. Brabec, "Performance engineering of semiconductor spin qubit systems," *Physical Review B*, vol. 82, p. 075311, Aug. 2010. Publisher: American Physical Society.

[40] B. Urbaszek, X. Marie, T. Amand, O. Krebs, P. Voisin, P. Maletinsky, A. Högele, and A. Imamoglu, "Nuclear spin physics in quantum dots: An optical investigation," *Reviews of Modern Physics*, vol. 85, pp. 79–133, Jan. 2013. Nuclear Spin Review.

[41] J. Dreiser, M. Atature, C. Galland, T. Muller, A. Badolato, and A. Imamoglu, "Optical investigations of quantum-dot spin dynamics," *arXiv:0705.3557 [cond-mat, physics:quant-ph]*, May 2007. Comment: submitted to Physical Review B, 19 Pages in RevTeX4 format.

[42] L. Childress, M. V. Gurudev Dutt, J. M. Taylor, A. S. Zibrov, F. Jelezko, J. Wrachtrup, P. R. Hemmer, and M. D. Lukin, "Coherent Dynamics of Coupled Electron and Nuclear Spin Qubits in Diamond," *Science*, vol. 314, pp. 281–285, Oct. 2006. Publisher: American Association for the Advancement of Science.

[43] R. Hanson, F. M. Mendoza, R. J. Epstein, and D. D. Awschalom, "Polarization and Readout of Coupled Single Spins in Diamond," *Physical Review Letters*, vol. 97, p. 087601, Aug. 2006. Publisher: American Physical Society.

[44] F. Jelezko, T. Gaebel, I. Popa, M. Domhan, A. Gruber, and J. Wrachtrup, "Observation of Coherent Oscillation of a Single Nuclear Spin and Realization of a Two-Qubit Conditional Quantum Gate," *Physical Review Letters*, vol. 93, p. 130501, Sept. 2004. Publisher: American Physical Society.

[45] C. Santori, P. Tamarat, P. Neumann, J. Wrachtrup, D. Fattal, R. G. Beausoleil, J. Rabeau, P. Olivero, A. D. Greentree, S. Prawer, F. Jelezko, and P. Hemmer, "Coherent Population Trapping of Single Spins in Diamond under Optical Excitation," *Physical Review Letters*, vol. 97, p. 247401, Dec. 2006.

[46] T. Gaebel, M. Domhan, I. Popa, C. Wittmann, P. Neumann, F. Jelezko, J. R. Rabeau, N. Stavrias, A. D. Greentree, S. Prawer, J. Meijer, J. Twamley, P. R. Hemmer, and J. Wrachtrup, "Room-temperature coherent coupling of single spins in diamond," *Nature Physics*, vol. 2, pp. 408–413, June 2006. Publisher: Nature Publishing Group.

[47] R. J. Epstein, F. M. Mendoza, Y. K. Kato, and D. D. Awschalom, "Anisotropic interactions of a single spin and dark-spin spectroscopy in diamond," *Nature Physics*, vol. 1, pp. 94–98, Nov. 2005. Publisher: Nature Publishing Group.

[48] J. Wrachtrup and F. Jelezko, "Processing quantum information in diamond," *Journal of Physics: Condensed Matter*, vol. 18, p. S807, May 2006.

[49] F. Jelezko, I. Popa, A. Gruber, C. Tietz, J. Wrachtrup, A. Nizovtsev, and S. Kilin, "Single spin states in a defect center resolved by optical spectroscopy," *Applied Physics Letters*, vol. 81, pp. 2160–2162, Sept. 2002.

[50] G. Juska, V. Dimastrodonato, L. O. Mereni, A. Gocalinska, and E. Pelucchi, "Towards quantum-dot arrays of entangled photon emitters," *Nature Photonics*, vol. 7, pp. 527–531, July 2013.

[51] G. Juska, V. Dimastrodonato, L. O. Mereni, A. Gocalinska, and E. Pelucchi, "A study of nitrogen incorporation in pyramidal site-controlled quantum dots," *Nanoscale Research Letters*, vol. 6, p. 567, Oct. 2011.

[52] G. Juska, E. Murray, V. Dimastrodonato, T. H. Chung, S. T. Moroni, A. Gocalinska, and E. Pelucchi, "Conditions for entangled photon emission from (111)B site-controlled pyramidal quantum dots," *Journal of Applied Physics*, vol. 117, p. 134302, Apr. 2015.

[53] S. T. Moroni, T. H. Chung, G. Juska, A. Gocalinska, and E. Pelucchi, "Statistical study of stacked/coupled site-controlled pyramidal quantum dots and their excitonic properties," *Applied Physics Letters*, vol. 111, p. 083103, Aug. 2017.

[54] K. M. Holsgrove, T. I. O'Reilly, S. Varo, A. Gocalinska, G. Juska, D. M. Kepaptsoglou, E. Pelucchi, and M. Arredondo, "Towards 3D characterisation of site-controlled InGaAs pyramidal QDs at the nanoscale," *Journal of Materials Science*, vol. 57, pp. 16383–16396, Sept. 2022.

[55] M. Burakowski, P. Mrowiński, M. Gawełczyk, J. P. Reithmaier, S. Höfling, and G. Sęk, "Diamagnetic coefficients and g-factors of InAs/InGaAlAs quantum dashes emitting at telecom wavelengths," *Journal of Applied Physics*, vol. 132, p. 144301, Oct. 2022.

[56] M. Gurioli, Z. Wang, A. Rastelli, T. Kuroda, and S. Sanguinetti, "Droplet epitaxy of semiconductor nanostructures for quantum photonic devices," *Nature Materials*, vol. 18, pp. 799–810, Aug. 2019.

[57] D. J. Eaglesham and M. Cerullo, "Dislocation-free Stranski-Krastanow growth of Ge on Si(100)," *Physical Review Letters*, vol. 64, pp. 1943–1946, Apr. 1990.

[58] D. Leonard, M. Krishnamurthy, C. M. Reaves, S. P. Denbaars, and P. M. Petroff, "Direct formation of quantum-sized dots from uniform coherent islands of InGaAs on GaAs surfaces," *Applied Physics Letters*, vol. 63, pp. 3203–3205, Dec. 1993.

[59] D. Loss and D. P. DiVincenzo, "Quantum computation with quantum dots," *Physical Review A*, vol. 57, pp. 120–126, Jan. 1998.

[60] S. Seidl, M. Kroner, A. Högele, K. Karrai, R. J. Warburton, A. Badolato, and P. M. Petroff, "Effect of uniaxial stress on excitons in a self-assembled quantum dot," *Applied Physics Letters*, vol. 88, p. 203113, May 2006.

[61] K. D. Jöns, R. Hafenbrak, R. Singh, F. Ding, J. D. Plumhof, A. Rastelli, O. G. Schmidt, G. Bester, and P. Michler, "Depen-

dence of the Redshifted and Blueshifted Photoluminescence Spectra of Single ${\mathrm{In}}_{x}{\mathrm{Ga}}_{1\ensuremath{-}x}\mathrm{As}/\mathrm{GaAs}$ Quantum Dots on the Applied Uniaxial Stress," *Physical Review Letters*, vol. 107, p. 217402, Nov. 2011.

[62] R. J. Warburton, C. Schulhauser, D. Haft, C. Schäflein, K. Karrai, J. M. Garcia, W. Schoenfeld, and P. M. Petroff, "Giant permanent dipole moments of excitons in semiconductor nanostructures," *Physical Review B*, vol. 65, p. 113303, Feb. 2002.

[63] A. J. Bennett, M. A. Pooley, R. M. Stevenson, M. B. Ward, R. B. Patel, A. B. de la Giroday, N. Sköld, I. Farrer, C. A. Nicoll, D. A. Ritchie, and A. J. Shields, "Electric-field-induced coherent coupling of the exciton states in a single quantum dot," *Nature Physics*, vol. 6, pp. 947–950, Dec. 2010.

[64] D. Press, T. D. Ladd, B. Zhang, and Y. Yamamoto, "Complete quantum control of a single quantum dot spin using ultrafast optical pulses," *Nature*, vol. 456, pp. 218–221, Nov. 2008.

[65] R. J. Warburton, "Single spins in self-assembled quantum dots," *Nature Materials*, vol. 12, pp. 483–493, June 2013. Spins Review.

[66] J. Fischer, W. A. Coish, D. V. Bulaev, and D. Loss, "Spin decoherence of a heavy hole coupled to nuclear spins in a quantum dot," *Physical Review B*, vol. 78, p. 155329, Oct. 2008.

[67] D. Heiss, S. Schaeck, H. Huebl, M. Bichler, G. Abstreiter, J. J. Finley, D. V. Bulaev, and D. Loss, "Observation of extremely slow hole spin relaxation in self-assembled quantum dots," *Physical Review B*, vol. 76, p. 241306, Dec. 2007. Comment: Published by Physical Review B.

[68] Y. Li, N. Sinitsyn, D. L. Smith, D. Reuter, A. D. Wieck, D. R. Yakovlev, M. Bayer, and S. A. Crooker, "Intrinsic Spin Fluctuations Reveal the Dynamical Response Function of Holes Coupled to Nuclear Spin Baths in (In,Ga)As Quantum Dots," *Physical Review Letters*, vol. 108, p. 186603, May 2012.

[69] R. Dahbashi, J. Hübner, F. Berski, K. Pierz, and M. Oestreich, "Optical Spin Noise of a Single Hole Spin Localized in an (InGa)As Quantum Dot," *Physical Review Letters*, vol. 112, p. 156601, Apr. 2014.

[70] G. Gillard, I. M. Griffiths, G. Ragunathan, A. Ulhaq, C. McEwan, E. Clarke, and E. A. Chekhovich, "Fundamental limits of electron and nuclear spin qubit lifetimes in an isolated self-assembled quantum dot," *npj Quantum Information*, vol. 7, p. 43, Dec. 2021.

[71] D. Press, K. De Greve, P. L. McMahon, T. D. Ladd, B. Friess, C. Schneider, M. Kamp, S. Höfling, A. Forchel, and Y. Yamamoto, "Ultrafast optical spin echo in a single quantum dot," *Nature Photonics*, vol. 4, pp. 367–370, June 2010.

[72] G. Burkard, T. D. Ladd, A. Pan, J. M. Nichol, and J. R. Petta, "Semiconductor spin qubits," *Reviews of Modern Physics*, vol. 95, p. 025003, June 2023.

[73] K. D. Greve, D. Press, P. L. McMahon, and Y. Yamamoto, "Ultrafast optical control of individual quantum dot spin qubits," *Reports on Progress in Physics*, vol. 76, p. 092501, Sept. 2013.

[74] T. M. Godden, J. H. Quilter, A. J. Ramsay, Y. Wu, P. Brereton, S. J. Boyle, I. J. Luxmoore, J. Puebla-Nunez, A. M. Fox, and M. S. Skolnick, "Coherent Optical Control of the Spin of a Single Hole in an $\mathrm{InAs}/\mathrm{GaAs}$ Quantum Dot," *Physical Review Letters*, vol. 108, p. 017402, Jan. 2012.

[75] S. J. Boyle, A. J. Ramsay, F. Bello, H. Y. Liu, M. Hopkinson, A. M. Fox, and M. S. Skolnick, "Two-qubit conditional quantum-logic operation in a single self-assembled quantum dot," *Physical Review B*, vol. 78, p. 075301, Aug. 2008.

[76] A. Imamoglu, D. D. Awschalom, G. Burkard, D. P. DiVincenzo, D. Loss, M. Sherwin, and A. Small, "Quantum Information Processing Using Quantum Dot Spins and Cavity QED," *Physical Review Letters*, vol. 83, pp. 4204–4207, Nov. 1999.

[77] I. Schwartz, D. Cogan, E. R. Schmidgall, L. Gantz, Y. Don, M. Zieliński, and D. Gershoni, "Deterministic coherent writing of a long-lived semiconductor spin qubit using one ultrafast optical pulse," *Physical Review B*, vol. 92, p. 201201, Nov. 2015.

[78] Y. Benny, S. Khatsevich, Y. Kodriano, E. Poem, R. Presman, D. Galushko, P. M. Petroff, and D. Gershoni, "Coherent Optical Writing and Reading of the Exciton Spin State in Single Quantum Dots," *Physical Review Letters*, vol. 106, p. 040504, Jan. 2011.

[79] T.-J. Wang, S.-Y. Song, and G. L. Long, "Quantum repeater based on spatial entanglement of photons and quantum-dot spins in optical microcavities," *Physical Review A*, vol. 85, p. 062311, June 2012.

[80] J. Neuwirth, F. B. Basset, M. B. Rota, E. Roccia, C. Schimpf, K. D. Jöns, A. Rastelli, and R. Trotta, "Quantum dot technology for quantum repeaters: From entangled photon generation toward the integration with quantum memories," *Materials for Quantum Technology*, vol. 1, p. 043001, Dec. 2021.

[81] I. Aharonovich, D. Englund, and M. Toth, "Solid-state single-photon emitters," *Nature Photonics*, vol. 10, pp. 631–641, Oct. 2016.

[82] M. Varnava, D. E. Browne, and T. Rudolph, "How Good Must Single Photon Sources and Detectors Be for Efficient Linear Optical Quantum Computation?," *Physical Review Letters*, vol. 100, p. 060502, Feb. 2008.

[83] S. D. Barrett and P. Kok, "Efficient high-fidelity quantum computation using matter qubits and linear optics," *Physical Review A*, vol. 71, p. 060310, June 2005.

[84] P. Michler, *Quantum Dots for Quantum Information Technologies*. Cham Springer International Publishing, 2017.

[85] Y.-M. He, Y. He, Y.-J. Wei, D. Wu, M. Atatüre, C. Schneider, S. Höfling, M. Kamp, C.-Y. Lu, and J.-W. Pan, "On-demand semiconductor single-photon source with

near-unity indistinguishability," *Nature Nanotechnology*, vol. 8, pp. 213–217, Mar. 2013.

[86] H. J. Kimble, "The quantum internet," *Nature*, vol. 453, pp. 1023–1030, June 2008.

[87] N. Somaschi, V. Giesz, L. De Santis, J. C. Loredo, M. P. Almeida, G. Hornecker, S. L. Portalupi, T. Grange, C. Antón, J. Demory, C. Gómez, I. Sagnes, N. D. Lanzillotti-Kimura, A. Lemaítre, A. Auffeves, A. G. White, L. Lanco, and P. Senellart, "Near-optimal single-photon sources in the solid state," *Nature Photonics*, vol. 10, pp. 340–345, May 2016.

[88] Y.-J. Wei, Y.-M. He, M.-C. Chen, Y.-N. Hu, Y. He, D. Wu, C. Schneider, M. Kamp, S. Höfling, C.-Y. Lu, and J.-W. Pan, "Deterministic and Robust Generation of Single Photons from a Single Quantum Dot with 99.5% Indistinguishability Using Adiabatic Rapid Passage," *Nano Letters*, vol. 14, pp. 6515–6519, Nov. 2014.

[89] H. Li, B. Yao, T. Tu, and G. Guo, "Quantum computation on gate-defined semiconductor quantum dots," *Chinese Science Bulletin*, vol. 57, pp. 1919–1924, June 2012.

[90] J. Darulová, S. Pauka, N. Wiebe, K. Chan, G. Gardener, M. Manfra, M. Cassidy, and M. Troyer, "Autonomous Tuning and Charge-State Detection of Gate-Defined Quantum Dots," *Physical Review Applied*, vol. 13, p. 054005, May 2020.

[91] P.-A. Mortemousque, E. Chanrion, B. Jadot, H. Flentje, A. Ludwig, A. D. Wieck, M. Urdampilleta, C. Bäuerle, and T. Meunier, "Coherent control of individual electron spins in a two-dimensional quantum dot array," *Nature Nanotechnology*, vol. 16, pp. 296–301, Mar. 2021.

[92] R. Radebaugh, "Cryocoolers: The state of the art and recent developments," *Journal of Physics: Condensed Matter*, vol. 21, p. 164219, Apr. 2009.

[93] A. H. Olafsdottir and H. U. Sverdrup, "Assessing the Past and Future Sustainability of Global Helium Resources, Extraction, Supply and Use, Using the In-

tegrated Assessment Model WORLD7," *Biophysical Economics and Sustainability*, vol. 5, p. 6, May 2020. He scarcity.

[94] D. Kramer, "Helium users are at the mercy of suppliers," *Physics Today*, vol. 72, pp. 26–29, Apr. 2019.

[95] R. Radenbaugh, "Refrigeration for superconductors," *Proceedings of the IEEE*, vol. 92, pp. 1719–1734, Oct. 2004.

[96] F. Frasconi, E. Majorana, L. Naticchioni, F. Paoletti, and M. Perciballi, "A vertical accelerometer for cryogenics implementation in third-generation gravitational-wave detectors," *Measurement Science and Technology*, vol. 25, p. 015103, Dec. 2013. higher cooling power, interferometry/vibrations.

[97] A. Louchet-Chauvet, R. Ahlefeldt, and T. Chanelière, "Piezospectroscopic measurement of high-frequency vibrations in a pulse-tube cryostat," *Review of Scientific Instruments*, vol. 90, p. 034901, Mar. 2019. measurement styles.

[98] S. Vadia, J. Scherzer, H. Thierschmann, C. Schäfermeier, C. D. Savio, T. Taniguchi, K. Watanabe, D. Hunger, K. Karraï, and A. Högele, "Open-cavity in closed-cycle cryostat as a quantum optics platform," *arXiv:2103.05619 [cond-mat, physics:physics, physics:quant-ph]*, Mar. 2021. Comment: 9 pages, 7 figures.

[99] G. Pagano, P. W. Hess, H. B. Kaplan, W. L. Tan, P. Richerme, P. Becker, A. Kyprianidis, J. Zhang, E. Birckelbaw, M. R. Hernandez, Y. Wu, and C. Monroe, "Cryogenic trapped-ion system for large scale quantum simulation," *Quantum Science and Technology*, vol. 4, p. 014004, Oct. 2018. measurement styles.

[100] T. Dubielzig, S. Halama, H. Hahn, G. Zarantonello, M. Niemann, A. Bautista-Salvador, and C. Ospelkaus, "Ultra-low-vibration closed-cycle cryogenic surface-electrode ion trap apparatus," *Review of Scientific Instruments*, vol. 92, p. 043201, Apr. 2021.

[101] R. S. R. Gajjela, A. L. Hendriks, J. O. Douglas, E. M. Sala, P. Steindl, P. Klenovský, P. A. J. Bagot, M. P. Moody, D. Bimberg, and P. M. Koenraad, "Structural and

compositional analysis of (InGa)(AsSb)/GaAs/GaP Stranski–Krastanov quantum dots," *Light: Science & Applications*, vol. 10, p. 125, June 2021.

[102] E. Peter, P. Senellart, D. Martrou, A. Lemaitre, J. Bloch, J. Hours, and J.-M. Gerard, "Exciton photon strong-coupling regime for a single quantum dot in a microcavity," *Physical Review Letters*, vol. 95, p. 067401, Aug. 2005. Comment: submitted on November 7th 2004.

[103] A. Küster, C. Heyn, A. Ungeheuer, G. Juska, S. Tommaso Moroni, E. Pelucchi, and W. Hansen, "Droplet etching of deep nanoholes for filling with self-aligned complex quantum structures," *Nanoscale Research Letters*, vol. 11, p. 282, June 2016.

[104] W. Rudno-Rudziński, M. Burakowski, J. P. Reithmaier, A. Musiał, and M. Benyoucef, "Magneto-Optical Characterization of Trions in Symmetric InP-Based Quantum Dots for Quantum Communication Applications," *Materials*, vol. 14, p. 942, Jan. 2021.

[105] K. E. Sautter, K. D. Vallejo, and P. J. Simmonds, "Strain-driven quantum dot self-assembly by molecular beam epitaxy," *Journal of Applied Physics*, vol. 128, p. 031101, July 2020. QD Growth.

[106] "Millennia® eV™ CW DPSS Laser." https://www.spectra-physics.com/en/f/millennia-ev-cw-dpss-laser.

[107] D. R. Paschotta, "Heisenberg's Uncertainty Principle and the Transform Limit." https://www.rp-photonics.com/spotlight_2008_06_13.html.

[108] K. G. Lagoudakis, K. A. Fischer, T. Sarmiento, P. L. McMahon, M. Radulaski, J. L. Zhang, Y. Kelaita, C. Dory, K. Müller, and J. Vučković, "Observation of Mollow Triplets with Tunable Interactions in Double Lambda Systems of Individual Hole Spins," p. 6. AB.

[109] K. G. Lagoudakis, P. L. Mcmahon, C. Dory, K. A. Fischer, K. Müller, V. Borish, D. Dalacu, P. J. Poole, M. E. Reimer, V. Zwiller, Y. Yamamoto, and J. Vuckovic,

"Ultrafast coherent manipulation of trions in site-controlled nanowire quantum dots," p. 6. AB.

[110] "The Optics Of Spectroscopy,"

[111] "Field guide to polarization | WorldCat.org." https://search.worldcat.org/title/58456547.

[112] S. G. Reddy, S. Prabhakar, A. Aadhi, A. Kumar, M. Shah, R. P. Singh, and R. Simon, "Measuring the Mueller matrix of an arbitrary optical element with a universal SU(2) polarization gadget," *JOSA A*, vol. 31, pp. 610–615, Mar. 2014.

[113] *Polarized Light, Revised and Expanded*. CRC Press, June 2003.

[114] *Polarized Light*.

[115] K. Barr, B. Hourahine, C. Schneider, S. Höfling, and K. G. Lagoudakis, "Towards spin state tailoring of charged excitons in InGaAs quantum dots using oblique magnetic fields," *Physical Review B*, vol. 109, p. 075433, Feb. 2024.

[116] T. A. Wilkinson, C. E. Maurer, C. J. Flood, G. Lander, S. Chafin, and E. B. Flagg, "Complete Stokes vector analysis with a compact, portable rotating waveplate polarimeter," *Review of Scientific Instruments*, vol. 92, p. 093101, Sept. 2021.

[117] H. G. Berry, G. Gabrielse, and A. E. Livingston, "Measurement of the Stokes parameters of light," *Applied Optics*, vol. 16, p. 3200, Dec. 1977.

[118] K. De Greve, D. Press, T. D. Ladd, B. Friess, P. l. McMahon, C. Schneider, M. Kamp, S. Hoefling, A. Forchel, and Y. Yamamoto, "Experimental approach to ultrafast optical spin echo of a single quantum dot electron spin," in *OPTO* (Z. U. Hasan, A. E. Craig, P. R. Hemmer, and C. M. Santori, eds.), (San Francisco, California), p. 76110K, Feb. 2010.

[119] K. G. Lagoudakis, K. A. Fischer, T. Sarmiento, K. Mueller, and J. Vučković, "Hole-spin pumping and repumping in a p -type δ-doped InAs quantum dot," *Physical Review B*, vol. 90, p. 121402, Sept. 2014.

[120] K. G. Lagoudakis, P. L. McMahon, K. A. Fischer, S. Puri, K. Müller, Dan Dalacu, P. J. Poole, M. E. Reimer, V. Zwiller, Y. Yamamoto, and J. Vučković, "Initialization of a spin qubit in a site-controlled nanowire quantum dot," *New Journal of Physics*, vol. 18, p. 053024, May 2016.

[121] B. Schaefer, E. Collett, R. Smyth, D. Barrett, and B. Fraher, "Measuring the Stokes polarization parameters," *American Journal of Physics*, vol. 75, pp. 163–168, Feb. 2007.

[122] K. D. Greve, *Towards Solid-State Quantum Repeaters: Ultrafast, Coherent Optical Control and Spin-Photon Entanglement in Charged InAs Quantum Dots*. Springer Science & Business Media, Apr. 2013.

[123] K. McDonnell, L. F. Keary, and J. D. Pritchard, "Demonstration of a Quantum Gate Using Electromagnetically Induced Transparency," *Physical Review Letters*, vol. 129, p. 200501, Nov. 2022.

[124] C. Dory, K. A. Fischer, K. Müller, K. G. Lagoudakis, T. Sarmiento, A. Rundquist, J. L. Zhang, Y. Kelaita, and J. Vučković, "Complete Coherent Control of a Quantum Dot Strongly Coupled to a Nanocavity," *Scientific Reports*, vol. 6, p. 25172, Apr. 2016. CC.

[125] S. M. Clark, K.-M. C. Fu, T. D. Ladd, and Y. Yamamoto, "Quantum Computers Based on Electron Spins Controlled by Ultrafast Off-Resonant Single Optical Pulses," *Physical Review Letters*, vol. 99, p. 040501, July 2007. Off-resonant CC on QD.

[126] B. D. Gerardot, D. Brunner, P. A. Dalgarno, P. Öhberg, S. Seidl, M. Kroner, K. Karrai, N. G. Stoltz, P. M. Petroff, and R. J. Warburton, "Optical pumping of a single hole spin in a quantum dot," *Nature*, vol. 451, pp. 441–444, Jan. 2008.

[127] R. I. Dzhioev, V. L. Korenev, I. A. Merkulov, B. P. Zakharchenya, D. Gammon, Al. L. Efros, and D. S. Katzer, "Manipulation of the Spin Memory of Electrons in n -GaAs," *Physical Review Letters*, vol. 88, p. 256801, June 2002.

[128] O. Krebs, B. Eble, A. Lemaître, P. Voisin, B. Urbaszek, T. Amand, and X. Marie, "Hyperfine interaction in InAs/GaAs self-assembled quantum dots: Dynamical nuclear polarization versus spin relaxation," *Comptes Rendus Physique*, vol. 9, pp. 874–884, Oct. 2008.

[129] M. Kroutvar, Y. Ducommun, D. Heiss, M. Bichler, D. Schuh, G. Abstreiter, and J. J. Finley, "Optically programmable electron spin memory using semiconductor quantum dots," *Nature*, vol. 432, pp. 81–84, Nov. 2004.

[130] I. A. Merkulov, Al. L. Efros, and M. Rosen, "Electron spin relaxation by nuclei in semiconductor quantum dots," *Physical Review B*, vol. 65, p. 205309, Apr. 2002.

[131] X. Xu, Y. Wu, B. Sun, Q. Huang, J. Cheng, D. G. Steel, A. S. Bracker, D. Gammon, C. Emary, and L. J. Sham, "Fast Spin State Initialization in a Singly Charged InAs-GaAs Quantum Dot by Optical Cooling," *Physical Review Letters*, vol. 99, p. 097401, Aug. 2007.

[132] J.-Y. Yan, C. Chen, X.-D. Zhang, Y.-T. Wang, H.-G. Babin, A. D. Wieck, A. Ludwig, Y. Meng, X. Hu, H. Duan, W. Chen, W. Fang, M. Cygorek, X. Lin, D.-W. Wang, C.-Y. Jin, and F. Liu, "Coherent control of a high-orbital hole in a semiconductor quantum dot with near-unity fidelity," Mar. 2023. Comment: Manuscript with 11 pages and 5 figures plus supplementary Information comprising 16 pages and 15 figures.

[133] A. West, B. Hensen, A. Jouan, T. Tanttu, C.-H. Yang, A. Rossi, M. F. Gonzalez-Zalba, F. Hudson, A. Morello, D. J. Reilly, and A. S. Dzurak, "Gate-based single-shot readout of spins in silicon," *Nature Nanotechnology*, vol. 14, pp. 437–441, May 2019.

[134] M. Holtkemper, D. E. Reiter, and T. Kuhn, "Influence of the quantum dot geometry on p -shell transitions in differently charged quantum dots," *Physical Review B*, vol. 97, p. 075308, Feb. 2018.

[135] K. De Greve, P. L. McMahon, D. Press, T. D. Ladd, D. Bisping, C. Schneider, M. Kamp, L. Worschech, S. Höfling, A. Forchel, and Y. Yamamoto, "Ultrafast

coherent control and suppressed nuclear feedback of a single quantum dot hole qubit," *Nature Physics*, vol. 7, pp. 872–878, Nov. 2011.

[136] E. D. Kim, K. Truex, X. Xu, B. Sun, D. G. Steel, A. S. Bracker, D. Gammon, and L. J. Sham, "Fast Spin Rotations by Optically Controlled Geometric Phases in a Charge-Tunable InAs Quantum Dot," *Physical Review Letters*, vol. 104, p. 167401, Apr. 2010.

[137] S. Germanis, P. Atkinson, R. Hostein, C. Gourdon, V. Voliotis, A. Lemaître, M. Bernard, F. Margaillan, S. Majrab, and B. Eble, "Dark-bright exciton coupling in asymmetric quantum dots," *Physical Review B*, vol. 98, p. 155303, Oct. 2018.

[138] M. Jeannin, A. Artioli, P. Rueda-Fonseca, E. Bellet-Amalric, K. Kheng, R. André, S. Tatarenko, J. Cibert, D. Ferrand, and G. Nogues, "Light-hole exciton in a nanowire quantum dot," *Physical Review B*, vol. 95, p. 035305, Jan. 2017.

[139] R. Kaji, S. Ohno, T. Hozumi, and S. Adachi, "Effects of valence band mixing on hole spin coherence via hole-nuclei hyperfine interaction in InAlAs quantum dots," *Journal of Applied Physics*, vol. 113, p. 203511, May 2013.

[140] G. Sallen, B. Urbaszek, M. M. Glazov, E. L. Ivchenko, T. Kuroda, T. Mano, S. Kunz, M. Abbarchi, K. Sakoda, D. Lagarde, A. Balocchi, X. Marie, and T. Amand, "Dark-Bright Mixing of Interband Transitions in Symmetric Semiconductor Quantum Dots," *Physical Review Letters*, vol. 107, p. 166604, Oct. 2011.

[141] M. Bayer, G. Ortner, O. Stern, A. Kuther, A. A. Gorbunov, A. Forchel, P. Hawrylak, S. Fafard, K. Hinzer, T. L. Reinecke, S. N. Walck, J. P. Reithmaier, F. Klopf, and F. Schäfer, "Fine structure of neutral and charged excitons in self-assembled In(Ga)As/(Al)GaAs quantum dots," *Physical Review B*, vol. 65, p. 195315, May 2002.

[142] A. V. Koudinov, I. A. Akimov, Yu. G. Kusrayev, and F. Henneberger, "Optical and magnetic anisotropies of the hole states in Stranski-Krastanov quantum dots," *Physical Review B*, vol. 70, p. 241305, Dec. 2004.

[143] D. N. Krizhanovskii, A. Ebbens, A. I. Tartakovskii, F. Pulizzi, T. Wright, M. S. Skolnick, and M. Hopkinson, "Individual neutral and charged In x Ga 1 - x As - Ga As quantum dots with strong in-plane optical anisotropy," *Physical Review B*, vol. 72, p. 161312, Oct. 2005.

[144] T. Kobayashi, J. Salfi, C. Chua, J. van der Heijden, M. G. House, D. Culcer, W. D. Hutchison, B. C. Johnson, J. C. McCallum, H. Riemann, N. V. Abrosimov, P. Becker, H.-J. Pohl, M. Y. Simmons, and S. Rogge, "Engineering long spin coherence times of spin–orbit qubits in silicon," *Nature Materials*, vol. 20, pp. 38–42, Jan. 2021.

[145] M. O. Scully, M. S. Zubairy, and I. A. Walmsley, "Quantum Optics," *American Journal of Physics*, vol. 67, p. 648, July 1999.

[146] D. L. Press, *Quantum Dot Spins and Microcavities for Quantum Information Processing*. Stanford University, 2010.

[147] T. D. Ladd, D. Press, K. De Greve, P. L. McMahon, B. Friess, C. Schneider, M. Kamp, S. Hoefling, A. Forchel, and Y. Yamamoto, "Nuclear Feedback in a Single Electron-Charged Quantum Dot under Pulsed Optical Control," p. 79480U, Feb. 2011. Comment: 15 pages, 7 figures. Corrected and expanded discussion. Now includes analysis of spin-echo and optical pumping experiments, in addition to FID.

[148] H. Bluhm, S. Foletti, I. Neder, M. Rudner, D. Mahalu, V. Umansky, and A. Yacoby, "Dephasing time of GaAs electron-spin qubits coupled to a nuclear bath exceeding 200 μs," *Nature Physics*, vol. 7, pp. 109–113, Feb. 2011.

[149] J. G. Tischler, A. S. Bracker, D. Gammon, and D. Park, "Fine structure of trions and excitons in single GaAs quantum dots," *Physical Review B*, vol. 66, p. 081310, Aug. 2002.

[150] I. Toft and R. T. Phillips, "Hole g factors in GaAs quantum dots from the angular dependence of the spin fine structure," *Physical Review B*, vol. 76, p. 033301, July 2007.

[151] B. J. Witek, R. W. Heeres, U. Perinetti, E. P. A. M. Bakkers, L. P. Kouwenhoven, and V. Zwiller, "Measurement of the g -factor tensor in a quantum dot and disentanglement of exciton spins," *Physical Review B*, vol. 84, p. 195305, Nov. 2011.

[152] B. Van Hattem, P. Corfdir, P. Brereton, P. Pearce, A. M. Graham, M. J. Stanley, M. Hugues, M. Hopkinson, and R. T. Phillips, "From the artificial atom to the Kondo-Anderson model: Orientation-dependent magnetophotoluminescence of charged excitons in InAs quantum dots," *Physical Review B*, vol. 87, p. 205308, May 2013. Diamagnetic shifts nice matching

B field angle dependence.

[153] I. A. Yugova, A. Greilich, E. A. Zhukov, D. R. Yakovlev, M. Bayer, D. Reuter, and A. D. Wieck, "Exciton fine structure in In Ga As / Ga As quantum dots revisited by pump-probe Faraday rotation," *Physical Review B*, vol. 75, p. 195325, May 2007.

[154] A. Schwan, B.-M. Meiners, A. Greilich, D. R. Yakovlev, M. Bayer, A. D. B. Maia, A. A. Quivy, and A. B. Henriques, "Anisotropy of electron and hole g-factors in (In,Ga)As quantum dots," *Applied Physics Letters*, vol. 99, p. 221914, Dec. 2011.

[155] V. V. Belykh, D. R. Yakovlev, J. J. Schindler, E. A. Zhukov, M. A. Semina, M. Yacob, J. P. Reithmaier, M. Benyoucef, and M. Bayer, "Large anisotropy of electron and hole g factors in infrared-emitting InAs/InAlGaAs self-assembled quantum dots," *Physical Review B*, vol. 93, p. 125302, Mar. 2016.

[156] V. V. Belykh, A. Greilich, D. R. Yakovlev, M. Yacob, J. P. Reithmaier, M. Benyoucef, and M. Bayer, "Electron and hole g factors in InAs/InAlGaAs self-assembled quantum dots emitting at telecom wavelengths," *Physical Review B*, vol. 92, p. 165307, Oct. 2015.

[157] S. Varwig, A. Schwan, D. Barmscheid, C. Müller, A. Greilich, I. A. Yugova, D. R. Yakovlev, D. Reuter, A. D. Wieck, and M. Bayer, "Hole spin precession in a (In,Ga)As quantum dot ensemble: From resonant spin amplification to spin mode locking," *Physical Review B*, vol. 86, p. 075321, Aug. 2012.

[158] S. A. Crooker, J. Brandt, C. Sandfort, A. Greilich, D. R. Yakovlev, D. Reuter, A. D. Wieck, and M. Bayer, "Spin Noise of Electrons and Holes in Self-Assembled Quantum Dots," *Physical Review Letters*, vol. 104, p. 036601, Jan. 2010.

[159] J.-M. Meyer, I. Hapke-Wurst, U. Zeitler, R. Haug, and K. Pierz, "Resonant Tunnelling through InAs Quantum Dots in Tilted Magnetic Fields: Experimental Determination of the g-Factor Anisotropy," *physica status solidi (b)*, vol. 224, no. 3, pp. 685–688, 2001.

[160] I. Hapke-Wurst, U. Zeitler, R. Haug, and K. Pierz, "Mapping the g factor anisotropy of InAs self-assembled quantum dots," *Physica E: Low-dimensional Systems and Nanostructures*, vol. 12, pp. 802–805, Jan. 2002.

[161] T. P. M. Alegre, F. G. G. Hernández, A. L. C. Pereira, and G. Medeiros-Ribeiro, "Landé g Tensor in Semiconductor Nanostructures," *Physical Review Letters*, vol. 97, p. 236402, Dec. 2006.

[162] T. A. Wilkinson, D. J. Cottrill, J. M. Cramlet, C. E. Maurer, C. J. Flood, A. S. Bracker, M. Yakes, D. Gammon, and E. B. Flagg, "Spin-selective AC Stark shifts in a charged quantum dot," *Applied Physics Letters*, vol. 114, p. 133104, Apr. 2019.

[163] BJ. Witek, *Quantum Dot Spin Engineering for Quantum Optics*. Dissertation (TU Delft), Casimir PhD Series, Delft, 2014.

[164] C. Tonin, R. Hostein, V. Voliotis, R. Grousson, A. Lemaitre, and A. Martinez, "Polarization properties of excitonic qubits in single self-assembled quantum dots," *Physical Review B*, vol. 85, p. 155303, Apr. 2012.

[165] K. Moratis, J. Cibert, D. Ferrand, and Y.-M. Niquet, "Light hole states in a strained quantum dot: Numerical calculation and phenomenological models," *Physical Review B*, vol. 103, p. 245304, June 2021.

[166] T. Belhadj, T. Amand, A. Kunold, C.-M. Simon, T. Kuroda, M. Abbarchi, T. Mano, K. Sakoda, S. Kunz, X. Marie, and B. Urbaszek, "Impact of heavy hole-

light hole coupling on optical selection rules in GaAs quantum dots," *Applied Physics Letters*, vol. 97, p. 051111, Aug. 2010.

[167] S. Maier, P. Gold, A. Forchel, N. Gregersen, J. Mørk, S. Höfling, C. Schneider, and M. Kamp, "Bright single photon source based on self-aligned quantum dot–cavity systems," *Optics Express*, vol. 22, pp. 8136–8142, Apr. 2014.

[168] M. Kroner, K. M. Weiss, B. Biedermann, S. Seidl, A. W. Holleitner, A. Badolato, P. M. Petroff, P. Öhberg, R. J. Warburton, and K. Karrai, "Resonant two-color high-resolution spectroscopy of a negatively charged exciton in a self-assembled quantum dot," *Physical Review B*, vol. 78, p. 075429, Aug. 2008.

[169] E. A. Chekhovich, M. N. Makhonin, A. I. Tartakovskii, A. Yacoby, H. Bluhm, K. C. Nowack, and L. M. K. Vandersypen, "Nuclear spin effects in semiconductor quantum dots," *Nature Materials*, vol. 12, pp. 494–504, June 2013.

[170] T. Yokoi, S. Adachi, S. Muto, H. Sasakura, H. Song, S. Hirose, and T. Usuki, "Observation of Overhauser shift in a self-assembled InAlAs quantum dot," *Physica E: Low-dimensional Systems and Nanostructures*, vol. 29, pp. 510–514, Nov. 2005.

[171] B. Eble, O. Krebs, A. Lemaître, K. Kowalik, A. Kudelski, P. Voisin, B. Urbaszek, X. Marie, and T. Amand, "Dynamic nuclear polarization of a single charge-tunable InAs / GaAs quantum dot," *Physical Review B*, vol. 74, p. 081306, Aug. 2006.

[172] O. Krebs, P. Maletinsky, T. Amand, B. Urbaszek, A. Lemaître, P. Voisin, X. Marie, and A. Imamoglu, "Anomalous Hanle Effect due to Optically Created Transverse Overhauser Field in Single InAs / GaAs Quantum Dots," *Physical Review Letters*, vol. 104, p. 056603, Feb. 2010.

[173] P. Millington-Hotze, H. E. Dyte, S. Manna, S. F. C. da Silva, A. Rastelli, and E. A. Chekhovich, "Approaching a fully-polarized state of nuclear spins in a semiconductor quantum dot," Feb. 2023.

[174] D. S. Smirnov, T. S. Shamirzaev, D. R. Yakovlev, and M. Bayer, "Dynamic Polarization of Electron Spins Interacting with Nuclei in Semiconductor Nanostructures," *Physical Review Letters*, vol. 125, p. 156801, Oct. 2020.

[175] L. Zaporski, N. Shofer, J. H. Bodey, S. Manna, G. Gillard, M. H. Appel, C. Schimpf, S. F. Covre da Silva, J. Jarman, G. Delamare, G. Park, U. Haeusler, E. A. Chekhovich, A. Rastelli, D. A. Gangloff, M. Atatüre, and C. Le Gall, "Ideal refocusing of an optically active spin qubit under strong hyperfine interactions," *Nature Nanotechnology*, vol. 18, pp. 257–263, Mar. 2023.

[176] B. Urbaszek, X. Marie, T. Amand, O. Krebs, P. Voisin, P. Maletinsky, A. Högele, and A. Imamoglu, "Nuclear spin physics in quantum dots: An optical investigation," *Reviews of Modern Physics*, vol. 85, pp. 79–133, Jan. 2013.

[177] D. Kim, S. G. Carter, A. Greilich, A. S. Bracker, and D. Gammon, "Ultrafast optical control of entanglement between two quantum-dot spins," *Nature Physics*, vol. 7, pp. 223–229, Mar. 2011. Two-qubit QD and CC.

[178] J. Altepeter, E. Jeffrey, and P. Kwiat, "Photonic State Tomography," in *Advances In Atomic, Molecular, and Optical Physics*, vol. 52, pp. 105–159, Elsevier, 2005.

[179] D. Cogan, G. Peniakov, Z.-E. Su, and D. Gershoni, "Complete state tomography of a quantum dot spin qubit," *Physical Review B*, vol. 101, p. 035424, Jan. 2020.

[180] J. J. Longdell and M. J. Sellars, "Experimental demonstration of quantum-state tomography and qubit-qubit interactions for rare-earth-metal-ion-based solid-state qubits," *Physical Review A*, vol. 69, p. 032307, Mar. 2004.

[181] J. Zhang, S. S. Hegde, and D. Suter, "Fast Quantum State Tomography in the Nitrogen Vacancy Center of Diamond," *Physical Review Letters*, vol. 130, p. 090801, Feb. 2023.

[182] D. Kim, Z. Shi, C. B. Simmons, D. R. Ward, J. R. Prance, T. S. Koh, J. K. Gamble, D. E. Savage, M. G. Lagally, M. Friesen, S. N. Coppersmith, and M. A. Eriksson,

"Quantum control and process tomography of a semiconductor quantum dot hybrid qubit," *Nature*, vol. 511, pp. 70–74, July 2014.

[183] R. Hafenbrak, S. M. Ulrich, P. Michler, L. Wang, A. Rastelli, and O. G. Schmidt, "Triggered polarization-entangled photon pairs from a single quantum dot up to 30 K," *New Journal of Physics*, vol. 9, pp. 315–315, Sept. 2007.

[184] T. Huber, L. Ostermann, M. Prilmüller, G. S. Solomon, H. Ritsch, G. Weihs, and A. Predojević, "Coherence and degree of time-bin entanglement from quantum dots," *Physical Review B*, vol. 93, p. 201301, May 2016. Biexciton time-bin.

[185] M. Howard, J. Twamley, C. Wittmann, T. Gaebel, F. Jelezko, and J. Wrachtrup, "Quantum process tomography and Linblad estimation of a solid-state qubit," *New Journal of Physics*, vol. 8, p. 33, Mar. 2006.

[186] X. Wang, C.-S. Yu, and X. X. Yi, "An alternative quantum fidelity for mixed states of qudits," *Physics Letters A*, vol. 373, pp. 58–60, Dec. 2008.

[187] M. Atatüre, J. Dreiser, A. Badolato, A. Högele, K. Karrai, and A. Imamoglu, "Quantum-Dot Spin-State Preparation with Near-Unity Fidelity," *Science*, vol. 312, pp. 551–553, Apr. 2006.

[188] L. Garza-Soto, N. Hagen, and D. Lopez-Mago, "Deciphering Pancharatnam's discovery of geometric phase: Retrospective," *JOSA A*, vol. 40, pp. 925–931, May 2023.

[189] D. Xiao, M.-C. Chang, and Q. Niu, "Berry phase effects on electronic properties," *Reviews of Modern Physics*, vol. 82, pp. 1959–2007, July 2010.

[190] D. A. Steck, "Quantum and Atom Optics,"

[191] K. De Greve, P. L. McMahon, L. Yu, J. S. Pelc, C. Jones, C. M. Natarajan, N. Y. Kim, E. Abe, S. Maier, C. Schneider, M. Kamp, S. Höfling, R. H. Hadfield, A. Forchel, M. M. Fejer, and Y. Yamamoto, "Complete tomography of a high-fidelity solid-state entangled spin–photon qubit pair," *Nature Communications*, vol. 4, p. 2228, Oct. 2013.

[192] J. P. Lee, B. Villa, A. J. Bennett, R. M. Stevenson, D. J. P. Ellis, I. Farrer, D. A. Ritchie, and A. J. Shields, "A quantum dot as a source of time-bin entangled multi-photon states," *Quantum Science and Technology*, vol. 4, p. 025011, Mar. 2019. Time-bin entanglement (Voigt).

[193] K. Sharman, F. K. Asadi, S. C. Wein, and C. Simon, "Quantum repeaters based on individual electron spins and nuclear-spin-ensemble memories in quantum dots," *arXiv:2010.13863 [quant-ph]*, Jan. 2021. Comment: 14 pages, 4 figures.

[194] A. Greilich, S. E. Economou, S. Spatzek, D. R. Yakovlev, D. Reuter, A. D. Wieck, T. L. Reinecke, and M. Bayer, "Ultrafast optical rotations of electron spins in quantum dots," *Nature Physics*, vol. 5, pp. 262–266, Apr. 2009.

[195] M. Goryca, J. Li, A. V. Stier, T. Taniguchi, K. Watanabe, E. Courtade, S. Shree, C. Robert, B. Urbaszek, X. Marie, and S. A. Crooker, "Revealing exciton masses and dielectric properties of monolayer semiconductors with high magnetic fields," *Nature Communications*, vol. 10, p. 4172, Sept. 2019.

[196] H. Kosaka, H. Shigyou, Y. Mitsumori, Y. Rikitake, H. Imamura, T. Kutsuwa, K. Arai, and K. Edamatsu, "Coherent Transfer of Light Polarization to Electron Spins in a Semiconductor," *Physical Review Letters*, vol. 100, p. 096602, Mar. 2008.